POLITECNICO
MILANO 1863

SCUOLA DI INGEGNERIA INDUSTRIALE
E DELL'INFORMAZIONE

A semi-analytical model for low thrust collision avoidance manoeuvres in presence of orbital perturbations

TESI DI LAUREA MAGISTRALE IN
SPACE ENGINEERING - INGEGNERIA SPAZIALE

Author: **Dimuthu Malshan Wedaralage**

Student ID: 964061
Advisor: Prof. Juan Luis Gonzalo Gómez
Academic Year: 2021-2022

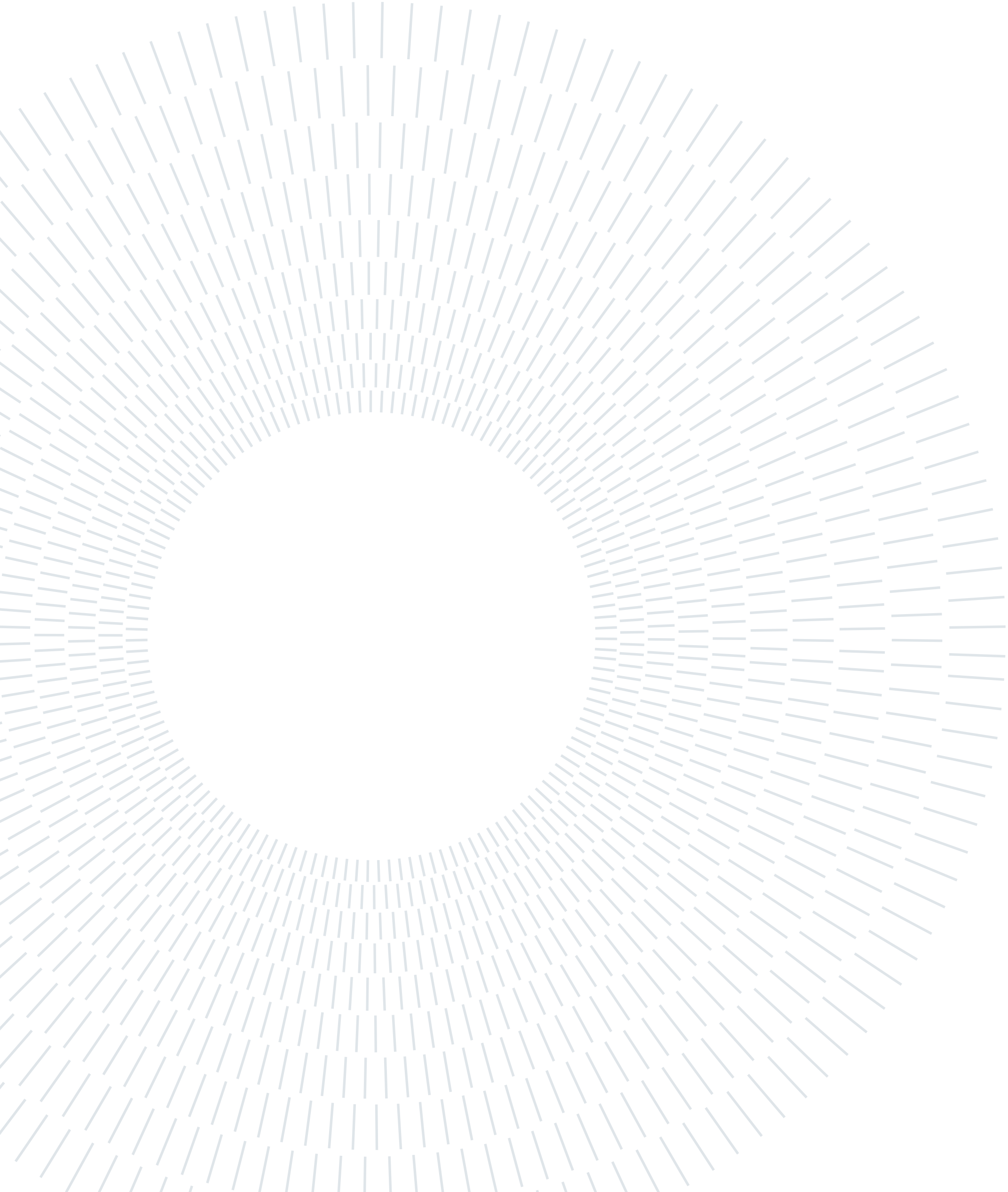

Copyright© April 2023 by Dimuthu Malshan Wedaralage.
All right reserved.

This content is original, written by the Author, Dimuthu Malshan Wedaralage. All the non-originals information, taken from previous works, are specified and recorded in the Bibliography.

When referring to this work, full bibliographic details must be given, i.e. Dimuthu Malshan Wedaralage, “A semi-analytical model for low thrust collision avoidance manoeuvres in presence of orbital perturbations”. 2023, Politecnico di Milano, Faculty of Industrial Engineering, Department of Aerospace Science and Technologies, Master in Space Engineering, Supervisor: Juan Luis Gonzalo Gómez.

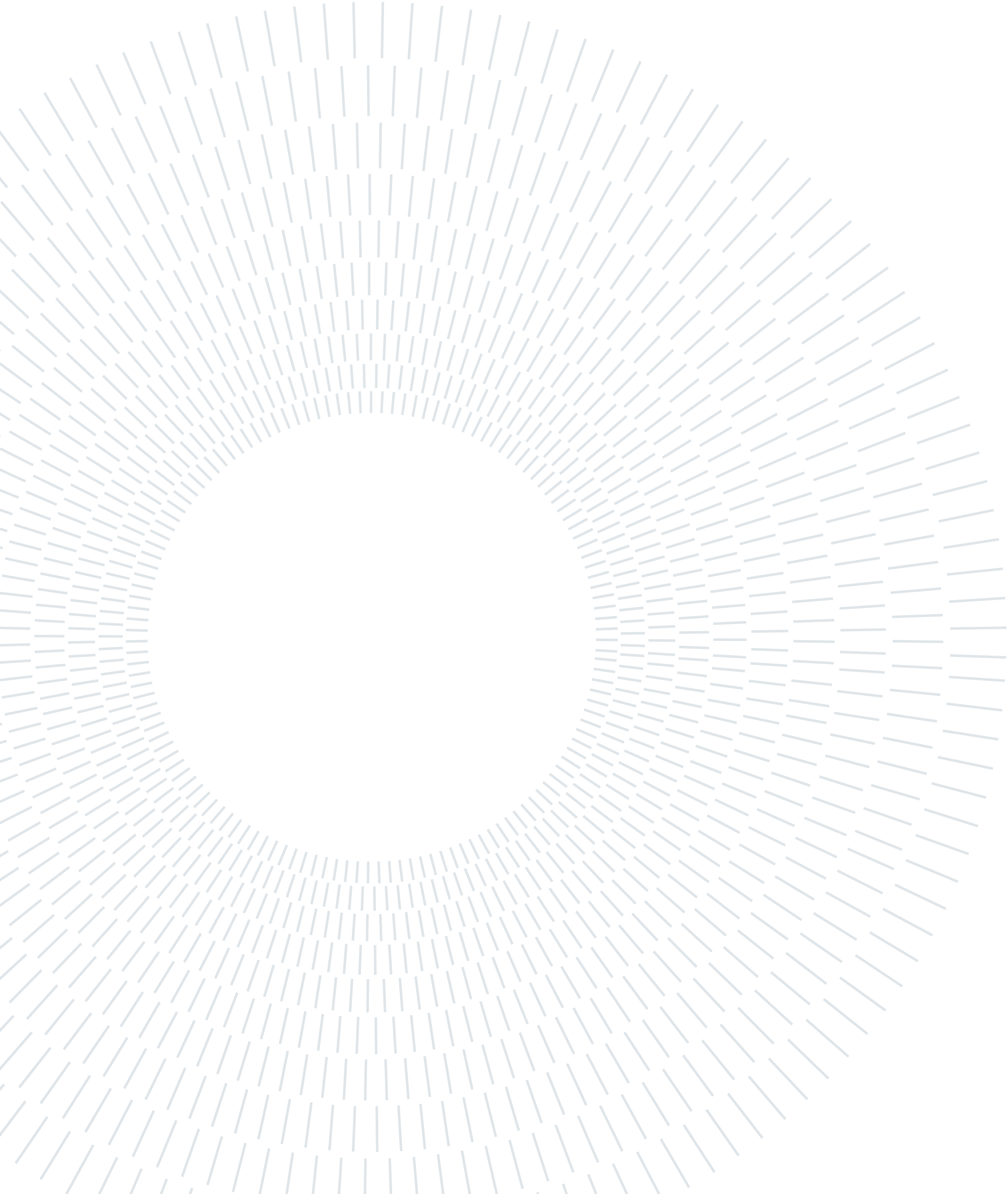

Abstract

In the latest years the population of space debris and satellites has considerably increased leading to the phenomenon of space congestion, in particular near Low Earth Orbits' (LEO) region; to decrease the risk of collisions, different strategies have been implemented based mainly on the design of collision avoidance manoeuvres (CAMs), which are regularly performed by operators.

Together with space congestion, it is important to take into account also the increasing amount of low thrust satellites in space, that are preferred due to their better fuel performances but also add complications in the design process since they require longer active times and the current methods are based on fully numerical models which are very expensive from a computational point of view, whereas the analytical models, that already exist, do not take into account any orbital perturbation (or at least only a few of them).

The following thesis focuses on the implementation and validation of semi-analytical algorithms for the design of low-thrust CAMs subject to different orbital perturbations: lightweight semi-analytical (SA) algorithms are implemented, considering not only a constant low-thrust perturbation but also other kind of orbital perturbations, such as atmospheric drag and J_2 for LEOs, and luni-solar, solar radiation pressure (SRP) and J_2 for Geostationary Earth Orbits (GEO).

Lastly parametric analysis of the SA models are performed in the design process in order to solve optimisation problems and define the optimal conditions to gain the maximum miss distance or the minimum probability of collision (PoC) from the secondary object.

The results are analysed and compared with respect to reference values, obtained through numerical integration to highlight the accuracy and the gain in the computational time; in this way it is possible to deal with the high amount of daily close approaches by retrieving the optimal solution in a matter of few minutes (or seconds) with respect to a fully numerical model which can take also some hours.

Key words: Collision avoidance manoeuvre, Orbital perturbation, Semi-analytical model, Low thrust, Probability of collision, CAM design and optimisation.

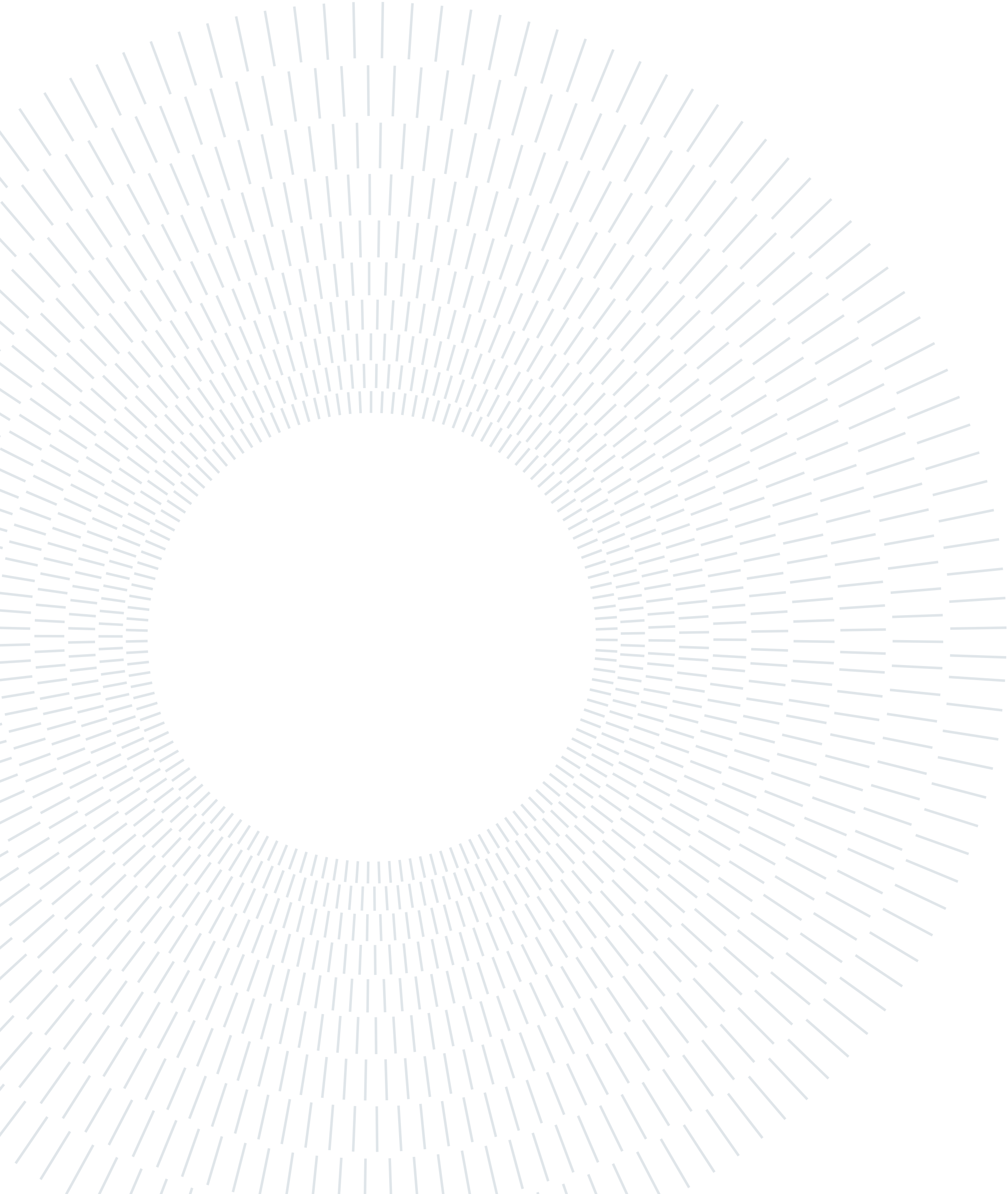

Abstract in lingua italiana

Negli ultimi anni la popolazione di detriti spaziali e satelliti è considerevolmente aumentata portando al fenomeno della congestione spaziale, in particolare attorno alla zona dei satelliti LEO; per diminuire il rischio di collisioni, diverse strategie sono state implementate basate principalmente sul design di manovre di anti-collisione che sono effettuati regolarmente da un operatore.
Oltre alla congestione spaziale, è importante tenere in considerazione anche l'aumento dei satelliti a bassa spinta nello spazio, che sono preferiti per la miglior prestazione del carburante ma che aggiungono anche complicazioni poichè richiedono periodi di attività molto lunghi e i metodi attuali per il loro design si basano su modelli interamente numerici ad alto costo computazionale mentre i modelli analitici già presenti tengono in considerazione poche se non nessuna perturbazione orbitale.
La seguente tesi intende focalizzarsi sull'implementazione e validazione di algoritmi semi-analitici per il design di LT CAMs soggetti a diverse perturbazioni: verranno ideati degli algoritmi semi-analitici a basso costo computazionale che oltre alla bassa spinta, terranno conto anche delle diverse perturbazioni orbitali come resistenza atmosferica e J_2 presenti nei satelliti LEO o perturbazioni luni-solari, J_2 e pressione di radiazione solare (SRP) presenti invece nei satelliti GEO.
Infine verranno effettuate analisi parametriche dei modelli nel processo di design per poter definire le condizioni ottimali per risolvere problemi di ottimizzazione ed ottenere la massima deviazione o la minima probabilità di collisione dal corpo secondario.
I risultati sono dunque analizzati e comparati con valori di riferimento ottenuti tramite integrazione numerica in modo da poter ottenere un confronto sull'accuratezza e il guadagno nei costi computazionali; in questo modo è possibile gestire l'alto numero di eventi di avvicinamento ottenendo la soluzione ottimale in pochi minuti (o secondi) rispetto ad un modello interamente numerico che altrimenti impiegherebbe ore.

Parole chiave: Manovre di anti-collisione, Perturbazioni orbitali, Modelli semi-analitici, Bassa spinta, Probabilità di collisione, Design e ottimizzazione di manovre.

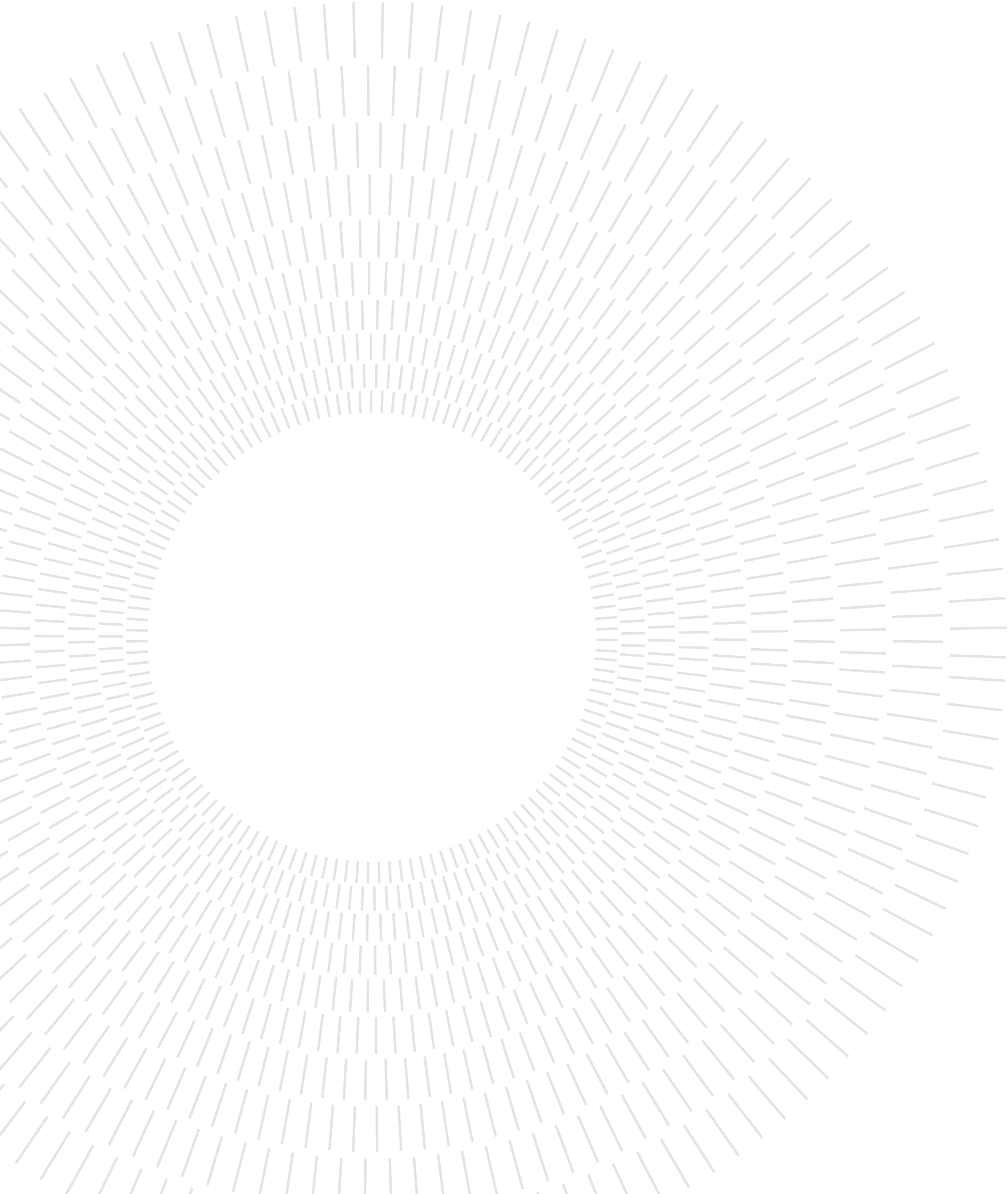

Contents

Abstract **i**

Abstract in lingua italiana **iii**

Contents **v**

1 Introduction **1**
- 1.1 General Introduction and Motivation 1
- 1.2 CAM Operational Background 2
  - 1.2.1 Collision Avoidance Process at ESOC 2
  - 1.2.2 Event Statistics 5
  - 1.2.3 Summary on ESOC's CAM Process 6
- 1.3 CAM's State of the Art 6
  - 1.3.1 Impulsive Collision Avoidance Manoeuvre 7
  - 1.3.2 Low Thrust Collision Avoidance Manoeuvre 11
- 1.4 Thesis Goal 17
  - 1.4.1 Scope of the Work 17
  - 1.4.2 Original Contribution from the Thesis 17
  - 1.4.3 Thesis Outline 17

2 Orbit Perturbations **19**
- 2.1 Introduction 19
- 2.2 Gravitational Perturbation 20
- 2.3 Atmospheric Drag 21
- 2.4 Solar Radiation Pressure 22
- 2.5 Third Body Perturbation 23

3 Collision Probability **25**
- 3.1 Chan's Model 27

3.2 Serra's Model 28
3.3 Patera's Model 29
3.4 Alfano's Model 29
3.5 Foster's Model 30

4 Perturbation Models 33
4.1 Analytical J_2 Models 33
  4.1.1 Aksnes Model on LEO 34
  4.1.2 Lyddane Model on GEO 36
4.2 Semi-Analytical Atmospheric Drag Models 38
  4.2.1 Low Eccentricity Drag Model 38
  4.2.2 High Eccentricity Drag Model 39
4.3 Analytical Solar Radiation Pressure Model 41
4.4 Analytical Sun Perturbation Model 43
4.5 Numerical Moon Perturbation Model 46
4.6 Analytical In-Plane Low-Thrust Models 46
  4.6.1 Tangential LT Model 46
  4.6.2 Normal LT Model 48
4.7 Computation of Perturbed Elements 50

5 CAM Design 53
5.1 Introduction to SA Propagator 53
  5.1.1 Computation of Miss Distance 54
  5.1.2 Computation of PoC 54
5.2 Introduction to Optimisation Problems 55
5.3 Case A : Cost Minimization for Given Miss Distance 55
  5.3.1 Case A : Optimisation on LEO 56
  5.3.2 Case A : Optimisation on GEO 60
5.4 Case B : Time Minimization for Given Miss Distance 65
  5.4.1 Case B : Optimisation on LEO 66
  5.4.2 Case B : Optimisation on GEO 71
5.5 Case C : Cost Minimization for Given PoC 76
  5.5.1 Case C : Optimisation on LEO 76
  5.5.2 Case C : Optimisation on GEO 80
5.6 Case D : PoC Minimisation in a Given Time 85
  5.6.1 Case D : Optimisation on LEO 85
  5.6.2 Case D : Optimisation on GEO 89
5.7 Cost Breakdown Analysis 93

6 Conclusion **97**
6.1 Conclusive Summary 97
6.2 Future Works 98

Bibliography **99**

A Appendix A **103**
A.1 Gonzalo's Normal Thrust Time Law 103

B Appendix B **105**
B.1 Brouwer's Secular Terms 105
B.2 Brouwer's Short-Periodic Terms 106

C Appendix C **109**
C.1 King-Hele Low Eccentricity Drag Model 109
C.2 King-Hele High Eccentricity Drag Model 110

D Appendix D **113**
D.1 Kozai's SRP Model 113

List of Figures **115**

List of Tables **117**

List of Acronyms **119**

List of Symbols **121**

Acknowledgements **125**

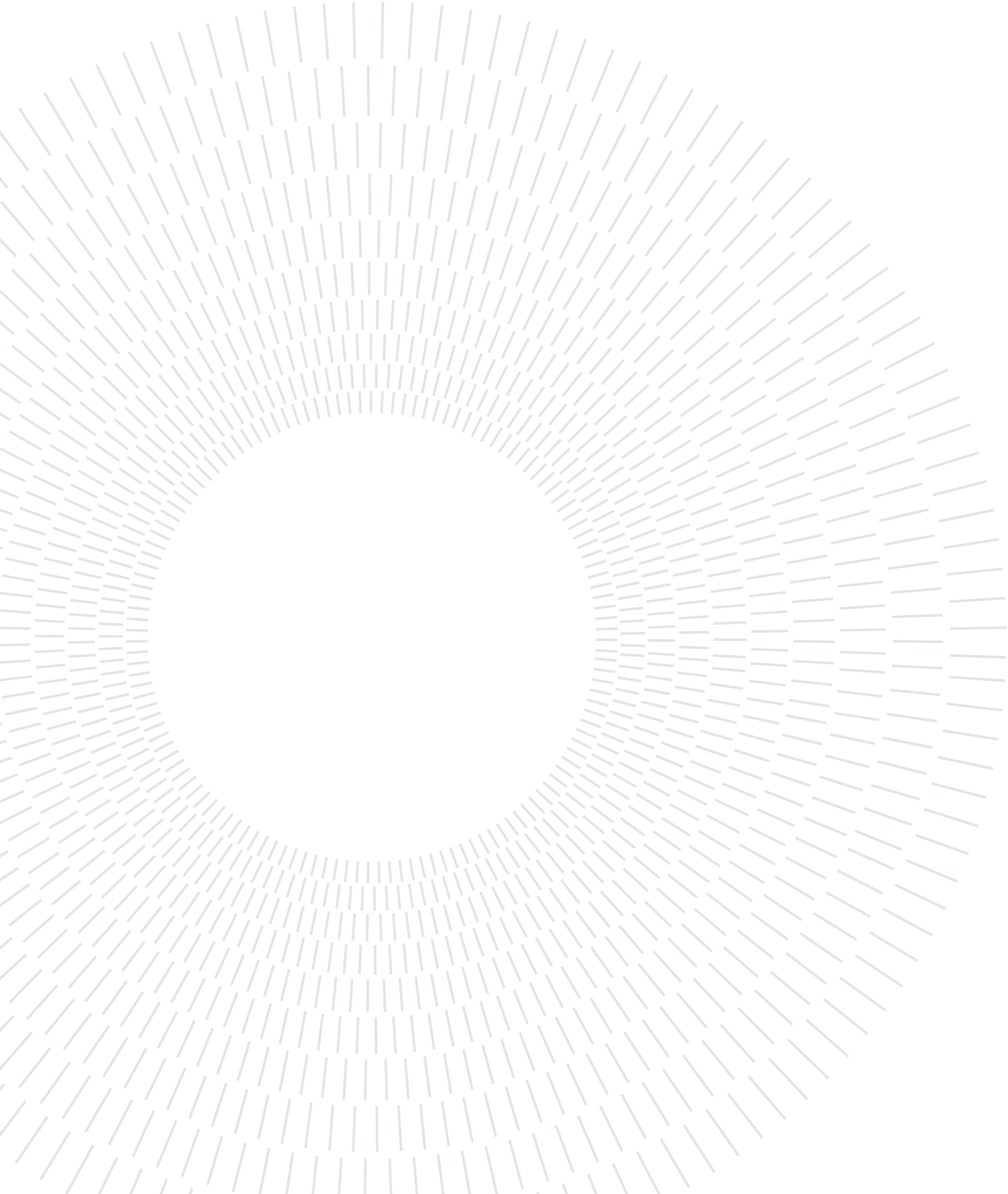

1 | Introduction

1.1. General Introduction and Motivation

In the latest years the population of space debris and satellites has considerably increased leading to the phenomenon of space congestion, in particular near LEO region; to decrease the risk of collisions, different strategies have been implemented:

1. **Design of re-entry manoeuvres for end-of-life satellites** where the Inter-Agency Space Debris Coordination Committee's (IADC) coordinates the activities of the member space agencies regarding space debris mitigation by providing the guidelines for post mission disposal [28]: in the case of GEO spacecrafts (s/c) the strategy is to manoeuvre the spacecraft far away from the GEO protected region in order to avoid interference with other satellites whereas for LEO the strategy consists in de-orbit the s/c (direct reentry is preferred) or manoeuvre it in an auxiliary orbit with an expected orbital lifetime of 25 years.

2. **Active debris removal missions** which are still under research, with technical and regulatory challenges; recent milestones are the successful missions accomplished by Astroscale's ELSA-d and ESA's ClearSpace-1.

3. **Design of collision avoidance manoeuvres (CAMs)** which are regularly performed by operators and are based on low thrust or impulsive propulsion systems;

The thesis focuses on the last point, in particular on perturbed low-thrust CAMs: the phenomenon of space congestion and the increasing amount of low thrust satellites in space, that are preferred due to their better fuel performances, add complications in the design process since they require longer active times and the current methods are based on fully numerical models which are very computationally expensive, whereas the analytical models, that already exist, do not take into account any orbital perturbation (or at least only a few of them); to address this problem, lightweight and accurate mathematical models are defined and implemented for this kind of manoeuvres to find the optimal strategy to get the maximum deviation or the minimum probability of collision (PoC).

1.2. CAM Operational Background

The European Space Agency's Space Debris Office (SDO) at European Space Operation Centre (ESOC) provides a service to support operational collision avoidance activities: the support consists mainly in conjunction events' detection, collision risk assessment, orbit determination and orbit and covariance propagation of objects involved in high risk conjunction events (HRCE).

This chapter gives an introduction to collision avoidance processes involved at ESOC with insights on the related activities in the recent years and on the statistical distribution of conjunction events.

1.2.1. Collision Avoidance Process at ESOC

The service is supported by two main tools:

- **CRASS** (Collision Risk Assessment Software) to predict daily conjunction events and to assess the associated PoC;
- **ODIN** (Orbit Determination by Improved Normal Equations) to improve the orbit determination of secondary object (e.g. debris or inoperative satellite) involved in HRCE through processing of acquired tracking data;

All of the provided services work following two steps:

1. Upcoming HRCE are identified based on Two-Lines-Elements (TLE) data obtained from United States STRATegic COMmand (USSTRATCOM), whereas precise orbit and covariance information of the object is obtained from ESA's Database and Information System Characterising Objects in Space (DISCOS), lastly the results are distributed as CRASS daily bulletins.
   This process is executed daily in an automated manner;
2. The second step is only applied to particular events with an estimated PoC higher than a certain threshold; these events are supported by further tracking data of the secondary object to ease the analysis, then a recommendation is sent to the mission management about whether or not to perform a CAM and how to perform it; any manoeuvre trajectory is screened for the introduction of secondary conjunction events.
   This process is applied in case of HRCE and requires an operator.

The overall process is shown in Figure 1.1, highlighting the first (orange) and second (green) steps.

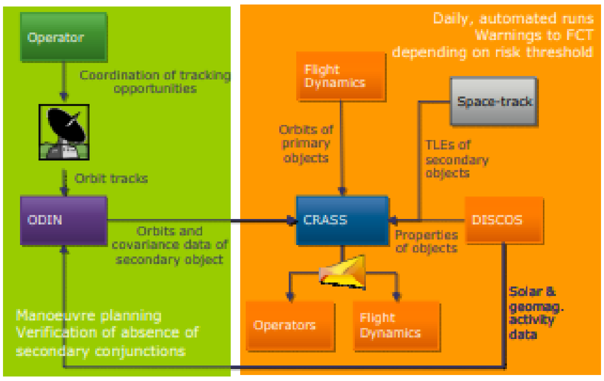
Operator
Coordination of tracking opportunities
Orbit tracks
ODIN
Orbits and covariance data of secondary object
Manoeuvre planning
Verification of absence of secondary conjunctions
Daily, automated runs
Warnings to FCT
depending on risk threshold
Flight Dynamics
Space-track
Orbits of primary objects
TLEs of secondary objects
CRASS
DISCOS
Properties of objects
Operators
Flight Dynamics
Solar & geomag. activity data

Figure 1.1: Operations on collision avoidance process at ESOC (from [15]).

As an alternative to this final step, also conjunction events warnings (with information on miss distance in radial, transversal and out-of-plane direction with associated errors) and Conjunction Summary Messages (CSM) received from Combined Space Operation Centre (CSPOC), with information on orbital state and full 6x6 covariance matrices in position and velocity are used since 2009 to perform a collision risk assessment; also in this case the step is initiated by an operator and the overall process is instead illustrated in Figure 1.2.

Reaction times are important in these situations, in case additional tracking data are required this should be notified fourty-eight hours before the conjunction (this time covers the acquisition of orbit determination, re-assessment of the risk, planning and possible implementation of CAM); all analyses need to be finished twelve hours before the conjunction since the command generation and the upload of the CAM require some amount of time.

The design should take into account the time to get to the closest approach (CA) and the conjunction geometry; along-track manoeuvres increase radial separation and can be executed very late (about half period before the conjunction), however they may be not optimal in terms of fuel consumption.

The reaction threshold considers a minimum miss distance or a maximum PoC; the one which is currently applied correspond to a maximum PoC of 10^{-4} in the case of TLE availability; for what it concerns the collision risk, the COllision Risk COmputation Software (CORCOS) provides a collection of different algorithms for its evaluation, such as:

- Alfriend-Akella, that performs the 2D integration of hard body projection in the encounter plane;
- Patera, that performs the contour integration of the projection;
- Maximum probability assuming spherical scaled covariance;

- MonteCarlo analysis;
- Non-spherical objects via projection of the Minkowsky sum to the B-plane;

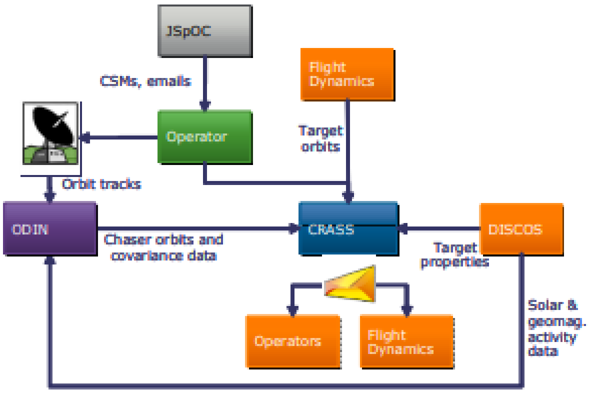
JSpOC
CSMs, emails
Flight Dynamics
Operator
Target orbits
Orbit tracks
ODIN
Chaser orbits and covariance data
CRASS
DISCOS
Target properties
Solar & geomag. activity data
Operators
Flight Dynamics

Figure 1.2: Operations on collision avoidance process at ESOC using CSM (from [15]).

Figure 1.3a shows the TLE-based risk evolution of a conjunction event whether the risk is ignored (red line) or avoided through some actions (green line), in function of the accepted PoC level; this factor can be relaxed to 10^{-3} as shown in Figure 1.3b if CSM are added since they give more reliable and accurate information on the covariance and orbital state; in this way the majority of the risks can be avoided and the frequency of performing expensive CAM can be reduced of one order of magnitude.

It is easy to understand that the high number of close approaches that are detected in a day requires fast and accurate algorithms to complete the design process in a short amount of time and to retrieve the optimal solution especially for low thrust CAMs (LT-CAM) where the control authority is smaller and the required manoeuvring times are longer than impulsive CAMs.

CAM Optimisation Software (CAMOS) supports the planning of avoidance manoeuvres: it allows optimising various objective functions such as minimising risk or Δv or maximising separation; this software can be run in parametric mode to assess one or several strategy analyses computed through a 1D or 2D parametric execution of a manoeuvre optimisation problem, the challenge is to expand the validity regions of CAMOS by obtaining lightweight algorithms especially on LEO that takes into account the different orbital perturbations and that can be used to perform 2D or 3D parametric analysis, and from this, retrieve a solution to the optimisation problems as soon as possible.

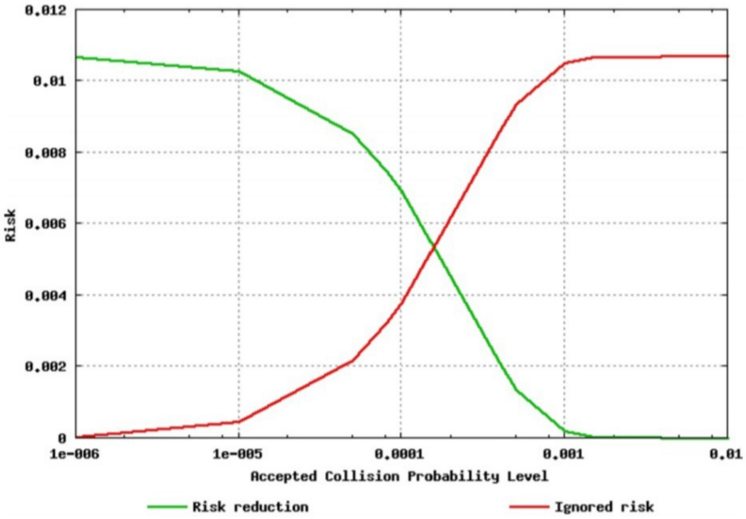

(a)

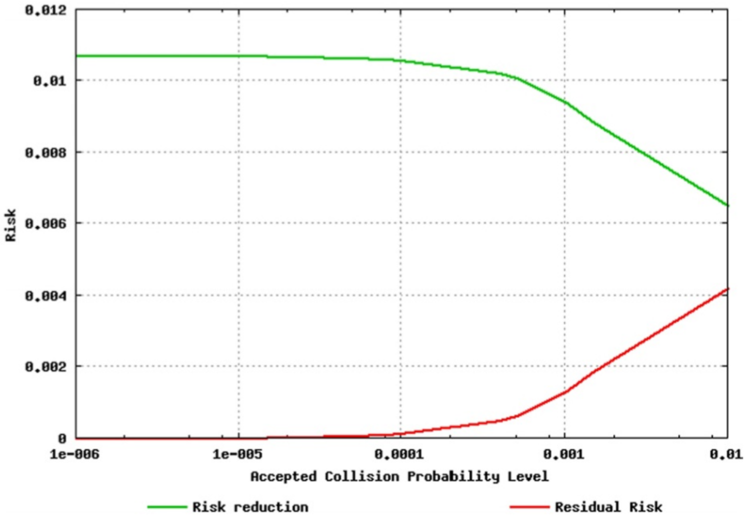

(b)

Figure 1.3: Risk assessment for TLE-based (top) and CSM-based (bottom) data [9].

1.2.2. Event Statistics

The described service is operational since 2006, since then the number of fragmentation particles and debris is increased, and leads to an increasing additional contribution of fragments in the catalogue provided by CSPOC; today from studies done on Envisat (ES), the fragments of Iridium 33, Cosmos 2251 and FengYun 1C in the altitude band of 800 km (band related to Sun-synchronous orbits (SSO)) contribute to roughly two thirds of all its close conjunction events, as shown in Figure 1.4; regarding the number of events in 2010, 43 HRCE, that exceed the PoC threshold, were detected; this is twice the number of events detected in 2009 suggesting that the population of space debris, fragments etc. is increasing.

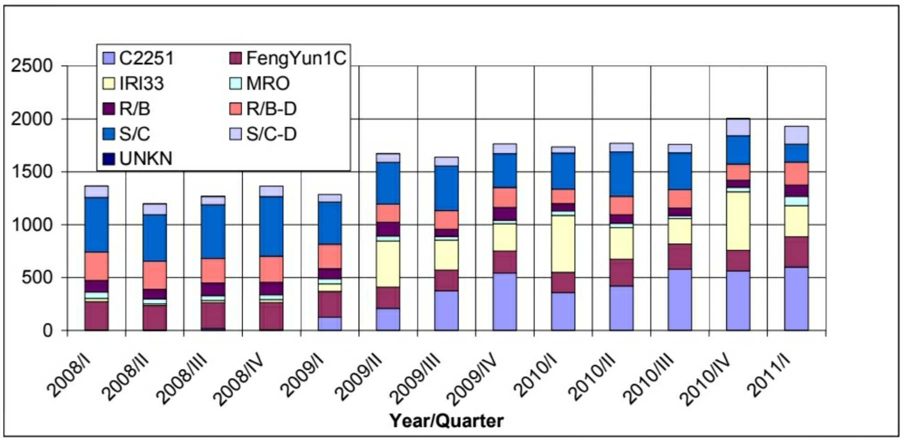

Figure 1.4: Objects encountered by ES into an ellipsoid of 10x25x10 km [15].

1.2.3. Summary on ESOC's CAM Process

Since 2006, ESA's missions in LEOs are monitored by a routine service that identify close conjunction events assessing their PoC with tracking campaigns that are carried out to improve orbit states and covariance of the secondary objects, especially near the operational altitude of SSO.

Until 2010 only TLEs were available for the secondary objects, by then with the use of CSM provided by CSpOC it was possible to have a more accurate definition of HRCE.

1.3. CAM's State of the Art

This section is dedicated to the analysis of the already existing analytical and SA models for the solution of optimisation problems related to impulsive and low thrust CAMs; it is important to highlight that all of these models do not take into account any orbital perturbation.

1. **Impulsive CAM models**: there are several algorithms to solve the different optimisation problems such as miss distance maximisation, PoC minimisation, cost minimisation etc.

   To retrieve the optimal solution, different analytical models have been implemented such as those proposed by Bombardelli and Hernando-Ayuso [5],[8] based on Dromo orbital elements where the solution is retrieved by solving an eigenvalue problem; another model is also proposed by Gonzalo and Colombo [24] where a state transition

matrix (STM) based on Gaussian equations is adopted, this method is less accurate than the Bombardelli's and Hernando-Ayuso's model for long coasting times but it needs less computational time.
Major details about formulas and expressions of Bombardelli and Hernando-Ayuso models are given in section 1.3.1 in order to solve three kind of optimisation problems: miss distance maximisation, PoC minimisation and Δv minimisation.

2. **Low Thrust CAM models**: in this case the optimal solution can be retrieved through a parametric analysis; most of the models are based on semi-analytical (SA) or analytical (AN) averaging techniques that maps the state of the s/c at the detected CA when subject to a in-plane low thrust action.
Regarding tangential low thrust, Colombo et al. developed a SA model based on an approximated time law and a numerical fitting procedure [13], [20].
The model was then improved to an analytical one by Gonzalo et al. first by reducing the fitting procedure to the computation of some elliptic integrals [23] (in this way it was possible to decrease the computational time since no numerical integration of the equations of motion are performed) and later on by adopting a more refined time law model [22] to get a better accuracy.
For what it concern the normal component, a similar averaging procedure to the tangential case was developed by Gonzalo et al. which permits to compute the state of the s/c at CA when subject to the only normal low thrust action [25].
Major details on the SA and AN tangential model and the AN normal model are given in section 1.3.2

1.3.1. Impulsive Collision Avoidance Manoeuvre

In this section analytical solutions for the optimisation of impulsive CAM are treated for the short-term encounters (see definition given in Chapter 3) of an operative s/c, in particular three main optimisation problems are analysed :

- Maximisation of the miss distance δr;
- Minimisation of PoC;
- Minimisation of Δv to get a given PoC;

The first two problems are based on the search of the optimal direction of Δv to grant fuel saving and optimisation of their respective parameters (δr and PoC) through the implementation of analytical and time efficient algorithms.
At the end the optimal solution is found by solving an eigenvalue problem which gives the

optimal direction of Δv; one of the drawbacks of this method is the fact that we cannot optimise the magnitude of the manoeuvre: the magnitude is kept to a constant value Δv_0 which is the total impulse capability of the spacecraft.
The third problem instead minimises the Δv cost both in terms of magnitude and direction in order to grant a given PoC, then results can be plotted in order to show the evolution of the miss distance (or PoC, Δv) in function of different t_{CAM} which is the time instant when the impulsive manoeuvre starts before the CA.

Analytical Model for Miss Distance Optimisation

This problem optimises the thrust direction in order to reach at a given t_{CA} (time of CA) the maximum deflection from the secondary object (an inoperative satellite or a debris) by using the overall thrust capability of the propulsion system; the results, of course differ from each others based on the starting time of the CAM, in particular for very long coasting times Δt_{coast} (time interval between the start of the manoeuvre and the CA) it is demonstrated that the optimal direction aligns with the tangential one if no other perturbations are considered; the algorithms proposed for this problems were implemented by Bombardelli and Hernando-Ayuso [5],[6], and consists in the solution of an eigenvalue problem by using Dromo's orbital elements to grant better accuracy also for very long coasting arcs.
By starting from a given initial miss distance $\vec{\delta r}_e$ the s/c performs at a certain t_{CAM} the manoeuvre with a given $\vec{\Delta v}$ (which components are given in the radial, transversal and out-of-plane (RTH) reference frame); the problem consists in the maximisation of the miss distance $\vec{\delta r}$ projected in the encounter plane (or B-plane).
The encounter plane is in general the plane whose normal direction is aligned with the relative velocity vector of the two objects at the CA and it contains the vector of minimum separation, the directions of the frame used to define the vector $\vec{\delta r} = [\xi \ \eta \ \zeta]^\top$ in this plane are computed as in Eq. (1.1):

$$\begin{cases} \vec{u_\xi} = \frac{\vec{v}_2 \times \vec{v}_1}{||\vec{v}_2 \times \vec{v}_1||} \\ \vec{u_\eta} = \frac{\vec{v}_1 - \vec{v}_2}{||\vec{v}_1 - \vec{v}_2||} \\ \vec{u_\zeta} = \vec{u_\xi} \times \vec{u_\eta} \end{cases} \tag{1.1}$$

the cost function J_r to maximise $\vec{\delta r}$ is instead defined as:

$$J_r = \vec{\delta r}^\top \boldsymbol{Q} \vec{\delta r} = \left(\vec{\delta r}_e + \boldsymbol{M} \vec{\Delta v}\right)^\top \boldsymbol{Q} \left(\vec{\delta r}_e + \boldsymbol{M} \vec{\Delta v}\right) \tag{1.2}$$

which can be reduced to the following form by eliminating the constant terms:

$$\tilde{J}_r(\vec{u}) = \vec{u}^\top \boldsymbol{A}\vec{u} + 2\vec{b}^\top \vec{u} \tag{1.3}$$

subject to the following constraint:

$$f(\vec{u}) = \vec{u}^\top \vec{u} - 1 \leq 0 \tag{1.4}$$

where:

$$\vec{u} = \frac{\vec{\Delta v}}{\Delta v_0} \tag{1.5}$$

$$\vec{b}^\top = \frac{\vec{\delta r_e}^\top \boldsymbol{QM}}{\Delta v_0} \tag{1.6}$$

$$\boldsymbol{M} = \boldsymbol{RKD} \tag{1.7}$$

$$\boldsymbol{A} = \boldsymbol{M}^\top \boldsymbol{QM} \tag{1.8}$$

$$\boldsymbol{Q} = \begin{bmatrix} 1 & 0 & 0 \\ 0 & 0 & 0 \\ 0 & 0 & 1 \end{bmatrix} \tag{1.9}$$

The expression for the matrices **R** (rotation) **K** (kinematics) and **D** (dynamics),based on Dromo elements, can be found in [8].

The problem can be reduced in a convex form and leads to the following non-linear equation :

$$\begin{cases} \left(\frac{\vec{s}_1^\top \vec{b}}{\lambda - \lambda_1}\right)^2 + \left(\frac{\vec{s}_2^\top \vec{b}}{\lambda - \lambda_2}\right)^2 - 1 = 0 \\ \lambda \geq \lambda_1 \end{cases} \tag{1.10}$$

where λ_1, λ_2, $\vec{s}_1$ and $\vec{s}_2$ are respectively the corresponding non-zero eigenvalues of $\boldsymbol{A}$ and their associated eigenvectors, the solution of the equation gives the value λ_{opt} which can be used to compute Δv.

$$\Delta \vec{v}_{opt} = -\Delta v_0 (\boldsymbol{A} - \lambda_{opt} \boldsymbol{I})^P \vec{b} \tag{1.11}$$

where the script P denotes the pseudo-inverse; at this point it is possible to retrieve the maximum miss distance $\vec{\delta r}_{max}$ by substituting Eq. (1.11) in Eq. (1.2).

The overall method consists in the solution of an eigenvalue problem and a non-linear equation, the problem can be simplified in the case of null $\vec{\delta r_e}$ (case of direct impact) where the problem consists only in the solution of an eigenvalue problem where the eigenvector associated to the maximum eigenvalue of $\boldsymbol{A}$ provides the optimal direction.

Analytical Model for Collision Probability Optimisation

This method is still based on the model adopted by Bombardelli and Hernando-Ayuso and consists in performing an impulsive CAM to minimise the PoC.

The model adopted for the probability computation is the one proposed by Chan [11] but other methods exist and can be found in Chapter 3.

The optimisation problem is similar to the one adopted for the maximum deflection CAM with the only difference that the matrix $\mathbf{Q}$ is substituted with $\hat{\boldsymbol{Q}}$ and has the following expression:

$$\hat{\boldsymbol{Q}} = \begin{bmatrix} \frac{1}{\sigma_\xi^2} & 0 & -\frac{\rho_{\xi\zeta}}{\sigma_\xi\sigma_\zeta} \\ 0 & 0 & 0 \\ -\frac{\rho_{\xi\zeta}}{\sigma_\xi\sigma_\zeta} & 0 & \frac{1}{\sigma_\zeta^2} \end{bmatrix} \tag{1.12}$$

where σ_ξ, σ_ζ and $\rho_{\xi\zeta}$ are related to the relative position covariance matrix in B-plane associated to the ξ-ζ axes; once the components (ξ and ζ) of the maximum deflection are obtained, it is possible to retrieve the depth of intrusion v using Eq. (3.8) to compute Chan's PoC as shown in Eq. (3.6).

As before the problem consists in solving an eigenvalue problem and a non-linear equation which leads to the optimal Δv to gain the minimum PoC; the problem, also in this case, can be simplified to the only eigenvalue problem in case of an initial null miss distance $\vec{\delta r}_e$.

Analytical Model for Thrust Optimization

In this problem the thrust magnitude and direction is optimised in order to grant a given PoC; the definition of the problem is similar to those mentioned before and it still consists in the solution of an implicit equation; the associated cost function is defined as:

$$J(\vec{\Delta v}) = \vec{\Delta v}^\top \vec{\Delta v} \tag{1.13}$$

which is subject to the following constraint:

$$(\vec{\delta r}_e + \boldsymbol{M}\vec{\Delta v})^\top \hat{\boldsymbol{Q}} (\vec{\delta r}_e + \boldsymbol{M}\vec{\Delta v}) - v_{req} = 0 \tag{1.14}$$

where v_{req} is computed from P_{req} which is the required PoC that is given as input; by following the same procedure adopted for the optimal miss distance, the problem ends up with an implicit equation which is solved by λ_{opt}, then the optimal thrust is computed as:

$$\vec{\Delta v} = -\lambda_{opt}(\boldsymbol{I} + \lambda_{opt}\hat{\boldsymbol{A}})^P \vec{b} \tag{1.15}$$

also in this case the problem can be reduced to an eigenvalue problem if a direct impact case is considered ($\delta\vec{r}_e$=0).

All of these optimisation problems are also included in the Optimal Computation of CAM (OCCAM) [27], a novel software tool aimed at computing minimum-fuel impulsive CAMs in the short-term encounter scenario using the algorithms that have already been proposed.

1.3.2. Low Thrust Collision Avoidance Manoeuvre

Impulsive CAMs are very efficient when performed a few orbits before the conjunction, on the other hand low-thrust CAMs require longer active times and are very expensive from the computational point when making optimisation and decision-making analysis; to ease this action some semi-analytical and fully analytical models are proposed, based on averaging techniques to shorten the CPU time.

The goal of the LT CAMs is to modify the phasing at the CA in order to reduce the PoC and increase miss distance.

In the following paragraph the two methods based on SA and AN models are illustrated for both the tangential and normal cases and both methods rely on the hypothesis of constant thrust acceleration.

As described for Manoeuvre Intelligence for Space Safety (MISS) [21], the CAM modeling is based mainly on three main blocks:

- Characterisation of orbit modification due to the CAM expressed by means of Keplerian elements;
- Determination of the deviation at CA using linearised relative motion equations to map the changes of Keplerian elements at CA into changes of position and velocity;
- Post-process operations for optimisation analysis;

Regarding the first point, the variation of Keplerian elements (KE) are modelled through the Gauss' planetary equations; in these methods the equations are rewritten after performing a change of variable from time to eccentric anomaly E; the general expression of the first order time law in E when considering a null out-of-plane acceleration is reported below:

$$\frac{dt}{dE} = \frac{r}{an} + a_t \frac{2r^2 \sin\theta}{aben^2 v} + a_n \frac{r^3 (e + \cos\theta)}{a^2 ben^2 v} + o(a_t^2) + o(a_n^2) \tag{1.16}$$

According to the different models this expression can be approximated by neglecting the terms depending on the acceleration to get a zeroth order time law.

At this point the equations are averaged over one period by integrating in E from 0 to 2π

to obtain SA and AN expressions for the KE evolution as function of E: each element x is obtained as a sum of a reference value, a mean value (as result of the averaging method) and an oscillatory components whose expressions differs according to the adopted models:

$$x(E) = x_{ref} + \epsilon_{t,n} x_{mean} + \epsilon_{t,n} x_{osc} \tag{1.17}$$

where $\epsilon_{t,n}$=$a_{t,n} a_{ref}^2/\mu$ is the thrust parameter where the subscript t and n differentiate the tangential and normal cases.

Tangential Semi-Analytical Model

The models adopted in this paragraph are based on the works of Colombo et al. [13],[20] and consider only the tangential component; in this way the only perturbed components are the semi-major axis (a), the eccentricity (e) and the pericenter anomaly (ω): first the following zeroth order time law equation is adopted to perform the change of variable in E:

$$\frac{dt}{dE} \approx \sqrt{\frac{a^3}{\mu}} (1 - e \cos E) \tag{1.18}$$

then the equations in a, e and ω are averaged by integrating in E over one orbital period (from 0 to 2π).

This method reduces the evolution of a, e and ω to their mean components but to have an accurate model also oscillatory contributions must be considered:

$$x(E) = x_0 + \frac{\Delta x}{2\pi}(E - E_0) + K_x(\cos(E - \phi_x) - \cos(E_0 - \phi_x)) \tag{1.19}$$

in this case the term Δx, which define the mean component, can be obtained from the averaging procedure by solving two elliptic integrals, whereas the terms K_x and ϕ_x which define the oscillatory component can be retrieved through a fitting procedure over a set of numerical values obtained by integrating numerically over one revolution of the orbit in this way a general expression for a, e and ω as function of the only unknown E is obtained.

To get the final eccentric anomaly E at the end of the manoeuvre, Eq. (1.18) is integrated numerically using for a and e the expressions provided in Eq. (1.19).

Once the final E is retrieved, it is possible to compute the final a, e and ω from Eq. (1.19).

Lastly the evaluation of the variation of mean anomaly (δM) is computed as:

$$\delta M = (n_f - n_0)t_{CA} + n_0 t_0 - n_f t_f + \Delta M \tag{1.20}$$

where n_0 and n_f are the mean motion evaluated at the manoeuvre's initial and final times (t_0 and t_f respectively) which are the result of the change in mean motion of the orbit whereas ΔM is the variation introduced by the direct effect of CAM acceleration in the Gaussian equations; this last term is retrieved by integrating numerically the differential equation of M only along the last incomplete revolution.

The need to perform the numerical integration of the time law over $\Delta \mathrm{t}_{CAM}$ and of the mean anomaly over the last incomplete arc, together with the fitting process over a whole orbit revolution is what prevents the method from being fully analytical.

Tangential Analytical Model: 0th-Order Time Law

In the previous paragraph a SA method to compute the changes of KE has been shown, however this method relies on three different numerical integrations:

1. a, e and ω over one period to perform the fitting of the short periodic corrections;
2. The approximated time law over the whole LT arc to get the final eccentric anomaly;
3. The differential equation of M over the last incomplete revolution to determine the term ΔM;

In order to avoid these integrations, an analytical expression for the short periodic terms was proposed by Gonzalo et al. in [23].

Considering the same approximated time law as in the SA case, the following analytical expression for a and e as a particular case of Eq. (1.17) are obtained as function of the eccentric anomaly E:

$$a(E) = a_{ref} + \epsilon_t K_a E + \epsilon_t a_{osc}(E) \tag{1.21}$$

$$e(E) = e_{ref} + \epsilon_t K_e E + \epsilon_t e_{osc}(E) \tag{1.22}$$

where the reference values are those associated to a and e at E=0; K_a and K_e are associated to the mean component and are evaluated by solving two complete elliptic integrals of first and second kind whereas the short periodic terms are obtained as an expansion in small eccentricity without performing any fitting process; using these expressions, the final eccentric anomaly is computed through the approximated time law by means of a root finding problem:

$$\begin{split}\Delta t n_{ref} = E - e_{ref} \sin E + \epsilon_t \Big[E^2 \frac{3K_a}{4a_{ref}} - E \Big(K_e + \frac{3}{2} e_{ref} \frac{K_a}{a_{ref}} \Big) \sin E + \\ + \sum_{u=1} e_{ref}^{u-1} \sum_{v=1}^{u} \boldsymbol{M}_{uv}^{E} \cos(vE) \Big] \Big|_{E_0}^{E}\end{split} \tag{1.23}$$

the expressions for the different parameters can be found in [23]; the mean anomaly is then computed through the Kepler's law using the previous expressions for a and e.

However this time law is an approximation: the direct contribution of thrust on the eccentric anomaly E, which is related to the apse line rotation is not considered; so a correction in the implicit Eq. (1.23) is made by adding the following term in order to have a better accuracy:

$$\Delta\omega = \epsilon_t \frac{2\sqrt{1-e_{ref}^2}}{e_{ref}^2}\left(2a\sin\sqrt{\frac{1-e_{ref}cosE}{2}} - \sqrt{1-e_{ref}^2\cos^2 E}\right)\Big|_{E_0}^{E} \tag{1.24}$$

this is also the solution for the change in argument of pericenter, which is the osculating change in ω.

By adopting this correction, a better accuracy is reached, in particular the apse line correction reduces the error for quasi-circular orbits since the apse line becomes more sensitive to perturbation as the orbit becomes circular, where the apse line is not defined and the Gauss' equations become singular.

This new model requires only the numerical solution of an implicit equation and one key difference with the SA method is that it captures the frequencies of the short periodic corrections better than the sinusoidal fitting of the SA.

By analyzing the results shown in [23] a better accuracy with respect to the SA approach is also obtained.

Tangential Analytical Model: 1st-Order Time Law

To improve both accuracy and computational cost a fully analytical model has been presented in the previous paragraph; using this model the determination of the changes of KE is reduced to a root finding problem in the $t(E)$ time law.

Despite these advantages, there are two main limitations to take into account:

- The use of an approximate time law for the change of independent variable;
- The use of the only tangential component which still gives good solutions, but for a more accurate model also the normal and out-of-plane component need to be considered;

This paragraph describes the model developed by Gonzalo et al. in [22] where the following first order expression for the time law from Eq. (1.16) is adopted:

$$\frac{dt}{dE} = \frac{r}{an} + a_t \frac{2r^2 \sin\theta}{aben^2 v} + o(a_t^2) \tag{1.25}$$

It can be observed that the approximate time law introduced in Eq. (1.18) neglects the direct effect of thrust on E.

However, the averaged models for the KEs obtained so far include terms up to the first order in a_t, making the expansion in ϵ_t of the time law inconsistent with the expansion of the KEs.

To address this, a new expression is derived introducing the analytical solutions of a and e (already shown in Eq. (1.21) and Eq. (1.22)), into Eq. (1.25) and expanding in power series of the thrust parameter up to first order.

At the end two main contribution can be observed:

- The first one corresponds to the solution already presented in the analytical time law without the apse line correction;
- The second one arises by introducing the reference values of KE into the term depending on a_t of Eq. (1.25)

By integrating analytically, the following expression for the first-order time law is retrieved, which can be solved as before by adopting a numerical solver.

$$\Delta t^* n_{ref} = \left. \frac{C_1 - C_2}{e^2(ec_e - 1)\sqrt{-1 - \frac{2}{-1+ec_e}}} \right|_{E_0}^{E} \tag{1.26}$$

where the expressions for C_1, C_2 and c_e can be found in [22].

The results presented in [22] show that first-order model gives a better accuracy with respect to the zeroth-order with apse line correction, however as the orbit becomes circular the zeroth-order model outperform the first-order model for very high values of a_t, this suggests of using a zeroth-order time with apse line correction for the cases of quasi-circular orbits.

Normal Analytical Model

To have a more complete model for in-plane thrust, Gonzalo et al. developed an analytical model also for the normal thrust component [25].

This component causes changes only in eccentricity, pericenter anomaly and mean anomaly; by performing a change of variable in eccentric anomaly E using the time law in Eq. (1.16), the following expression for e, ω and t can be derived:

$$\begin{cases} \frac{de}{dE} = -\epsilon_n \sqrt{1-e^2} \frac{(1-e\cos E)\sin E}{\sqrt{\frac{1+e\cos E}{1-e\cos E}}} \\ \frac{d\omega}{dE} = \epsilon_n \frac{(e+\cos E)(1-e\cos E)^2}{e\sqrt{1-e^2\cos^2 E}} \\ \frac{dt}{dE} = \frac{r}{an} + a_n \frac{r^3(e+\cos\theta)}{a^2 b e n^2 v} \end{cases} \tag{1.27}$$

the equation in eccentricity can be integrated analytically, whereas the one in pericenter anomaly is derived by following a similar procedure used for a and e in the tangential case with an expansion in power series of e_{ref}:

$$\begin{aligned} e(E) =& e_{ref} + \frac{\epsilon_n \sqrt{1-e_{ref}^2}}{2e_{ref}} ((4 + e_{ref}\cos E)\sqrt{1 - e_{ref}^2 \cos^2 E} + \\ & + 6 \arctan \sqrt{\frac{1 + e_{ref}\cos E}{1 - e_{ref}\cos E}}) \Big|_{E_0}^{E} \end{aligned} \tag{1.28}$$

$$\begin{aligned} \omega(E) =& \omega_{ref} + \epsilon_n \frac{2\sqrt{1-e_{ref}^2}}{e_{ref}^2 \pi} \left((2 - e_{ref}^2) \mathrm{E} \left[-\frac{e_{ref}^2}{1-e_{ref}^2} \right] - 2\mathrm{F} \left[-\frac{e_{ref}^2}{1-e_{ref}^2} \right] \right) E + \\ & + \epsilon_n \omega_{osc}(E) \end{aligned} \tag{1.29}$$

The analytical expression to get the final E is then retrieved by solving a non-linear equation:

$$\Delta t n_{ref} = E - e_{ref}\sin E + \epsilon_n \left[E K_E^n + \sum_{u=1} e_{ref}^{u-1} \sum_{v=1}^{u} \boldsymbol{N}_{uv}^{E} \sin vE \right] \Big|_{E_0}^{E} \tag{1.30}$$

the expressions for the oscillatory component ω_{osc} can be found in [25] whereas those related to the time law are reported in Appendix A.

Although the optimal thrust direction to get higher miss distances tends to align with the tangential direction, it is important to have a good understanding of this component to define an overall model for the in-plane thrust.

1.4. Thesis Goal

1.4.1. Scope of the Work

The models shown until now do not take into account any orbital perturbation due to the complexity and the difficulties in their integration with analytical expressions, potentially leading to large errors in terms of position and PoC.

This thesis work is meant to provide lightweight and accurate algorithms for the design of low-thrust CAM when the satellite is subject to different orbital perturbations.

Analytical and SA perturbation models will be provided and integrated together to obtain an overall low-thrust perturbed model which will be used to perform parametric analysis and obtain optimal solutions in a short amount of time with respect to a fully numerical propagator; the region of interest for these models are limited to the only LEO and GEO regions where space congestion is a big issue.

In each of these regions, orbital perturbations are identified in order to decide which ones can be included in the SA model.

1.4.2. Original Contribution from the Thesis

In this work a new SA perturbed CAM model is developed by putting together different perturbation models developed by different authors with some modifications to their works to obtain lighter algorithms.

This perturbed model is integrated together with a CAM design algorithm and then tested for some optimisation problems in different orbits to assess its robustness, accuracy and low CPU cost.

1.4.3. Thesis Outline

After the introductory chapter regarding CAM's background and state of the art (Chapter 1.1), the document is followed by a chapter dedicated to the orbital perturbations of interest, with a brief summary on their effects and computation.

Chapter 3 is dedicated to a general overview on probability of collision, in particular to its definition and computation using different methods developed by authors such as Chan, Patera, Foster, etc.

Chapter 4 is the core of the work, where all of the developed perturbation models will be presented, each perturbation has its own section with details on how to model it, each of them is then tested against a numerical propagator to assess their accuracy on LEO and GEO.

Chapter 5 is dedicated to the application of the developed models for different optimisation problems through numerical examples and cases, at the end of the chapter pro and cons of the models will be analyzed highlighting their accuracy and CPU cost.

The last chapter (Chapter 6) is dedicated to the conclusions: advantages against a numerical propagator, final thoughts and future works.

2 | Orbit Perturbations

2.1. Introduction

Keplerian orbits are the closed form solutions of the two body equation of relative position:

$$\ddot{\vec{r}} = -\frac{\mu}{r^3}\vec{r} \tag{2.1}$$

this equation is based on the assumption that there are only two body objects in space, and that they only interact through their spherically symmetric gravitational fields.
Any effect that cause the motion to deviate from the Keplerian trajectory is known as **perturbation**; to account for them, the equation of motion is modified as follows [14]:

$$\ddot{\vec{r}} = -\frac{\mu}{r^3}\vec{r} + \vec{p} \tag{2.2}$$

where $\vec{p}$ is the vector of perturbing accelerations from all sources.
There are different perturbations the s/c is subject to, and their magnitudes vary with the distance between s/c and Earth; Figure 2.1, describes the various perturbations' magnitude acting on a satellite as function of its distance from the Earth's centre.
In this work only perturbations acting on LEO and GEO satellites will be considered to model the SA perturbed CAM propagator, in particular it is possible to notice that in LEO (h: 300-1000 km) the main contributions are given by atmospheric drag and gravity (which includes J_2 effect and higher order zonal harmonics) whereas for a GEO (h: 36000 km) the main contributions are given by third body perturbations (of Sun and Moon), solar radiation pressure (SRP), J_2 and $J_{2,2}$ effects.
All of these orbital perturbations, except of drag, can be described by a disturbing potential U which can be used in Lagrangian equations to calculate the change in elements.
In the case of non-conservative forces (e.g. atmospheric drag and thrust) it is possible to use instead a more general form based on the Gaussian equations to calculate the variation of orbital elements especially when dealing with LT CAMs.
This work aims to find a semi-analytical solution to these equations when the s/c is sub-

ject to a constant low thrust and to other orbital perturbations; one of the recurring methodology is based on averaging the Keplerian elements over one revolution in order to filter high frequency oscillations and decrease the CPU time, in particular using this SA approach it is possible to differentiate the various short-period, long-period and secular variations.

In the following sections, each perturbation source is studied separately.

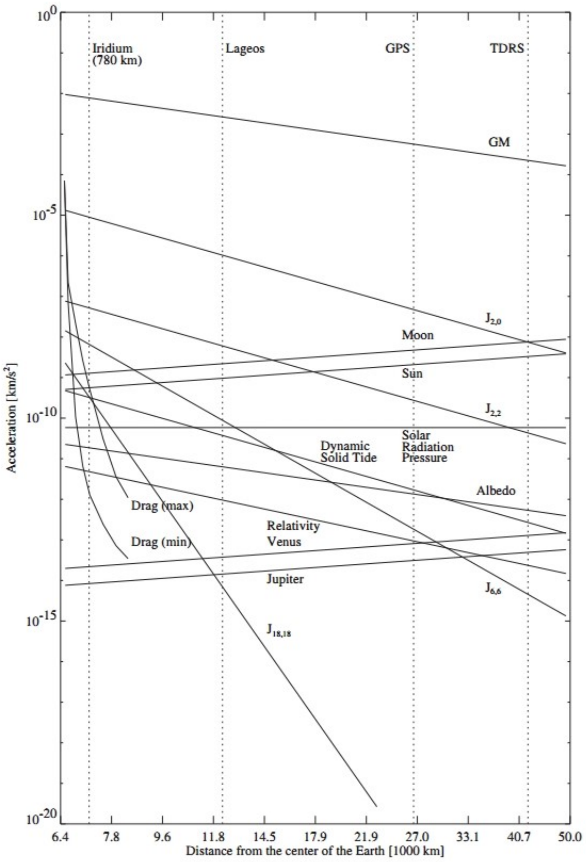

Figure 2.1: Magnitude of orbital perturbations [36].

2.2. Gravitational Perturbation

In the Keplerian model shown in Eq. (2.1), the Earth is considered as a perfect sphere which is not true in reality since the equator is twenty-one kilometers larger than polar radius.

Due to this lack of symmetry the gravity of an orbiting body is not directed towards the centre of the Earth; this perturbation can be described through a potential which is sum of two main terms which are the zonal and tesseral harmonics:

$$U(r, \phi, \lambda) = U_{zonal}(r, \phi) + U_{tesseral}(r, \phi, \lambda) \tag{2.3}$$

the s/c position in this case is described by the polar coordinates where r is the radial distance from the centre, λ is the longitude and ϕ is the latitude from the equator. Developing the terms for the zonal and tesseral harmonics, the following equation for the gravity potential is obtained :

$$U = -\frac{\mu}{r}\big[1 - \sum_{n=2}^{\infty} J_n\big(\frac{R_e}{r}\big)^n P_n(\sin\phi) + \sum_{n=2}^{\infty}\sum_{m=1}^{n} J_{n,m}\big(\frac{R_e}{r}\big)^n P_{n,m}(\sin\phi)\cos(m(\lambda - \lambda_{n,m}))\big] \tag{2.4}$$

where $P_{n,m}$(x) and P_n(x) are the associated Legendre function and the Legendre polynomial respectively, the values for J_n, $J_{n,m}$ and $\lambda_{n,m}$ can be instead retrieved from the geodesy data; in this work only the first term will be considered (J_2).

2.3. Atmospheric Drag

For the Earth, the space altitude begins beyond 100 km, air density at this altitude is sufficient to exert drag and cause aerodynamic heating of objects moving at orbital speeds. The drag lowers the speed and the height of a s/c with the orbit eccentricity that gets lower and lower; the drag effect is negligible for GEO satellites but not for LEO which orbits at very low altitudes; this perturbation is calculated as:

$$\vec{p}_{drag} = -\frac{1}{2}\rho v_{rel}\big(\frac{C_D A}{m}\big)\vec{v}_{rel} \tag{2.5}$$

$$\vec{v}_{rel} = \vec{v} - \vec{\omega}_e \times \vec{r} \tag{2.6}$$

where C_D is the drag coefficient, A/m is the ratio between the exposed surface and the mass of the s/c, ω_e is Earth angular velocity and ρ is the density of air at the given altitude.

There are different models that can be considered to define the air density; the most refined ones consider the influence of the air temperature, of solar cycles, etc. such as the Naval Research Laboratory Mass Spectrometer, Incoherent Scatter Radar Extended (NRLMSISE) model [39].

In this work it has been decided to adopt the simplest model which relate the atmospheric density to an exponential relation [14]:

$$\rho(h,t) = \rho_0 \exp\big[-\frac{h-h_0}{H}\big] \tag{2.7}$$

where ρ_0, h_0 are the reference values and H is the scale height; all these values are tabulated according to the *U.S. Standard Atmosphere.*
Atmospheric drag is the only non-conservative force so it cannot be expressed through a disturbing potential, in this case Gaussian equations are used and averaged to compute secular and long-term effects.

2.4. Solar Radiation Pressure

Solar radiation comprises photons, which are mass-less particles that carry energy and momentum, this flux of photons interacts with the s/c and exerts a pressure on it, this pressure is called solar radiation pressure (SRP) and at 1 UA is P_{SR}=4.56 μPa; by adopting the cannonball model where the s/c is assumed as a spherical object, the perturbing acceleration is computed as [14]:

$$\vec{p}_{SRP} = -\nu \frac{S}{c} \frac{C_R A}{m} \hat{\vec{u}} \tag{2.8}$$

where ν is the shadow function (0 in eclipse case, 1 otherwise), the ratio between S (energy flux per unit time per unit area) and c (speed of light) defines the solar radiation pressure P_{SR}, C_R and A are the reflectivity coefficient and the exposed area of the s/c (which is the area of a circle according to the cannonball model) and the versor $\hat{\vec{u}}$ defines the Earth-Sun direction.
The influence of SRP is more pronounced at higher orbital altitude, where the effect of atmospheric drag is negligible, in particular the altitude of 625 km defines the transition between the two forces; the effect of SRP on the s/c orbit depends on the area-to-mass ratio and on the reflectivity coefficient of the s/c itself; the higher the values the higher the magnitude of SRP and its effects on the orbit, which mainly leads to an increase of eccentricity especially for GEO satellites.
One of the main complications in the model is given by the eclipse condition: when the s/c is in Earth's shadow then the SRP is null; the following elementary procedure, defined by Vallado [42] based on a conical shadow with no penumbra, manages to identify whether a satellite is in Earth's shadow or not: defining as α the angle between the s/c and the Sun positions from Earth, α_1 the angle between the Sun position and its tangential point to the Earth and α_2 the angle between the s/c position and its tangential point to the Earth, if α_1+α_2<α then there is no line of sight and the SRP is 'off', otherwise the s/c is in the Sun's line of sight and the SRP is 'on'.
There are other models for the modeling of eclipses such as the cylindrical approximation, where the shadow created by Earth is a cylindrical projection of the Earth's diameter

along the Earth-Sun direction; and the conical approximation with penumbra described in [43].

The introduction of shadow is a complication also because it is difficult to define a proper potential since the perturbation is no more conservative.

2.5. Third Body Perturbation

Until now only two objects have been considered in the problem; however there are other different objects that exert an attractive force towards the satellite.

It is the case of the Moon and of the Sun, thanks to their mass (in case of the Sun) and closeness (in case of the Moon) the nominal orbit of the s/c is perturbed.

These perturbations tends to grow up as the distance from the Earth get larger and larger, especially in the case of GEO satellites.

The perturbation is defined as [12]:

$$\vec{p}_{3B} = \mu' \Big(\frac{\vec{r'} - \vec{r}}{(r' - r)^3} - \frac{\vec{r'}}{r'^3} \Big) \tag{2.9}$$

where the apex denotes the coefficients related to the third body; also in this case it is possible to associate a disturbing potential in the form of:

$$U(r, r') = \frac{\mu'}{r'} \Big(\big(1 - 2\frac{r}{r'} \cos\psi + \big(\frac{r}{r'}\big)^2 \big)^{-0.5} - \frac{r}{r'} \cos\psi \Big) \tag{2.10}$$

where ψ is the angle between the s/c position and the third body which can be compacted in a Taylor series as modelled by Kaufman and Dasenbrock [29]:

$$U_{3B}(r, r') = \frac{\mu'}{r'} \sum_{k=2}^{\infty} \delta^k F_k(A, B, e, E) \tag{2.11}$$

$$\begin{cases} \delta = \frac{a}{r'} \\ A = \hat{\vec{P}} \cdot \hat{\vec{r'}} \\ B = \hat{\vec{Q}} \cdot \hat{\vec{r'}} \end{cases} \tag{2.12}$$

where $\hat{\vec{P}}$, $\hat{\vec{Q}}$ are the eccentricity versor and the semi-latus rectum versor, respectively, expressed in ECI and F_k is instead the Kaufman-Dasenbrock function (full expression is available in [29]).

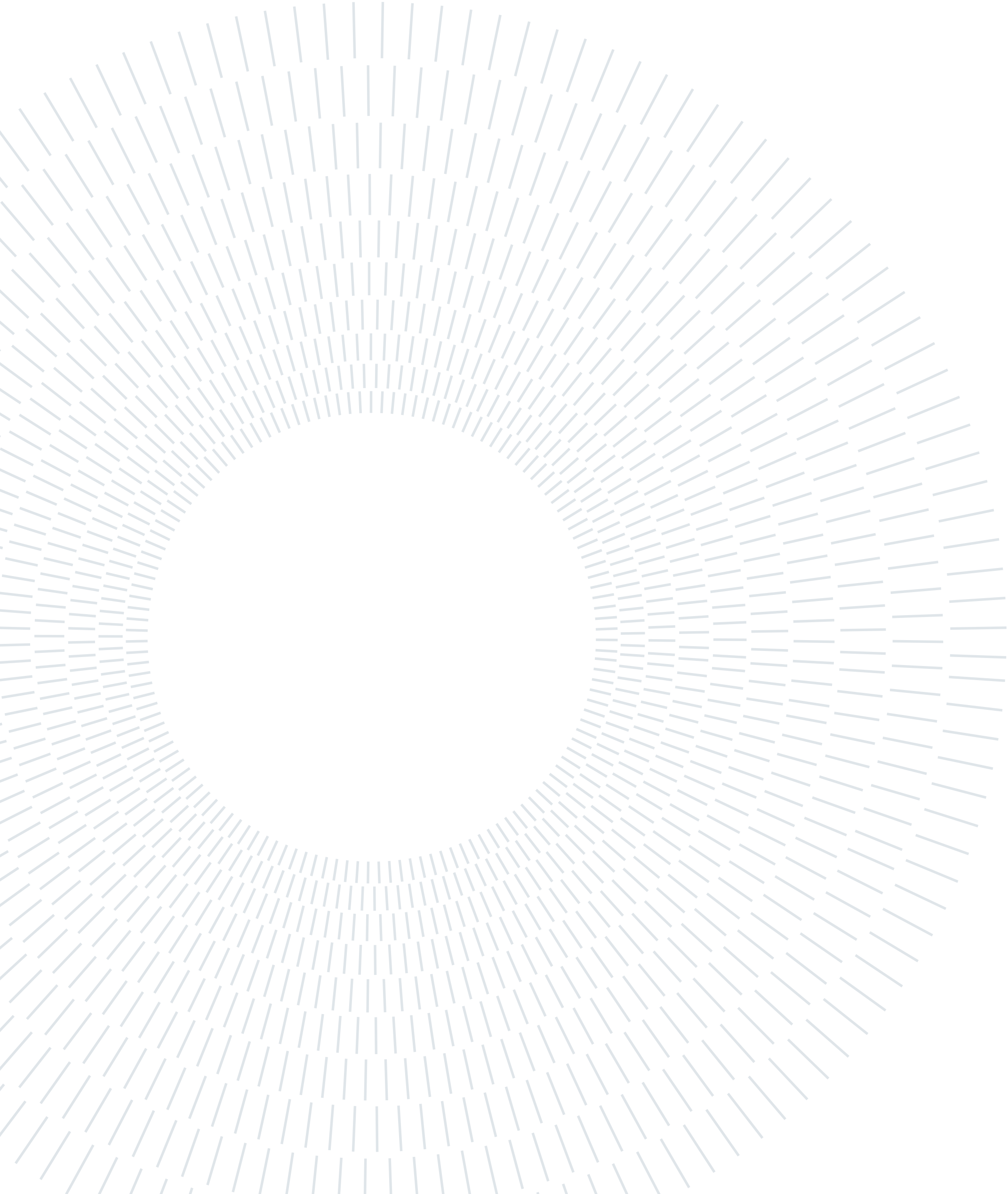

3 | Collision Probability

One of the most important actions to take into account, when a close conjunction is observed, is to compute the probability that a collision may occur, so an estimation of the probability of collision is needed.

When considering a close approach between two objects, that in this work will be considered as spheres of radius r_P (for the primary) and r_S (for the secondary), a collision will occur if the distance between them is equal or lower than the sum of the two radii; in case there are uncertainties in the state of the objects, then the problem is equivalent to studying the relative motion of a sphere with radius the sum of the two radii, and of a point where all of the uncertainty of the two objects is concentrated, the PoC is hence computed as:

$$\mathrm{PoC} = \iiint_V f_r(\vec{r})d\vec{r} \tag{3.1}$$

where $\vec{r}$ is the relative position of the primary with respect to the secondary, f_r is the associated probability function (e.g. a Gaussian distribution) and V the volume swept by the combined sphere centered in the primary.

Figure 3.1, shows the encounter plane with the combined covariance applied on the secondary object and the combined volume on the primary.

Before going into details it is fundamental to introduce the hypothesis of short-term encounters: a close encounter can be regarded as short-term depending not only on the relative encounter velocity but also on the size of the covariance ellipsoid.

For this purpose it is necessary to introduce the definition of covariance ellipsoid and encounter plane.

The **covariance ellipsoid** is a region defined by a given probability that depends on a scalar parameter, σ called *depth of intrusion* (or *standard deviation*), whose boundary is defined (assuming a Gaussian distribution) through:

$$(\vec{x} - \vec{\mu})^\top \boldsymbol{C}^{-1}(\vec{x} - \vec{\mu}) = \sigma^2 \tag{3.2}$$

where $\vec{\mu}$ is the expected value and $\boldsymbol{C}$ the covariance matrix which eigenvalues and eigenvectors give the magnitude of the ellipsoid's axes and directions respectively.

Along this contour the PoC is constant and it decreases for increasing σ as the size of the ellipsoid increases.

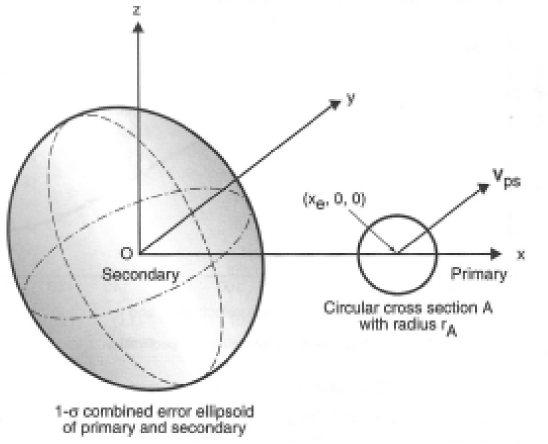

Figure 3.1: Encounter plane between two objects [40].

The **encounter plane** is instead the plane whose normal direction is aligned with the relative velocity vector of the two object at the CA and it contains the vector of minimum separation; there are several frames associated to this plane but the one that is adopted here is the one shown in Eq. (1.1) characterized by the directions $[\xi\ \eta\ \zeta]$.

Now it is possible to define the concept of short-term encounter: from a quantitative point of view, it is possible to define the conjunction duration t_c as the time required by the primary to move through the 1σ relative position uncertainty ellipsoid in the η direction [7]:

$$t_c = \frac{2\sigma_\eta}{||\vec{v}_P - \vec{v}_S||} \tag{3.3}$$

In this way, a short-term encounter is characterized by:

$$\epsilon_c = \frac{t_c}{T_P} \ll 1 \tag{3.4}$$

where T_1 is the orbital period of the primary body; typical values for ϵ_c are in the order of 10^{-3} or lower.

If the hypothesis of short-term encounter is satisfied then the relative motion, described before, approaches to a rectilinear one and the volume approaches to that of a cylinder, in this way is possible to approximate the integral in Eq.(3.1) to a 2D one, defined as:

$$\begin{aligned} \mathrm{PoC} = \iint_A \frac{1}{2\pi\sigma_\xi\sigma_\zeta\sqrt{1-\rho_{\xi\zeta}^2}} \exp\Bigg\{ - \Bigg[\left(\frac{\xi-\xi_e}{\sigma_\xi}\right)^2 + \left(\frac{\zeta-\zeta_e}{\sigma_\zeta}\right)^2 + \\ - 2\rho_{\xi\zeta}\frac{\xi-\xi_e}{\sigma_\xi}\frac{\zeta-\zeta_e}{\sigma_\zeta}\Bigg] \frac{1}{2(1-\rho_{\xi\zeta}^2)}\Bigg\} d\xi d\zeta \end{aligned} \tag{3.5}$$

where the subscript e indicates the expected closest approach relative position, A is a circular domain of radius s_a (given by sum of the two radii) and σ_ξ, σ_ζ and $\rho_{\xi\zeta}$ are related to the relative position covariance matrix in the B-plane axes.

There are several models, both numerical and analytical, for the computation of the PoC: the one developed by Chan [11], through some manipulations, can be approximated to a Rician integral; the model of Serra [41] is a general case of Chan's model; the models of Foster [16] and Alfano [4] require less manipulation but they are based on solving a 2D integral whereas the model developed by Patera [38] is based instead on a contour integral; Monte Carlo analysis can also be used in order to compute the PoC starting from random sampling points of the error ellipsoid defined in Eq. (3.2).

Further details on each of the models listed above will be given in the next sections.

Other models exist, such as Akella's and Alfriend's [1] or Garcia-Pelayo's [18] models, but they will not be discussed.

3.1. Chan's Model

In the model developed by Chan, the computation of Eq. 3.5 is equivalent of integrating a properly scaled isotropic Gaussian distribution over an elliptical cross-section; if this one is approximated to a circular cross-section of equal area, then the computation of PoC reduces to a Rician integral:

$$\mathrm{PoC}(u,v) = e^{-v/2}\sum_{m=0}^{\infty}\frac{v^m}{2^m m!}\left(1 - e^{-u/2}\sum_{k=0}^{m}\frac{u^k}{2^k k!}\right) \tag{3.6}$$

where u represents the ratio between the circular cross sectional area and the 1σ covariance ellipse:

$$u = \frac{s_a^2}{\sigma_\xi\sigma_\zeta\sqrt{1-\rho_{\xi\zeta}^2}} \tag{3.7}$$

and v is the square of the *depth of intrusion*:

$$v = \left[\left(\frac{\xi_e}{\sigma_\xi} \right)^2 + \left(\frac{\zeta_e}{\sigma_\zeta} \right)^2 - 2\rho_{\xi\zeta} \frac{\xi_e}{\sigma_\xi} \frac{\zeta_e}{\sigma_\zeta} \right] \frac{1}{1-\rho_{\xi\zeta}^2} \tag{3.8}$$

These formulas are valid for a general case with a not-isotropic, not-diagonal covariance matrix where the isotropic solution (σ_ξ=σ_ζ=σ) is a particular case.
A good approximation of PoC, for small values of u can be reached if the series is truncated after three or higher terms.

3.2. Serra's Model

This method allows to compute PoC for short-term encounters under Gaussian distributed uncertainties.
Serra's can be considered a general case of Chan's method: the model, computed as a product between an exponential term and a convergent power series with positive terms obtained through Laplace transform, provides analytical bounds on the truncation error, does not need any approximation of the integral and performs better, compared to the previous methods; for its formulation the PoC in Eq. (3.5) is arranged in a new reference frame in order to cancel the cross-term of the covariance and then it is integrated over the circular domain of radius s_a defined in the collision plane:

$$\mathrm{PoC} = g(s_a^2) = \frac{1}{2\pi\sigma_x\sigma_y} \int_A \exp\Big\{ -\frac{1}{2} \big[\big(\frac{x-x_e}{\sigma_x}\big)^2 + \big(\frac{y-y_e}{\sigma_y}\big)^2 \big] \Big\} dxdy \tag{3.9}$$

where the domain A is defined by a closed disk centered in the origin of radius s_a, the PoC as mentioned before is given by the product between an exponential and a convergent series:

$$\mathrm{PoC} = g(s_a^2) = f(s_a^2)\exp(-ps_a^2) \tag{3.10}$$

$$p = \frac{1}{2\sigma_y^2} \tag{3.11}$$

$$f(s_a^2) = \sum_{k=0}^{\infty} \beta_k s_a^{2k} \tag{3.12}$$

The full expression for the different parameters are shown in [41]; at the end the PoC according to Serra's method is computed as:

$$\mathrm{PoC} = g(s_a^2) = \exp(-ps_a^2) \sum_{k=0} \beta_k s_a^{2k} \tag{3.13}$$

3.3. Patera's Model

Chan showed that it is possible to combine the error covariance matrices of two objects if they are statistically independent; this combined covariance matrix has an associated 3D probability density function (PDF) that represents the uncertainty in the relative position between the two objects; as mentioned before the problem can be reduced to a two-dimensional one by eliminating the dimension parallel to the relative velocity (η-direction), the computation of the PoC is then reduced to a 2D integral over a circular region in the B-plane.

In Patera's methodology this area integral is computed as a path integral around the perimeter of the hard-body (the body with the combined radii), this one is obtained by performing a coordinate rotation followed by a scale change to make the density distribution symmetric which enables the 2D integral to be reduced to a 1D path integral; the coordinate rotation does not alter the size of the body but its location whereas the scale change alters both position and size of the hard-body circle.

The problem is then reduced to integrating a symmetric probability function over an elliptical region :

$$\mathrm{PoC} = -\frac{1}{2\pi}\oint_{ellipse} \exp(-\alpha r^2)d\theta \tag{3.14}$$

this formula is valid in the case the hard-body does not belong to the origin, if this happens the adopted formula is:

$$\mathrm{PoC} = 1 - \frac{1}{2\pi}\oint_{ellipse} \exp(-\alpha r^2)d\theta \tag{3.15}$$

where α is a parameter that depends on the coordinate rotation and the subsequent scale change to get a symmetric PDF; this methodology does not require any additional assumption, it is computationally efficient and applicable to satellites of irregular shape.

3.4. Alfano's Model

In this methodology the double integral is reduced to a single integral by using the error function whose integral is evaluated through Simpson's one-third rule.

Also in this case the objects are modelled as spheres with their combined size and covariance; by starting from Eq. (3.5) a change of reference frames is performed in order to get a diagonal covariance, this new frame is defined by x'y':

$$\mathrm{PoC} = \frac{1}{2\pi\sigma_{x'}\sigma_{y'}}\int_{-s_a}^{s_a}\int_{-\sqrt{s_a^2-x^2}}^{\sqrt{s_a^2-x^2}} \exp\Big\{-\frac{1}{2}\Big[\Big(\frac{x'+x'_e}{\sigma_{x'}}\Big)^2+\Big(\frac{y'+y'_e}{\sigma_{y'}}\Big)^2\Big]\Big\}dx'dy' \tag{3.16}$$

where the subscript e indicates the secondary body's coordinates and s$_a$ the combined radius; the equation is then reduced to a single integral through the use of the error function *erf* and then to a n-series expression which is then computed numerically through Simpson's rule which is chosen for its simplicity and computational efficiency; at the end the PoC is computed as:

$$\mathrm{PoC} = \frac{dx'}{3\sqrt{8\pi}\sigma_{x'}}(m_{even}+m_{odd}+m_0) \tag{3.17}$$

the odd, even and zeroth order expressions are shown in [4] whereas *dx'* is computed as:

$$dx' = \frac{s_a}{m} \tag{3.18}$$

with m that defines the accuracy of PoC and it is defined as:

$$m = \mathrm{int}\left(\frac{5s_a}{\min(\sigma_{x'},\sigma_{y'},\sqrt{x_e'^2+y_e'^2})}\right) \tag{3.19}$$

3.5. Foster's Model

This method was developed in 1992 and used by NASA for analyzing the hazard of space debris on the International Space Station (ISS); the mathematical model is based on representing the position distribution by a bi-variate normal distribution and integrating it over a circular domain defined by the hard-body sphere of radius s_a; the method is based on the following process:

1. Position distribution of the secondary relative to the primary object is described by a 2D normal distribution along the estimated CA on the B-plane ξ, η, ζ;
2. The σ's associated to the bi-variate function are extracted from the σ's of primary and secondary objects;
3. A per-event PoC is calculated for the primary sphere;

In particular for the calculation of PoC in point 3, the following formula is used:

$$\begin{aligned}\text{PoC} =& \frac{1}{2\pi\sigma_\xi\sigma_\zeta}\exp\Big\{-\frac{R^2}{2}\big[\big(\frac{\sin\phi}{\sigma_\xi}\big)^2+\big(\frac{\cos\phi}{\sigma_\zeta}\big)^2\big]\Big\} \\ & \int_0^{s_a}\int_0^{2\pi}\exp\big[rR\big(\frac{\cos\phi\cos\theta'}{\sigma_\zeta^2}+\frac{\sin\phi\sin\theta'}{\sigma_\xi^2}\big)+ \\ & -\frac{r^2}{2}\big(\frac{\sin^2\theta'}{\sigma_\xi^2}+\frac{\cos^2\theta'}{\sigma_\zeta^2}\big)\big]rdrd\theta\end{aligned} \tag{3.20}$$

where R and ϕ define the polar coordinates of the miss distance whereas r and θ' define the polar coordinates of the actual position in the B-frame.

The integral can be solved numerically adopting a proper discretisation for both r and θ' variables.

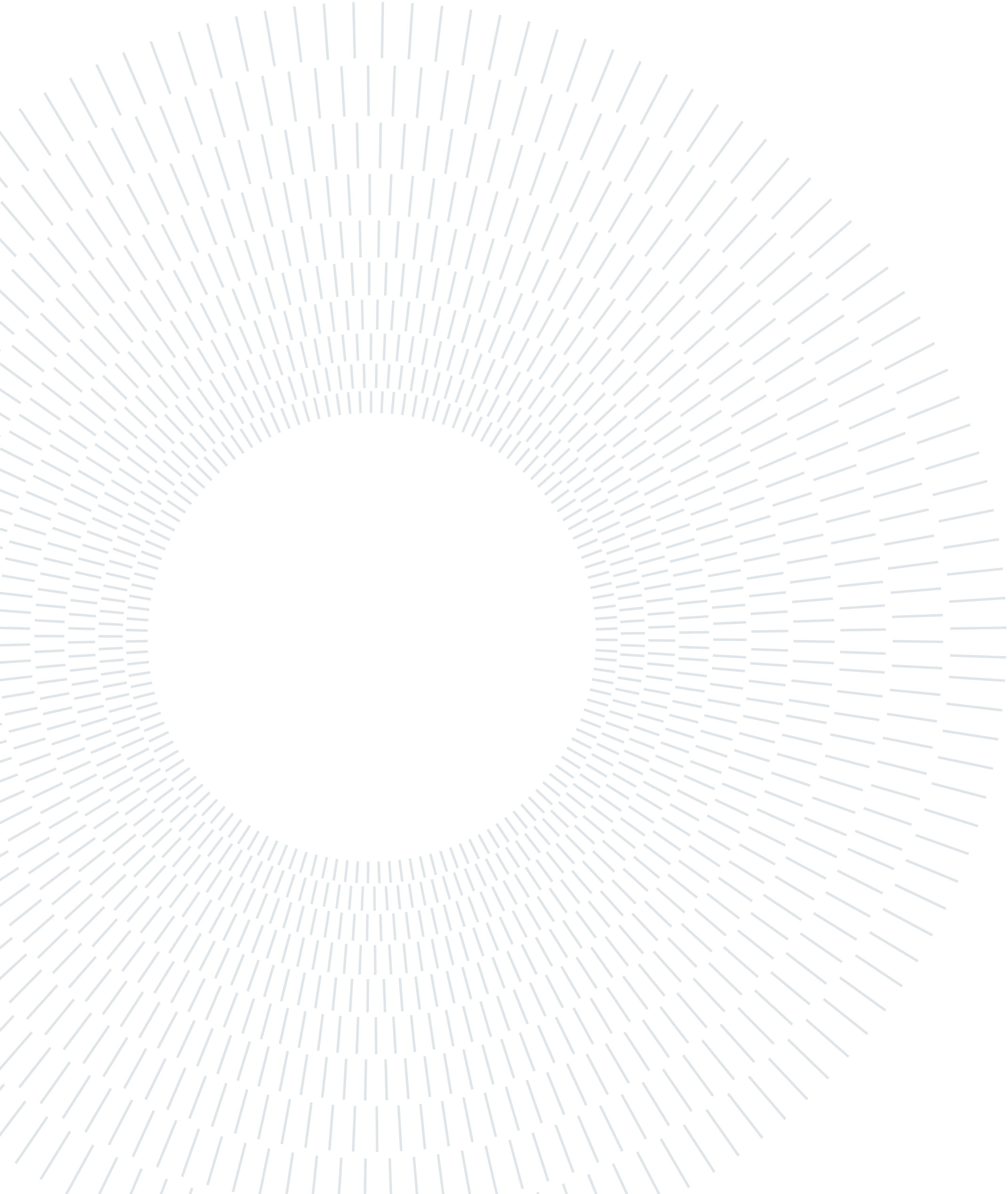

4 | Perturbation Models

The goal of this thesis work is to obtain lightweight and accurate perturbed CAM algorithms which can be used for the fast computation of parametric analysis; the orbits that will be taken into account belong to LEO (from 300 to 1000 km of altitude) and GEO (at 36000 km of altitude) regions so it is essential to know the main perturbations acting on these regions.

Analyzing Fig. 2.1 and taking into account that the maximum time for a CAM manoeuvre is of a few hours, it is possible to neglect those perturbations characterized by long-periodic effects on the orbit (an example is $J_{2,2}$ harmonic for GEO).

At the end it is stated that the most relevant perturbations on LEO are atmospheric drag and J_2 effects, whereas on GEO there are solar radiation pressure, luni-solar and J_2 effects.

In the next paragraphs accurate and analytical algorithms will be developed for each of these perturbations, the accuracy of each model will be tested by plotting the absolute error in position between the analytical and numerical models whose solution is derived by solving the six Gaussian Ordinary Differential Equations (ODE) through *ode45* of *MATLAB* using an *abstol* and *reltol* of 1e-12.

4.1. Analytical J_2 Models

Earth gravitational effects are very important when dealing with orbital perturbation, in particular the second zonal harmonic (J_2 harmonic) is the most relevant orbital perturbation; on LEO it has an order of magnitude from 10^{-5} to 10^{-6} km/s^2 whereas on GEO its effect is much weaker but still relevant with respect to the other perturbation, with a magnitude of 10^{-8} km/s^2.

During the past years, different analytical algorithms to model this effect were developed such as the first-order models of Brouwer [10] and Lyddane [35], the second-order's of Kozai [32] and Aksnes [2] and the third-order's of Kinoshita [30]; each of these models has been validated by performing numerical tests on each region, in order to choose the best one to adopt for the SA propagator.

The results given by each model are briefly summarized below:

- **Brouwer's model**: it is a first order model based on Delaunay's elements (but there is a version with Keplerian elements too) and it is the fastest one from a computational point of view; however the accuracy is really poor, both for LEO and GEO (reaching errors in position of 200 m and 500 m respectively).
- **Lyddane's model**: it is based on a first order model and it is a particular case of Brouwer's model optimized for very low eccentricities and inclinations by adopting the Poincarè's elements.
  The model is less fast than Brouwer's but the accuracy on GEO is really good with errors that are below one meter, however on LEO the errors are still too large (150-200 m).
- **Kozai's model**: it is a second order model based on Delaunay's elements and it requires more time with respect to Brouwer's.
  The errors on GEO are in the order of 400-500 m whereas on LEO are in the order of 80-100 m but only for $e>0.02$ otherwise they increase exponentially.
- **Aksnes's model**: it is a second order model based on Hill's elements.
  The errors in this case are very small both on GEO and LEO (in the order of a few centimeters), however this is the heaviest model from a computational point of view.

Each model has its own accuracy and computational cost (which increase as the order of the model increases too).
For the region of our interest it was adopted for LEO the analytical model of Aksnes whereas for GEO the model developed by Lyddane which gives good results when dealing with small inclinations and eccentricities.
More details on the two models are given in the next sections.

4.1.1. Aksnes Model on LEO

Due to the high order of magnitude of J_2 effect on the LEO zone, a first-order solution is not accurate enough to model the perturbation, hence a second-order solution was developed based on the analytical model of Aksnes which is lighter and more accurate with respect to the one developed by Kozai.
Aksnes' J_2 model has no singularity at zero eccentricity and includes short and long periodic terms up to the second-order whereas the secular components are developed up to the third-order; starting from a set of initial Keplerian mean elements the algorithm

computes the state at a given time in terms of modified Hill's variables; one of the main drawback of this algorithm is that it starts from the mean elements which can be retrieved from the osculating ones solving a non-linear equation.
Below it is reported the overall algorithm, more information are also available in [2]:

Algorithm 4.1 Aksnes J_2 Algorithm

```
Start from initial osculating element $\alpha_0$ and propagation time $\Delta$t.
Compute the mean elements $\overline{\alpha}_0$ from the initial Keplerian osculating elements solving the following non-linear system:
    $$F(\overline{\alpha}_0) = \overline{\alpha}_0 + \Delta\overline{\alpha}_{sp} + \Delta\overline{\alpha}_{lp} - \alpha_0 = 0 \tag{4.1}$$
Propagate the initial mean elements at the wanted time $\Delta$t by adding the 3rd-order secular terms.
    $$\overline{\alpha}(t) = \overline{\alpha}_0 + \dot{\alpha}_{sec}\Delta t \tag{4.2}$$
Compute the modified Hill's variables $\overline{\alpha}_H$(t) from the propagated mean Keplerian elements:
    $$\alpha_H = \begin{bmatrix} r & \dot{r} & \sqrt{\mu p} & \sqrt{\mu p}\cos i & \Omega & \omega + \theta \end{bmatrix} \tag{4.3}$$
Compute the second-order short and long periodic terms and add them to the Hill's variables to retrieved the final osculating state in terms of Hill's elements:
    $$\alpha_H(t) = \overline{\alpha}_H(t) + \Delta\overline{\alpha}_{H,sp} + \Delta\overline{\alpha}_{H,lp} \tag{4.4}$$
Convert the Hill's variables to the desired elements (Keplerian, Cartesian etc.)
```

To assess the accuracy of the model, the algorithm was run for different values of semi-major axis and eccentricities typical of the LEO region, Figure 4.1 shows the maximum absolute error in position as function of a and e between the numerical model and the analytical one over five revolutions of the orbit.
It can be noticed that the error is in the order of a few centimeters making Aksnes' algorithm an accurate model to compute the Keplerian elements subject to J_2 perturbation.

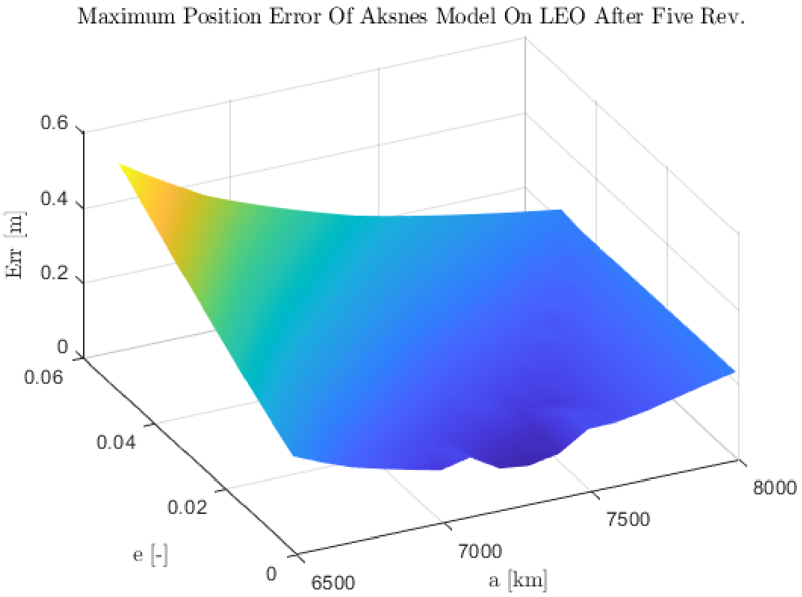

Figure 4.1: Error in position of Aksnes' model.

4.1.2. Lyddane Model on GEO

For the modeling of J_2 effect on GEO a 1st-order model was adopted, precisely Lyddane's model, the reason behind this choice is given by the fact that the second zonal harmonic is much weaker in GEO than LEO so a good accuracy can be reached in a short time with respect to a second-order model.

Lyddane gives very good results when dealing with very small inclinations and eccentricities which are typical of a GEO.

Lyddane's model can be considered as a particular case to Brouwer's analytical J_2 model for $e{\approx}0$ and $i{\approx}0$, the steps are similar to the one developed by Aksnes with the only exception that the final state is expressed through Poincaré's canonical elements:

$$\alpha_P = \begin{bmatrix} a & \Omega + \omega + M & e\cos M & e\sin M & \sin\frac{i}{2}\cos\Omega & \sin\frac{i}{2}\sin\Omega \end{bmatrix} \tag{4.5}$$

the short periodic terms of Keplerian elements ($\delta\alpha$) are computed as shown in [10] (and can also be found in Appendix B together with the secular expressions), then they are integrated together to compute the final state in terms of Poincaré variables:

$$\begin{cases} a = \overline{a} + \delta a \\ \Omega + \omega + M = \overline{\Omega} + \overline{\varpi} + \overline{M} + \delta(\Omega + \omega + M) \\ e \cos M = (\overline{e} + \delta e) \cos \overline{M} - \overline{e} \delta M \sin \overline{M} \\ e \sin M = (\overline{e} + \delta e) \sin \overline{M} + \overline{e} \delta M \cos \overline{M} \\ \sin \frac{i}{2} \cos \Omega = [\sin \frac{\overline{i}}{2} + \frac{1}{2} \cos \frac{\overline{i}}{2} \delta i] \cos \overline{\Omega} - \sin \frac{\overline{i}}{2} \delta \Omega \sin \overline{\Omega} \\ \sin \frac{i}{2} \sin \Omega = [\sin \frac{\overline{i}}{2} + \frac{1}{2} \cos \frac{\overline{i}}{2} \delta i] \sin \overline{\Omega} + \sin \frac{\overline{i}}{2} \delta \Omega \cos \overline{\Omega} \end{cases} \tag{4.6}$$

where the overlined element $\overline{\alpha}$ represent a generic mean element propagated for the wanted Δt according to Eq. (4.2).

As done previously, to assess the accuracy of the model, the algorithm was run for a given range of eccentricities and inclination typical of a GEO region (semi-major axis is fixed to 42165 km), Figure 4.2 shows the maximum absolute error in position between the numerical and analytical models over one revolution of the orbit.

Also in this case it is noted that the error is very small (below one meter) in the eccentricity and inclination range of interest.

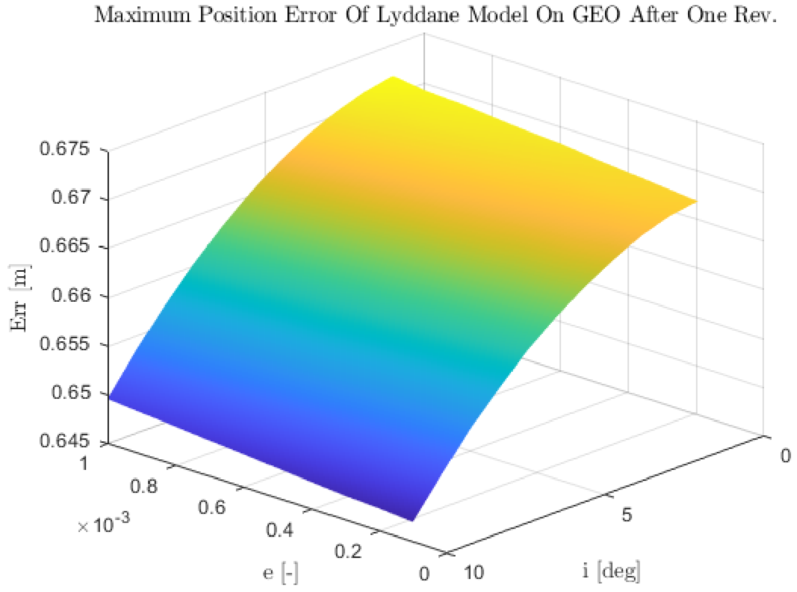

Figure 4.2: Error in position of Lyddane's model.

4.2. Semi-Analytical Atmospheric Drag Models

Another important perturbation to be considered when dealing with s/c in the LEO region is the atmospheric drag, the main effects of this perturbation is a continuous decrement of semi-major axis and eccentricity which can lead to orbit decay; to avoid this problem and reduce its effects, most of the satellite in LEO, especially those very close to Earth, are quasi-circular (e.g. ISS orbit) however drag effects are still relevant and must be taken into account.

For the modeling of atmospheric drag, a SA approach developed by King-Hele will be used [26], this method is not fully analytical since it consists on the numerical integration of equations but it is still lightweight with respect to a fully numerical model since the short periodic terms are removed by averaging the equations, moreover the equations to be integrated are only three since atmospheric drag has relevant effects only on semi-major axis, eccentricity and mean anomaly.

King-Hele developed two different models for the low and high eccentricity cases, in this work both the models will be presented highlighting the position error of both for a given range of semi-major axes and eccentricities, both models are also developed considering the exponential atmospheric model shown in Eq. (2.7)

4.2.1. Low Eccentricity Drag Model

The following model is adopted when dealing with very small eccentricities, in this case a series expansion in e is performed and then integrated using the modified Bessel function of first kind $I_n(z)$, where z is an auxiliary variable defined as $z{=}ae/H$ and H is the scale height at the perigee altitude.

The final state is retrieved by solving the following ODE of three equations on semi-major axis, eccentricity and mean anomaly:

$$\begin{cases} \frac{da}{dt} = -\frac{A}{m} C_D \sqrt{\mu a} \rho(h_p) \exp(-z) [\vec{e}^\top \boldsymbol{K^l_a} \vec{I}] \\ \frac{de}{dt} = -\frac{A}{m} C_D \sqrt{\frac{\mu}{a}} \rho(h_p) \exp(-z) [\vec{e}^\top \boldsymbol{K^l_e} \vec{I}] \\ \frac{dM}{dt} = \sqrt{\frac{\mu}{a^3}} \end{cases} \tag{4.7}$$

The expressions for the vectors $\vec{e}$ and $\vec{I}$ and the matrices $\mathbf{K}^l_a$ and $\mathbf{K}^l_e$ are available in Appendix C.1.

Lastly, to validate the model, the maximum absolute error between the numerical and SA model over five periods of a LEO subject to only atmospheric drag was plotted for different a and e.

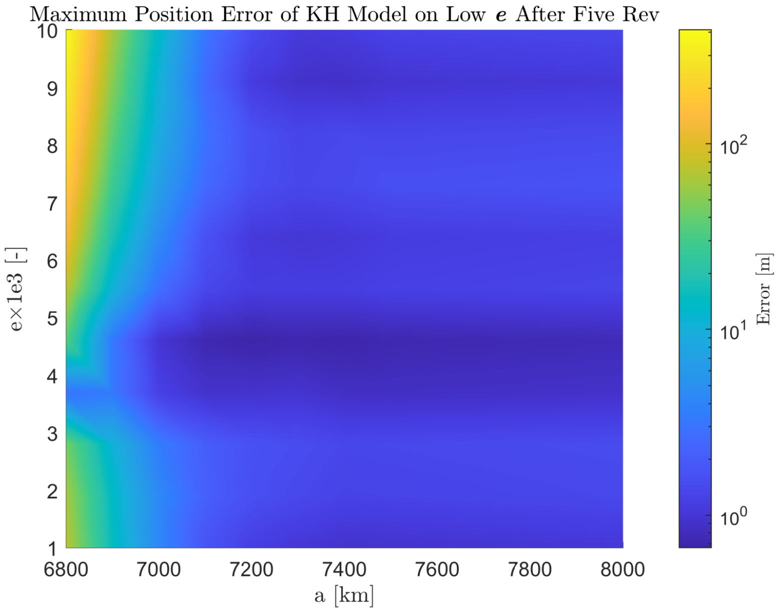

Figure 4.3: Error in position of KH low eccentricity model.

Figure 4.3 is obtained by considering an area-to-mass ratio of 0.005 m^2/kg and a drag coefficient of 2.0 which are typical values for a LEO satellite; it is shown that the error reaches very large values for low a and high e; this is mainly due to two limitations of KH model:

1. The model consists on an averaged solution which discards short periodic terms, these terms tends to be significant for high eccentricity cases, especially when the drag effects at perigee are relevant;
2. The density is evaluated only at the perigee height, so the larger the difference between perigee and apogee altitudes, the larger the error;

However as said previously most of the LEO satellites (especially those really close to Earth) are quasi-circular to minimise drag effects which can lead to orbital decay, so the model is still really good for low a and low e with a maximum error of 50-60 meters; for a>7000 km the model works perfectly for the given range of e which can be enlarged by adopting the high eccentricity KH model shown in Section 4.2.2.

4.2.2. High Eccentricity Drag Model

The high eccentricity model can be used when dealing with large e, however as said before the eccentricity cannot grow too much due to the model limitation especially in the low a region.

In this model instead of performing a series expansion on e, the expansion is performed over a λ parameter defined as $1/z$(1-e^2) where z is the same auxiliary variable defined in the low eccentricity case; then, as before, the final state is retrieved by solving numerically the following ODE:

$$\begin{cases} \frac{da}{dt} = -\frac{A}{m} C_D \sqrt{\mu a} \rho(h_p) \sqrt{\frac{2(1+e)}{\pi z(1-e)}} (1+e)[\vec{e}^{\top} \boldsymbol{K_a^h} \vec{r}] \\ \frac{de}{dt} = -\frac{A}{m} C_D \sqrt{\frac{\mu}{a}} \rho(h_p) \sqrt{\frac{2(1+e)}{\pi z(1-e)}} (1-e^2)[\vec{e}^{\top} \boldsymbol{K_e^h} \vec{r}] \\ \frac{dM}{dt} = \sqrt{\frac{\mu}{a^3}} \end{cases} \tag{4.8}$$

The expressions for the vectors $\vec{e}$ and $\vec{r}$ and the matrices $\mathbf{K}_a^h$ and $\mathbf{K}_e^h$ are available in Appendix C.2.

Lastly, as done previously, to validate the model, the maximum absolute error between the numerical and SA model over five periods of a LEO subject to the only atmospheric drag was plotted for different a and e, also in this case the values adopted for the drag coefficient and the area-to-mass ratio are respectively 2.0 and 0.005 m^2/kg.

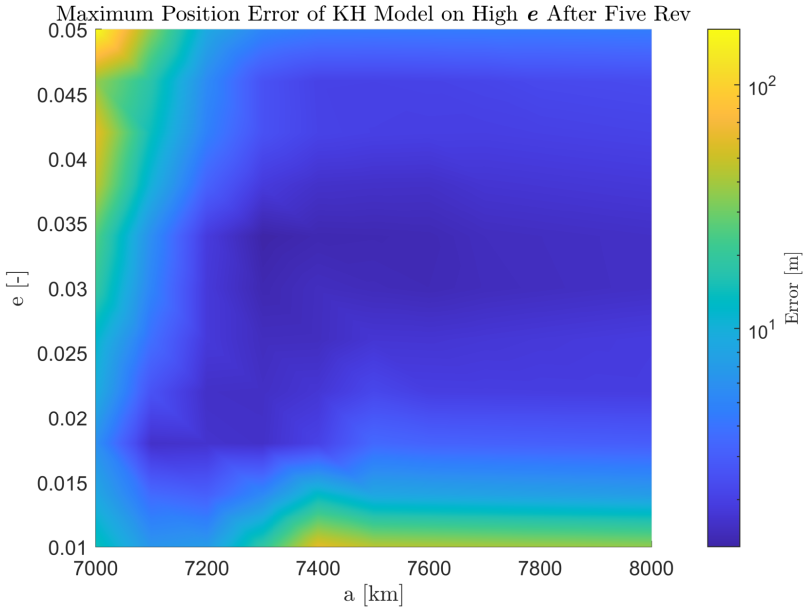

Figure 4.4: Error in position of KH high eccentricity model.

Figure 4.4 shows that a good approximation can be reached for e>0.01, also in this case the error tends to grow up starting from the low a and high e region, however the error remains globally lower than 10-20 meters.

4.3. Analytical Solar Radiation Pressure Model

SRP is one of the main perturbations acting on GEO.
To model this perturbation, the works developed by Kozai [31] and Aksnes [3] (who basically corrected some errors present in Kozai's model) are considered.
Kozai computed the variations in Keplerian elements by integrating analytically the Gaussian equations considering all terms constant except the true anomaly θ, once the variations are computed they are added to the initial mean Keplerian element to compute the final state at the wanted time.
Despite its simplicity this model has three main limitations:

1. Eclipse conditions are not modelled: to compute the extremes of the sunlight arc a quartic non-linear equation must be solved which is computationally too expensive; however this simplification will not introduce a big error in the model;
2. Since the perturbation's magnitude is really low (10^{-10} km/s^2 considering an area-to-mass ratio of 0.01 m^2/kg) the initial mean elements are approximated with the initial osculating ones;
3. The Sun-Earth vector is considered to be constant during the whole interval, this approximation is valid since the characteristic interval for a low-thrust CAM is less than a day;

Taking into account these limitations, the short periodic variations can be calculated (full expression are available in Appendix D with some corrections) to retrieve the final state. To compute the Sun's ephemerides, precisely the ecliptic longitude λ_{sun} and the obliquity ϵ) and the SRP magnitude the following formulae, taken from [3], are adopted:

$$\begin{cases} d = MJD - 15019.5 \\ \epsilon = 23.44^\circ \\ M_{sun} = 358.48^\circ + 0.98560027^\circ d \\ \lambda_{sun} = 279.70^\circ + 0.98564734^\circ d + 1.92^\circ \sin M_{sun} \end{cases} \tag{4.9}$$

$$\begin{cases} \frac{a_{sun}}{r_{sun}} = \frac{1+0.01672 \cos\left(M_{sun}+1.92^\circ \sin M_sun\right)}{0.99972} \\ a_{SRP} = C_R \frac{A}{m} P_{SR} \left(\frac{a_{sun}}{r_{sun}}\right)^2 \end{cases} \tag{4.10}$$

where MJD is the modified Julian day and P_{SR} is the Sun pressure exerted on Earth's surface of 4.56×10^{-6} Pa; these formulae will be used both for the numerical and analytical models in order to reduce the differences between them.

The algorithm was run for different ranges of GEO's eccentricities and inclinations (considering A/m=0.01 m^2/kg and C_R=1.5) to evaluate the error over one revolution of the model starting from an initial propagation date fixed to the 1st March 2023, Figure 4.5 shows that the error is bounded to 150 meters and increases slightly towards the low-eccentricity high-inclination region.

However, this error does not take into account the different starting times: results given on a certain date are not the same for another one, so the algorithm was run for different epochs of year 2023 and also in this case the maximum absolute error over one revolution was plotted considering e=0.0005, i=1 deg, A/m=0.01 m^2/kg and C_R=1.5; Figure 4.6 shows how significantly the error varies according to the starting point, in particular an oscillatory behaviour is detectable over the whole year leading to errors that grow from 60 up to 200 meters.

Despite this large error, the model is still accurate enough to model a perturbed low-thrust GEO CAM considering also all the simplifications that have been done.

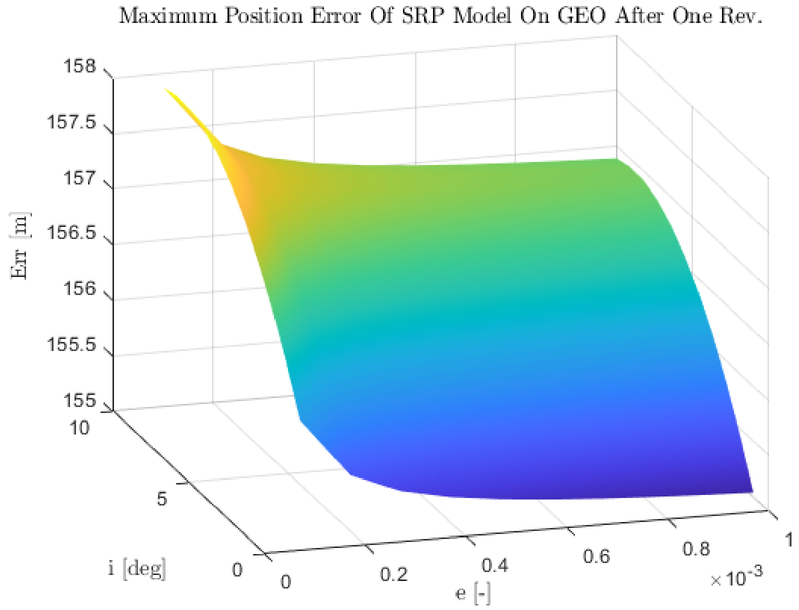

Figure 4.5: Error in position of SRP model.

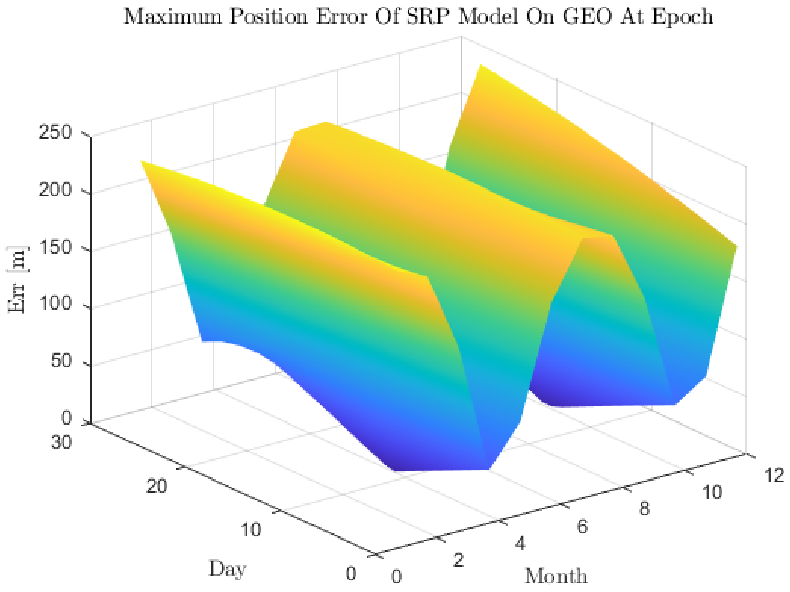

Figure 4.6: Error in position of SRP model at epoch.

4.4. Analytical Sun Perturbation Model

Last of the perturbation to be modelled on GEO is the luni-solar perturbation, this perturbation is caused by the interaction of the satellite with a third body (Sun and Moon in this case) and the relevant effects can be detected in particular on the pericenter anomaly and eccentricity.

Regarding the solar perturbation, this one is modelled according to a model developed by Kozai [33], the procedure is similar to the one used to model J_2 perturbation in Chapter 4.1 with some differences: the long-periodic contributions are derived numerically whereas the short-periodic ones are computed analytically.

In order to decrease the computational cost and avoid numerical integration, some modifications to the original theory are made:

1. Since the CAMs' manoeuvring times last less than few hours, the long-periodic effects will not act in a relevant way in this amount of time and so it can be treated as part of the secular contribution;
2. Secular evolution of Keplerian elements is considered to vary linearly in time;

Taking into account these assumptions, a fully analytical model for Sun perturbation is derived, Algorithm 4.2 reports the main steps to compute the final state of a satellite subject only to the Sun perturbation, starting from a set of osculating Keplerian elements;

the full expressions of the secular and short-periodic contributions can be found in [33].

Algorithm 4.2 Sun Model Algorithm

```
Start from initial osculating element $\alpha_0$ and propagation time $\Delta$t.
Compute the mean elements $\overline{\alpha}_0$ from the initial Keplerian osculating elements solving the following non-linear system:
    $F(\overline{\alpha}_0) = \overline{\alpha}_0 + \Delta\overline{\alpha}_{sp,0} - \alpha_0 = 0 \quad (4.11)$
    where $\Delta\overline{\alpha}_{sp,0}$ is the short periodic contribution evaluated at the initial time.
Propagate the initial mean elements to the wanted time $\Delta$t by adding linearly the secular rates.
    $\overline{\alpha}(t) = \overline{\alpha}_0 + \dot{\alpha}_{sec}\Delta t \quad (4.12)$
Compute the short-periodic terms and add them to the propagated variables to retrieved the final osculating state in terms of Keplerian elements:
    $\alpha(t) = \overline{\alpha}(t) + \Delta\overline{\alpha}_{sp} \quad (4.13)$
```

The accuracy of the model was tested by calculating the maximum absolute error over one revolution between the numerical and analytical models for a given range of eccentricities and inclinations; the starting propagation time of the algorithm was fixed to 1^{st} March 2023 whereas Sun ephemerides were computed by adopting the same equations used for the SRP model (Eq. 4.9).

Figure 4.7 shows how the error increases exponentially as the orbit gets more and more circular reaching a maximum error of 150 meters for e=0.0001, the inclination instead does not have so much influence in the error of the model; also in this case the algorithm was run for different epochs of 2023 to check the error of the model over one year, Figure 4.8 reports this error for a generic GEO (e=0.0005, i=1 deg) showing an oscillatory behaviour (as seen in Figure 4.6) with a maximum error of 60 meters over the whole year.

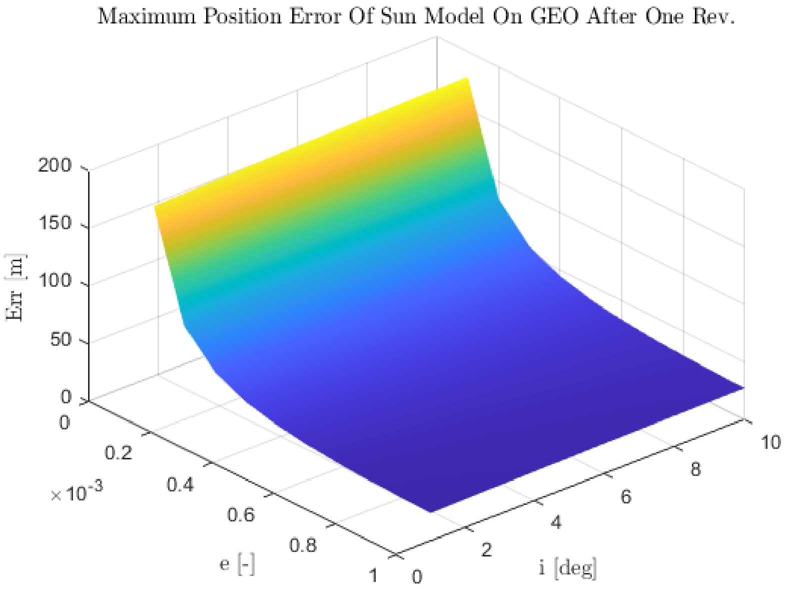

Figure 4.7: Error in position of Sun model.

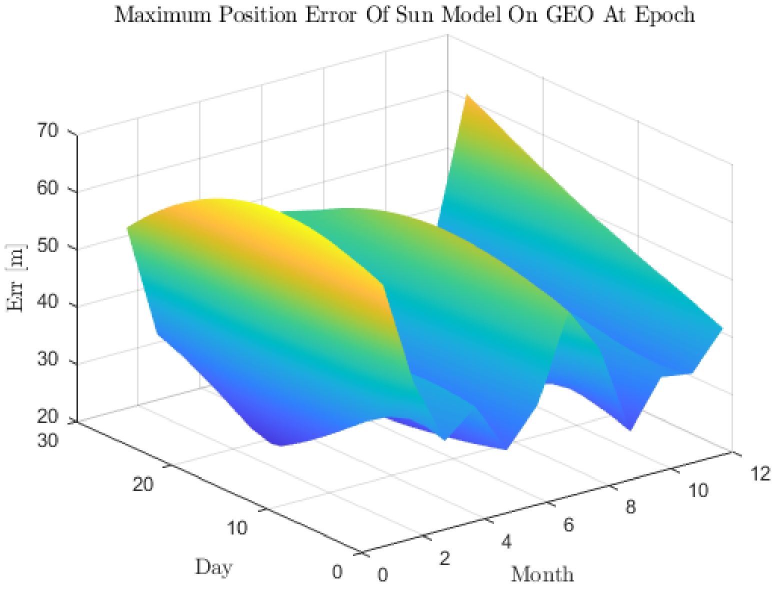

Figure 4.8: Error in position of Sun model at epoch.

4.5. Numerical Moon Perturbation Model

For what concerns the Moon perturbation on GEO, several models were considered to compute this perturbation such as the versions proposed by Giacaglia [19], Lane [34], Musen [37] and Kozai [33].

Numerical tests have been performed on Kozai's and Giacaglia's models, however the results are not accurate enough and the models are really heavy from a computational point of view (especially when solving the non-linear equations to get the mean elements) making them inefficient with respect to the full numerical integration.

For this purpose it was decided to model Moon perturbation by integrating numerically the Gaussian equations using *ode45* of *MATLAB* with more relaxed tolerances: *abstol* and *reltol* are both fixed to 1e-8.

4.6. Analytical In-Plane Low-Thrust Models

To model a low thrust CAM with perturbation is important to have a model for in-plane thrust of course; analytical models for both the tangential and normal thrust were already presented in Section 1.3.2 with their references.

In this section a sensitivity analysis for both the tangential and normal components will be performed in LEO and GEO to have a better understanding of the error between the two models.

4.6.1. Tangential LT Model

It is important to have a good accuracy along this component since the optimal thrust direction to get optimal results tends to align with the tangential one or close to it; the first order algorithm developed by Gonzalo et al. [23] was tested on LEO for different ranges of a and e considering a propagation time of five periods and a tangential thrust acceleration of 1e-9 km/s^2 (which is a reasonable value for a low thrust of 500 mN mounted on ISS with mass of 420 tons).

The maximum absolute error in position between the numerical and analytical models was computed and plotted in Fig. 4.9, the error tends to stay below 10 meters even after five revolution all over the LEO region, which is really good considering also the given thrust levels.

The algorithm was tested also on GEO for a given range of eccentricities and inclinations, in this case the thrust level is still fixed to 1e-9 km/s^2 but the propagation time is reduced to only one period since there is no interest for longer time when dealing with low-thrust

CAM, results are shown in Fig. 4.10 where the maximum absolute error in position is plotted; in this case the error is much higher than in LEO due to the fact that the tangential thrust parameter $\epsilon_t{=}a_t a_{ref}^2/\mu$ is no longer small in GEO so, when performing the series expansion, the error tends to grow up too, the error in particular is much higher for quasi-circular orbits: the lower the eccentricity the more sensitive the error in pericentre anomaly, so even a small error in ω can cause a large error in position when dealing with very low eccentric orbits; for what it concerns the inclination, the error tends to remain constant since the tangential model does not have any influence in the inclination of the orbit.

Another aspect to consider is that as ϵ_t increases, the displacement for a given acceleration increases too together with the error because the perturbation becomes stronger compared to the main gravitational attraction.

Fig. 4.11 shows the behaviour of the error as function of the total displacement obtained by solving for different ϵ_t; in particular it shows how the error increase exponentially with the displacement both on LEO and GEO, considering tangential accelerations that go from 1e-9 to 5e-9 km/s^2.

Although the same accelerations are adopted, the error in LEO is much lower than in GEO since in LEO a_{ref} is smaller.

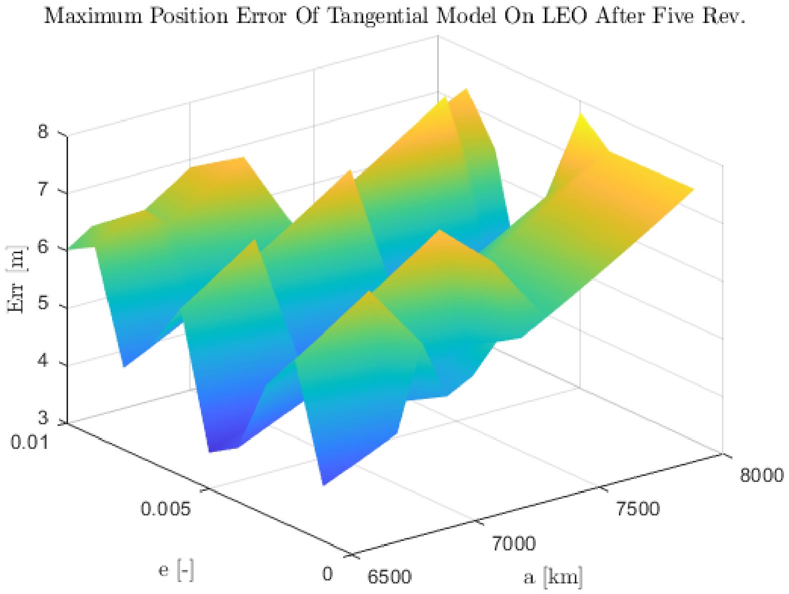

Figure 4.9: Error in position of LEO tangential model.

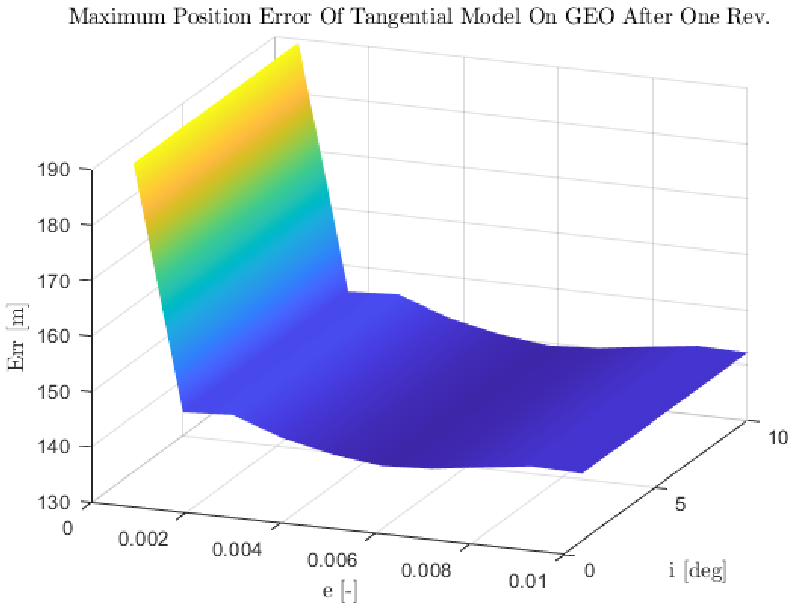

Figure 4.10: Error in position of GEO tangential model.

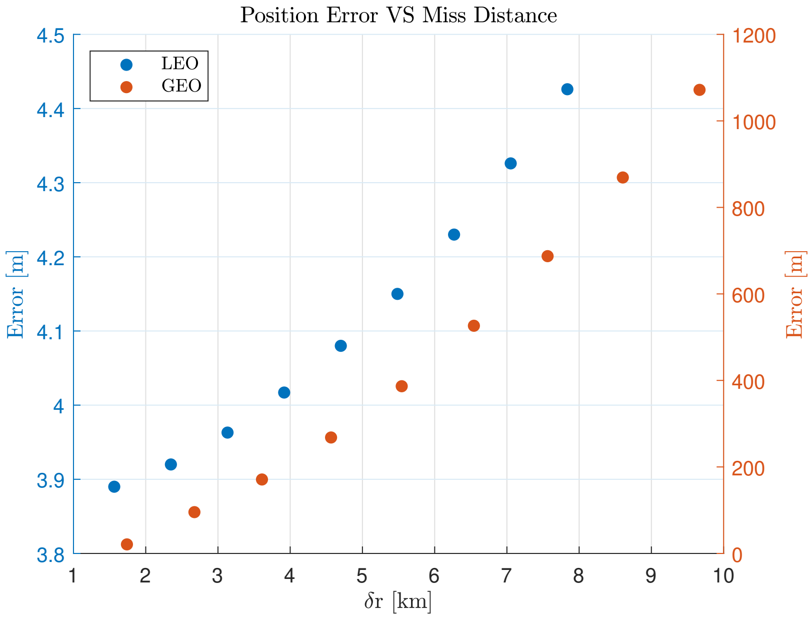

Figure 4.11: Position error VS displacement obtained from different ϵ_t.

4.6.2. Normal LT Model

To have an overall model for in-plane thrust, also a normal thrust model was developed, although the normal component is not essential as the tangential one when dealing with LT CAM; in this case analytical expression for e, ω and E are formulated to develop lightweight algorithms.

To assess the accuracy of the model developed by Gonzalo et al. for the normal component [25], the algorithm was run first on LEO considering a propagation time of five periods and a normal thrust acceleration of -1e-9 km/s^2; the error of the model between the analytical and numerical one is shown in Fig. 4.12.

In this case the error is much larger than that already presented for the LEO tangential case reaching peaks of 40 meters for high semi-major axes but it is still a good error especially considering the high thrust level used for the test: the thrust level along the normal component is much lower than that along the tangential one which is the optimal direction.

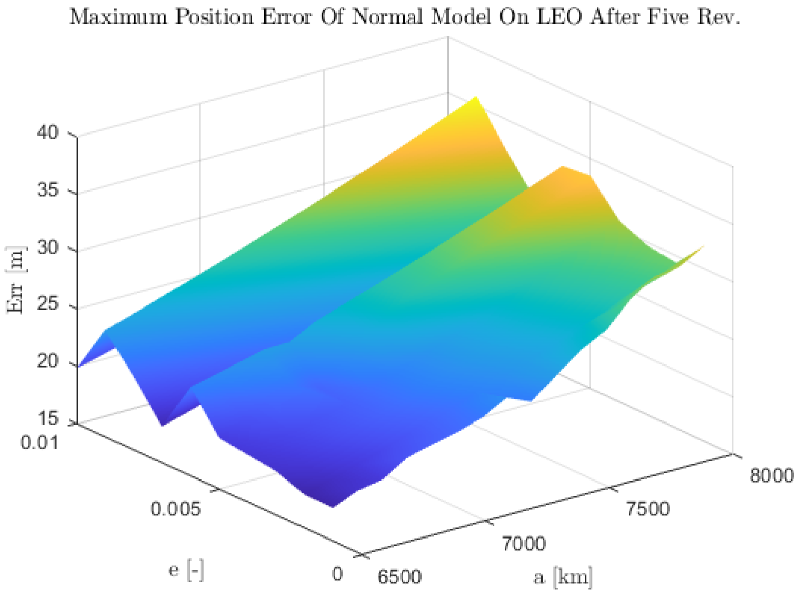

Figure 4.12: Error in position of LEO normal model.

The algorithm was tested also in GEO considering for this case a propagation time of one period and a normal thrust acceleration of -1e-10 km/s^2, the error was plotted for different ranges of inclinations and eccentricities as shown in Fig. 4.13; as it can be noticed, the error is much bigger than the GEO tangential case reaching errors in the order of kilometers for the quasi-circular orbits, for this reason the normal component is not considered for orbits with $e<0.0005$ whereas for e>0.0005 a limited normal thrust acceleration of -1e-10 km/s^2 is considered.

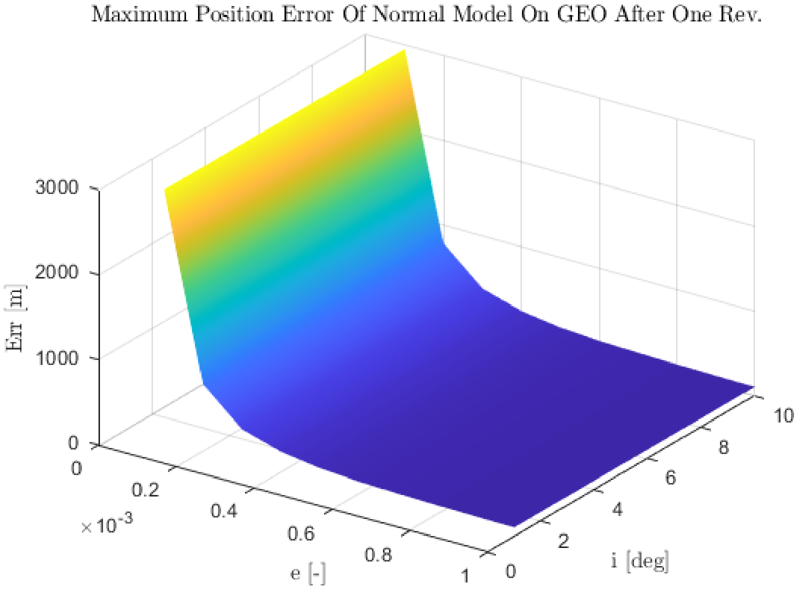

Figure 4.13: Error in position of GEO normal model.

Lastly, from now on, to have a better understanding of the LT propulsion, the two components will be expressed through a^T and γ_t which are the acceleration magnitude and the angle measured clockwise from the tangential direction respectively, in this way it is straightforward to calculate the two components as:

$$\begin{cases} a_t = a^T \cos\gamma_t \\ a_n = -a^T \sin\gamma_t \end{cases} \tag{4.14}$$

For LEO the considered angle γ_t goes from 0 to 30 degrees whereas on GEO from 0 to 5 degrees, this narrow range is also related to the model accuracy since high accelerations on the normal direction cause big errors on GEO; instead, the considered acceleration magnitude a^T goes from $1{\times}10^{-9}$ to $5{\times}10^{-9}$ km/s^2 for both regions.

4.7. Computation of Perturbed Elements

Table 4.1 shows the main perturbation models that have been treated until now with their classification; almost all of them consist of analytical and SA algorithms that are capable of computing the final state in a shorter time with respect to a numerical model; the only exception is given by Moon perturbation which is the only fully numerical model, since it was not possible to retrieve a fast and accurate algorithm to compute the final states.

	LEO	**GEO**
Drag	SA	-
Sun	-	AN
SRP	-	AN
J$_2$	AN	AN
Moon	-	NUM
LT$_n$	AN	AN
LT$_t$	AN	AN

Table 4.1: Summary of perturbation models.

Now that all of the perturbation models have been shown, the next step is to compute the final Keplerian element at a given time starting from an initial one given at t_0; this is computed by adding to the initial element α_0 the variation caused by each perturbation to the given element α.

The variations for a given perturbation are calculated as follows by considering one perturbation per time:

$$\begin{cases} \delta a_{pert}(t) = a_{pert}(t) - a_0 \\ \delta e_{pert}(t) = e_{pert}(t) - e_0 \\ \delta i_{pert}(t) = i_{pert}(t) - i_0 \\ \delta \omega_{pert}(t) = \omega_{pert}(t) - \omega_0 \\ \delta \Omega_{pert}(t) = \Omega_{pert}(t) - \Omega_0 \\ \delta M_{pert}(t) = M_{pert}(t) - M_0 - \sqrt{\frac{\mu}{a_0^3}}(t - t_0) \end{cases} \tag{4.15}$$

Once the variations are calculated for all of the perturbations, the final Keplerian elements are retrieved using Eq. (4.16) for the LEO case where only drag and J$_2$ perturbation are considered together with the LT action and Eq. (4.17) for the GEO case where instead luni-solar, SRP and J_2 are considered together with the LT action.

In LEO this formula approximates well the perturbed behaviour of KE for any eccentricities and semi-major axes, but on GEO the formula shows some inaccuracies especially for very low eccentricities.

To avoid big errors in the perturbed GEO model a limitation on the eccentricity was set to 0.0005, any e lower than this limit will create big errors in the model.

$$\alpha(t)^{LEO} = \alpha_0 + \delta\alpha_{drag}(t) + \delta\alpha_{J2}(t) + \delta\alpha_t(t) + \delta\alpha_n(t) \tag{4.16}$$

$$\alpha(t)^{GEO} = \alpha_0 + \delta\alpha_{Moon}(t) + \delta\alpha_{J2}(t) + \delta\alpha_{Sun}(t) + \delta\alpha_{srp}(t) + \delta\alpha_t(t) + \delta\alpha_n(t) \tag{4.17}$$

The accuracy and advantages of this propagator will be shown in Chapter 5 which is dedicated to the design of perturbed CAM and the use of the developed SA propagator for different optimisation problems.

5 | CAM Design

5.1. Introduction to SA Propagator

The perturbed SA propagator built until now computes the KE at the original CA, in particular the propagator takes as input the original state of satellite and debris at CA, the powered time (or manoeuvring time, Δt_{CAM}) where LT is turned on, the coasting time (Δt_{coast}) where LT is turned off and the thrust acceleration a^T, giving as output the final state of the satellite at the original time of CA after being perturbed by the given thrust acceleration for the given time Δt_{CAM} under the influence of orbital perturbations. The steps of the SA propagator can be summarized with the following three points, reported below and in Fig 5.1:

1. **Backward Arc**: Backward perturbed propagation for a time $\Delta t{=}\Delta t_{CAM}{+}\Delta t_{coast}$, starting from the initial state at CA considering a null LT action;
2. **Powered Arc**: Forward perturbed propagation for a time Δt_{CAM}, starting from the final state obtained from the backward propagation in step 1, considering also the LT action (which was given as input);
3. **Coasting Arc**: Forward perturbed propagation for a time Δt_{coast}, starting from the final state obtained from the powered phase in step 2, considering a null LT action;

All of these steps take into account the orbital perturbations during the propagation, which are based on the SA and AN algorithms developed in Chapter 4 and combined through Eq. (4.16) for the LEO case and Eq. (4.17) for the GEO case.

Now that the final state is derived from the coasting arc, the next step is the computation of miss distance and PoC.

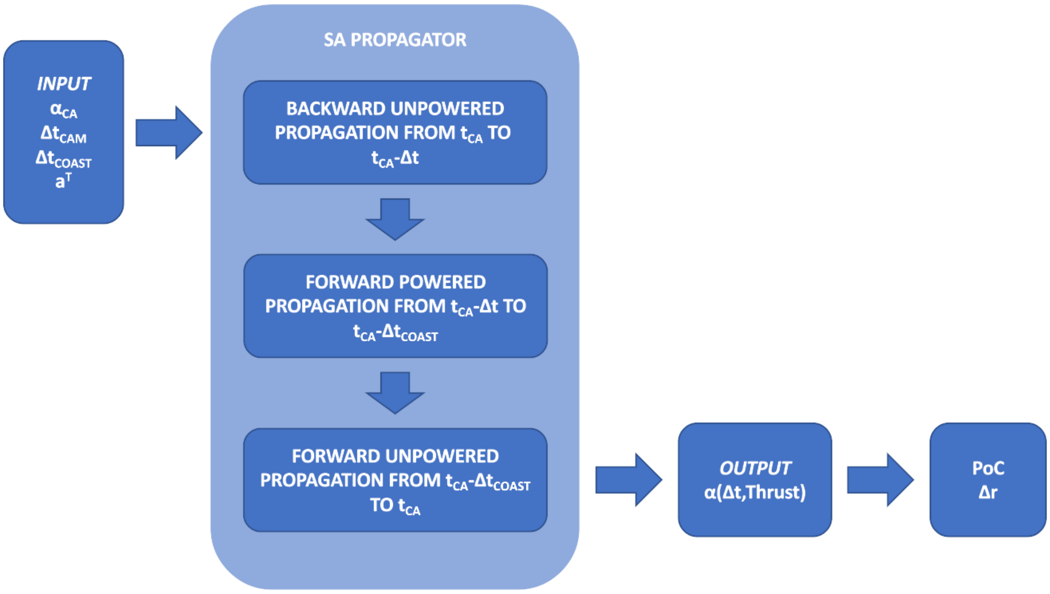
INPUT
αCA
ΔtCAM
ΔtCOAST
aT
SA PROPAGATOR
BACKWARD UNPOWERED PROPAGATION FROM tCA TO tCA-Δt
FORWARD POWERED PROPAGATION FROM tCA-Δt TO tCA-ΔtCOAST
FORWARD UNPOWERED PROPAGATION FROM tCA-ΔtCOAST TO tCA
OUTPUT
α(Δt,Thrust)
PoC
Δr

Figure 5.1: Structure of the perturbed SA propagator.

5.1.1. Computation of Miss Distance

Given the state at CA and the final state in terms of KE obtained from the propagator, the miss distance can be retrieved immediately:

1. Convert the two states based in KE to Cartesian elements to retrieve the position vector for both;
2. Compute the difference $\vec{\delta r}$ between the two position vectors;
3. Compute the miss distance δr by taking the norm of the vector computed in 2;

5.1.2. Computation of PoC

The computation of the PoC is not that immediate, as shown in Chapter 3 there are different methods to compute it, but in this work it was decided to adopt Chan's method for its computation.

Once the combined covariance matrix, projected in the B-plane, $\mathbf{C}_{\xi\zeta}$ and the combined radius s_a have been defined, the PoC is computed through the following steps:

1. Convert the two states based in KE to Cartesian element to retrieve the position vector for both;
2. Compute the difference $\vec{\delta r}$ between the two position vectors;

3. Through a rotation matrix, transform the vector $\vec{\delta r}$ from the Cartesian reference frame to the B-plane reference frame which axes are computed through Eq. (1.1) (in this case $\vec{v}_1$ and $\vec{v}_2$ are the velocity of s/c and debris at CA respectively);
4. Use the components of the B-plane position vector to compute the covariance ellipse ratio u and the depth of intrusion v through Eq. (3.7) and (3.8);
5. Calculate the PoC using Chan's formula given in Eq. (3.6) truncated after three-four terms;

5.2. Introduction to Optimisation Problems

Now that all the algorithms and elements to compute miss distance and PoC have been presented, the next goal is to use these algorithms to design and validate real case CAM through optimisation analysis, which is carried out through a parametric analysis involving three main free variables: a^T, Δt_{CAM}, Δt_{coast}.
With the developed propagator it is possible to solve several optimisation problems:

- Minimisation of cost to reach given miss distance or PoC;
- Minimisation of time to reach given miss distance or PoC;
- Maximisation of miss distance in a given interval;
- Minimisation of PoC in a given time;
- Other combinations involving PoC, δr, Δv and Δt;

Some of these problems will be discussed and solved in the next sections through numerical examples, both for LEO and GEO, highlighting the differences between the fully numerical and SA approaches.

5.3. Case A : Cost Minimization for Given Miss Distance

The goal of this optimisation problem consists in reaching a given miss distance $\overline{\delta r}$ by minimizing the Δv parameter, which is computed as a product between the thrust acceleration a^T and the manoeuvring time Δt_{CAM}; in order to have a bounded problem, a further constraint on the overall time Δt is applied which takes into account the times needed for the design of CAM,and various processes that start once CA is detected.
This kind of problem can be mainly implemented to save propellant.

5.3.1. Case A : Optimisation on LEO

Problem Statement

In this test case, a CA is detected on 27^{th} June 2023 at 3:37 p.m. (GMT), the states of both orbit and debris are reported in Table 5.1 and the goal is to reach a miss distance of about 800 meters (or more), by minimizing the cost of the CAM, moreover the overall manoeuvre cannot last more than 3.5 periods of the nominal orbit.

	a [km]	e [-]	i [deg]	ω [deg]	Ω [deg]	θ [deg]	$\frac{A}{m}$ $[\frac{m^2}{kg}]$	C_D [-]
LEO$_1$	7500	.0070	40.00	10.00	20.00	100.00	0.100	2.0
DEB	7549	.0701	39.14	17.56	23.54	89.71	-	-

Table 5.1: Case A: Orbital parameters of LEO$_1$ and debris at CA.

To better define the problem, a mathematical formulation is reported in Eq. 5.1:

$$\begin{cases} \min \Delta v = \min a^T \Delta t_{CAM} \\ \delta r \geq 800 \text{ m} \\ \Delta t \leq 3.5 \text{ T} \end{cases} \tag{5.1}$$

Optimisation Analysis

The problem has four free variables to work on in order to carry out the optimal solution: a^T, Δt_{CAM}, Δt_{coast} and γ_t; in order to decrease the dimension of the problem, it was decided to use a constant parameter for the angle γ_t which was fixed to 15 degrees, so from now the miss distance δr is function of only three variables.

The optimal solution is carried out by performing a parametric analysis in Δt_{CAM} and Δt_{coast} for a given acceleration level a^T, at this point once the contour plots with the curves' level in δr are obtained, an optimisation analysis on each of these plots is performed in order to get a sub-optimal solution for each value of a^T, lastly all of these sub-optimal solutions are confronted to get a final global optimal solution.

The parametric analysis uses different values of Δt_{CAM} and Δt_{coast} which go from 0 to 3.5 T in 50 equally spaced steps, whereas for the accelerations five values are considered which go from 1e-9 to 5e-9 km/s^2, so a final 50x50x5 grid is obtained and solved.

The next five figures (Fig. 5.2, 5.3, 5.4, 5.5 and 5.6) show the various contour plots (with the δr curves' level in meters) obtained for the different values of a^T, in particular in each of them is presented the solution obtained by solving the grid analytically through the SA propagator (on the left) and the absolute error in δr (on the right) between the SA and numerical models, this one is carried out through *ode45* of MATLAB with *abstol* and *reltol* of 1e-13, in the analytical plot is also present a red dot which identify the sub-optimal solution for the given ϵ.

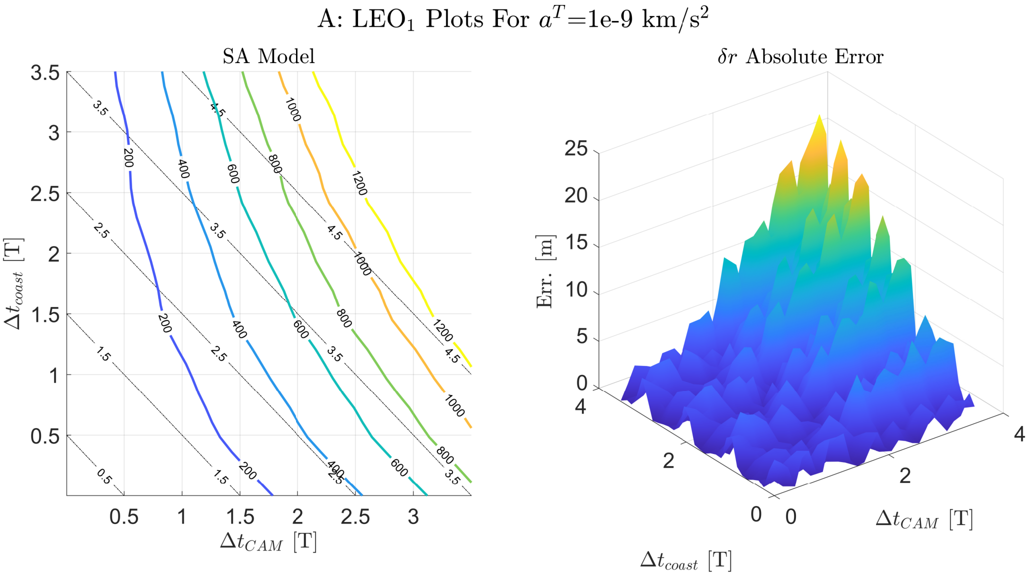

Figure 5.2: CASE A: LEO$_1$ solution for a^T=1×10^{-9} km/s^2.

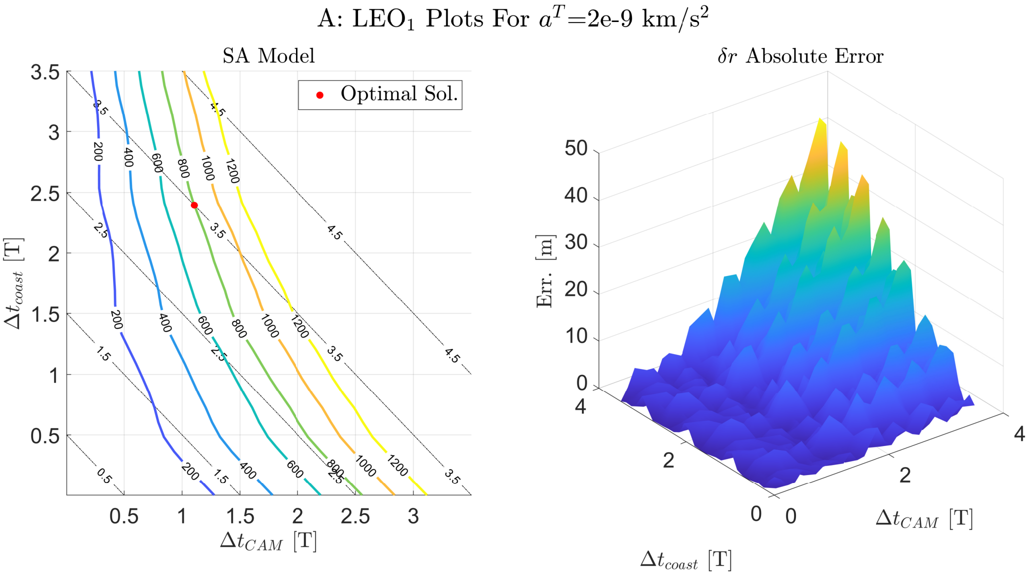

Figure 5.3: CASE A: LEO$_1$ solution for a^T=2×10^{-9} km/s^2.

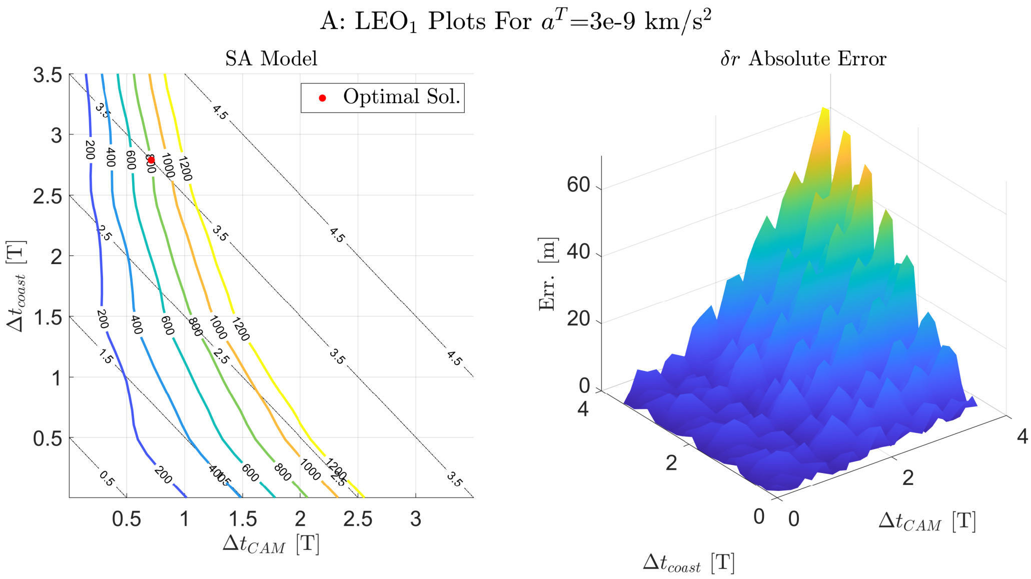

Figure 5.4: CASE A: LEO$_1$ solution for a^T=3×10^{-9} km/s^2.

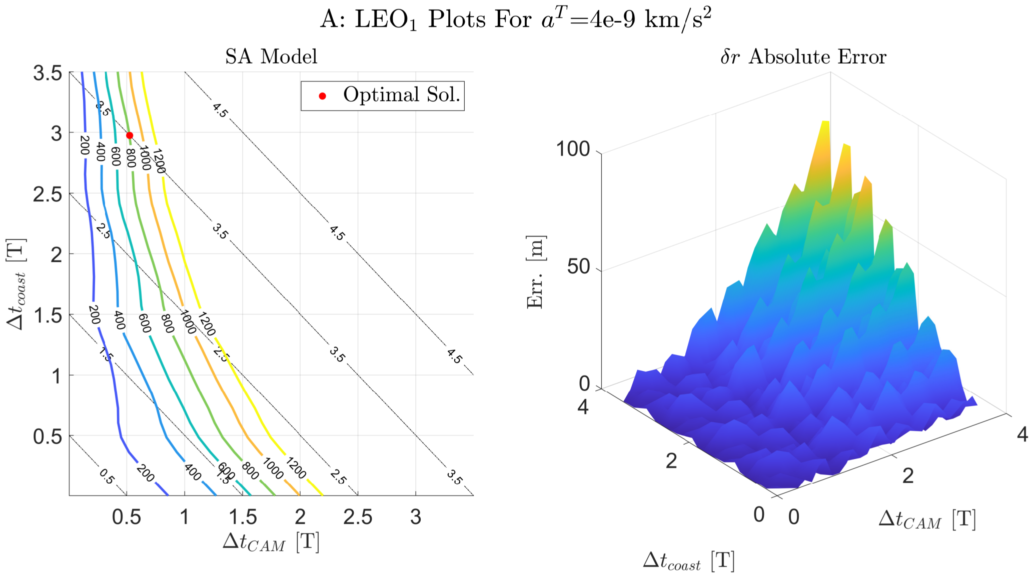

Figure 5.5: CASE A: LEO$_1$ solution for a^T=4×10^{-9} km/s^2.

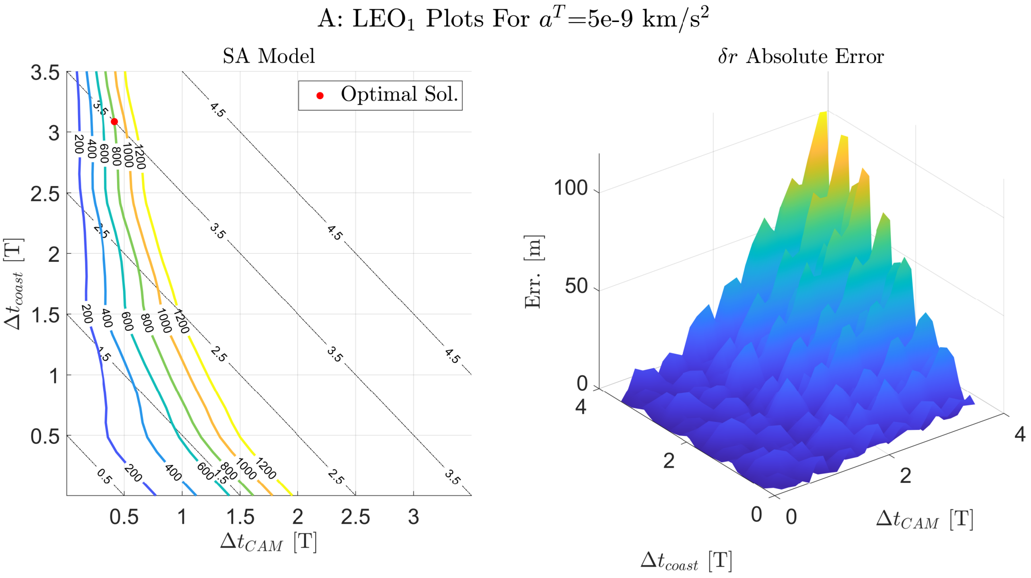

Figure 5.6: CASE A: LEO solution for a^T=5×10^{-9} km/s^2.

Fig. 5.2 shows no feasible solution with respect to the others since the acceleration is not enough to grant a miss distance of 800 meters before 3.5 T, it can be notice too that the optimal solution tends to move along the curve line of 3.5 T towards lower and lower manoeuvring times as the acceleration level increases.

Solution Analysis

Table 5.2 reports the coordinates of the sub-optimal solution for each acceleration with their relative miss distances and costs, moreover the last two columns report the CPU cost of the SA and numerical methods to solve the 50x50 grid.

It is easy to notice that the global optimal solution which gives the minimum cost Δv is the one obtained by using an acceleration of 5e-9 km/s^2.

a^T [$\frac{km}{s^2}$]	δr [m]	Δt_{CAM} [T]	Δt_{coast} [T]	Δt [T]	Δv [$\frac{cm}{s}$]	t_{CPU}^{an} [s]	t_{CPU}^{num} [s]
1e-9	-	-	-	-	-	42.17	946.82
2e-9	$\approx$ 800	1.1060	2.3940	3.5000	1.4298	38.63	986.67
3e-9	$\approx$ 800	0.7124	2.7876	3.5000	1.3815	37.20	1040.88
4e-9	$\approx$ 800	0.5259	2.9740	3.5000	1.3598	37.22	978.07
5e-9	$\approx$ 800	0.4158	3.0842	3.5000	1.3439	37.70	1001.22

Table 5.2: Case A: LEO$_1$ results for different a^T.

Now that the problem is solved, the final solution can be summarized as follows:

- The CAM starts on **June 27th 2023** at **9:20 a.m.(GMT)**;
- An acceleration of **5e-9 km/s^2** tilted of **15 deg** from the tangential direction is adopted;
- The powered leg lasts approximately **45 min** (2688 s);
- The coasting leg lasts **5 h 32 min** (19936 s);
- The total time of the manoeuvre (powered+coasting) is about **6 h 17 min**;
- The cost of the manoeuvre is **1.3439 cm/s**;
- The final miss distance, reached through the manoeuvre, is about **800 m**;
- To solve the 50x50x5 grid and compute the solution the **SA** propagator takes **192.92 s** whereas the **numerical** takes **4953.66 s**;

The last point describes the fulcrum of the whole thesis: saving time is essential when dealing with this kind of manoeuvres especially when collisions are detected at the latest moment and the manoeuvre has to be designed in a short time; the use of these lightweight algorithms help in the design process by reducing drastically the computational cost of also two orders of magnitude with respect to a numerical integration and giving also accurate results as shown in Table 5.3 where the values of the optimal solution obtained from the SA model are confronted with those from the numerical one: the error committed in time during the powered and coasting legs are both of only **25 s**, whereas the error on Δv is about **0.0136 cm/s**.

	δr **[m]**	Δt_{CAM} **[T]**	Δt_{coast} **[T]**	Δv **[$\frac{cm}{s}$]**	t_{CPU} **[s]**
SA	≈ 800	0.4158	3.0842	1.3439	37.70
NUM	≈ 800	0.4116	3.0884	1.3303	1001.22

Table 5.3: Case A: LEO$_1$ results from numerical and SA models for a^T=5e-9 km/s^2.

5.3.2. Case A : Optimisation on GEO

Problem Statement

In this test case, a CA is detected on 1st April 2023 at 9:49 p.m. (GMT), the states of both the GEO and debris are reported in Table 5.4 and the goal is to reach a miss distance of about 1100 meters (or more), by minimizing the cost of the CAM, moreover the overall manoeuvre cannot last more than 0.3 periods of the nominal GEO.

	a [km]	e [-]	i [deg]	ω [deg]	Ω [deg]	θ [deg]	$\frac{A}{m}$ [$\frac{m^2}{kg}$]	C_R [-]
GEO$_1$	42165	.0008	1.00	50.00	30.00	20.00	0.010	1.2
DEB	38846	.3128	35.16	124.17	98.66	237.47	-	-

Table 5.4: Case A: Orbital parameters of GEO$_1$ and debris at CA.

The mathematical formulation of the problem is reported in Eq. 5.2:

$$\begin{cases} \min \Delta v = \min a^T \Delta t_{CAM} \\ \delta r \geq 1100 \text{ m} \\ \Delta t \leq 0.3 \text{ T} \end{cases} \tag{5.2}$$

Optimisation Analysis

For this problem, it was decided to use a fixed value of three degrees for the angle γ_t. Also in this case, the optimal solution is carried out by performing a parametric analysis in Δt_{CAM} and Δt_{coast} for a given acceleration level a^T.

The parametric analysis uses values of Δt_{CAM} and Δt_{coast} which space from 0 to 0.3 T in 50 equally spaced steps, whereas for the accelerations the same range of values adopted in LEO are used, so a final 50x50x5 grid is obtained and solved; the next five figures (Fig. 5.7, 5.8, 5.9, 5.10 and 5.11) show the various contour plots obtained for the different values of a^T, with the same structure as before: analytical solution on the left, the absolute error on the right and a red dot to identify the sub-optimal solution in the analytical model.

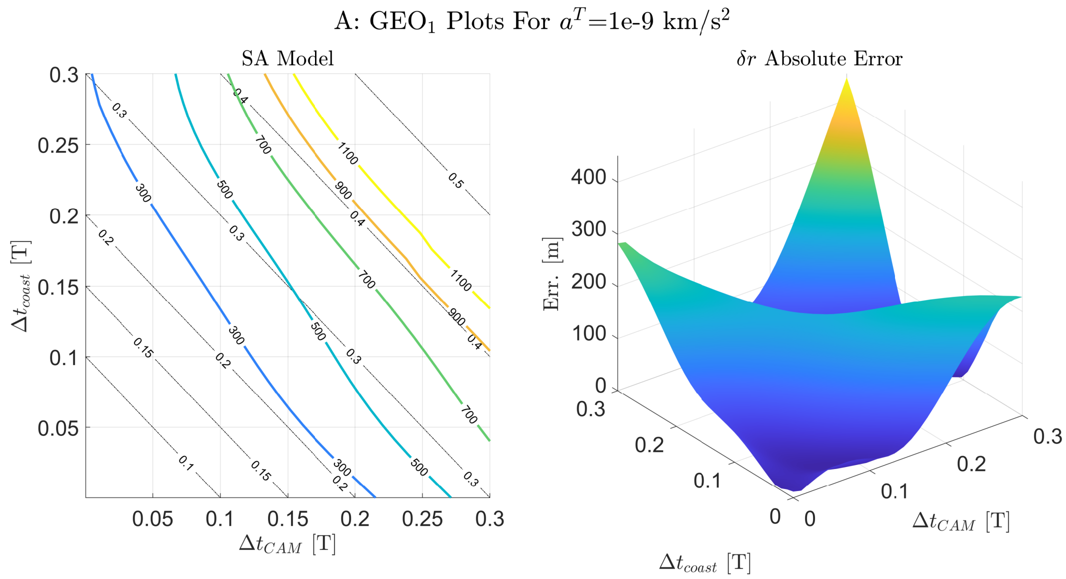

Figure 5.7: CASE A: GEO$_1$ solution for a^T=1$\times$10^{-9} km/s^2.

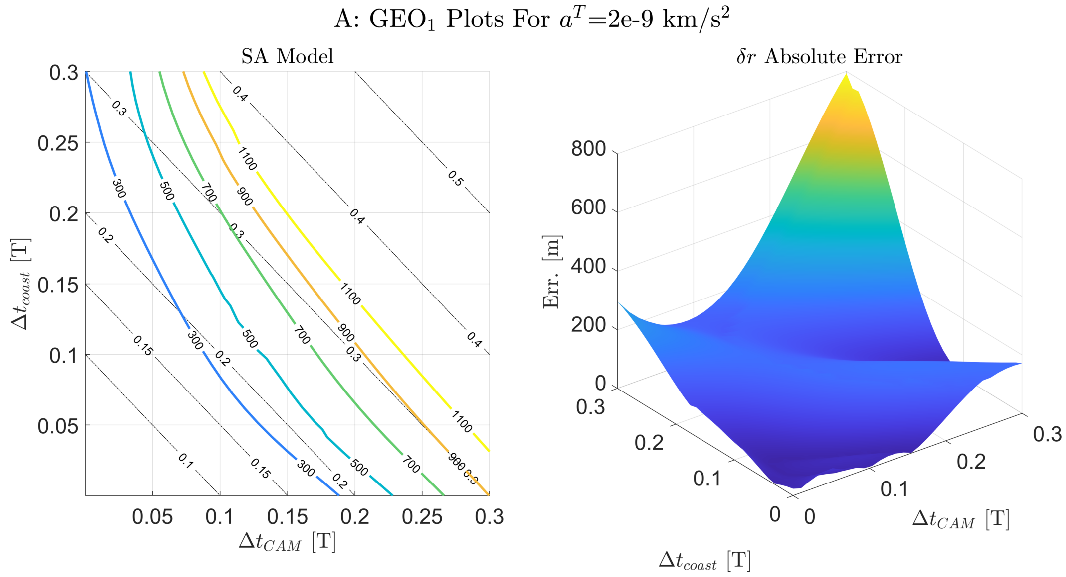

Figure 5.8: CASE A: GEO$_1$ solution for a^T=2$\times$10^{-9} km/s^2.

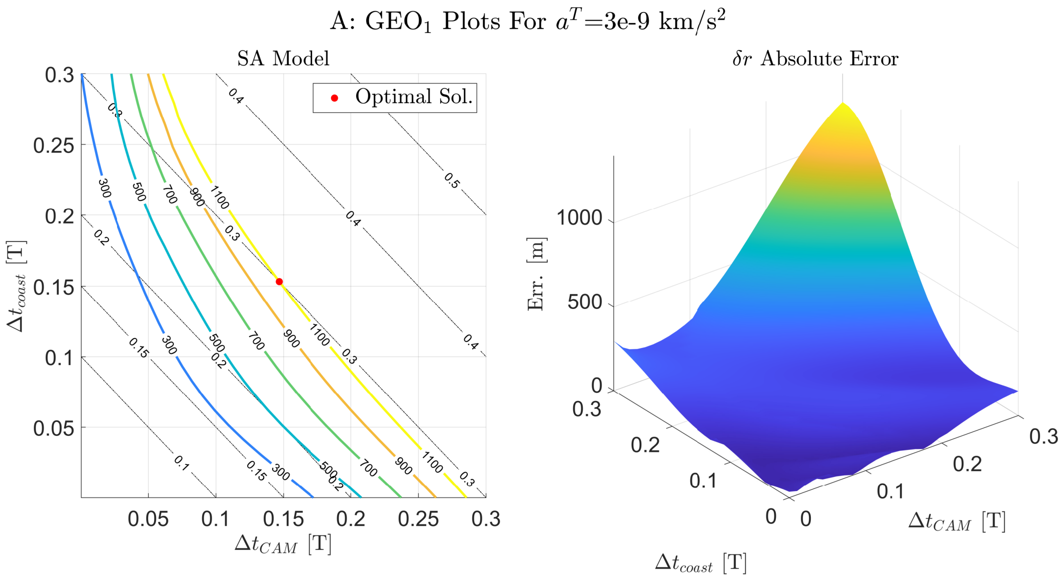
A: GEO_1 Plots For a^T=3e-9 km/s^2

Figure 5.9: CASE A: GEO_1 solution for a^T=3×10^{-9} km/s^2.

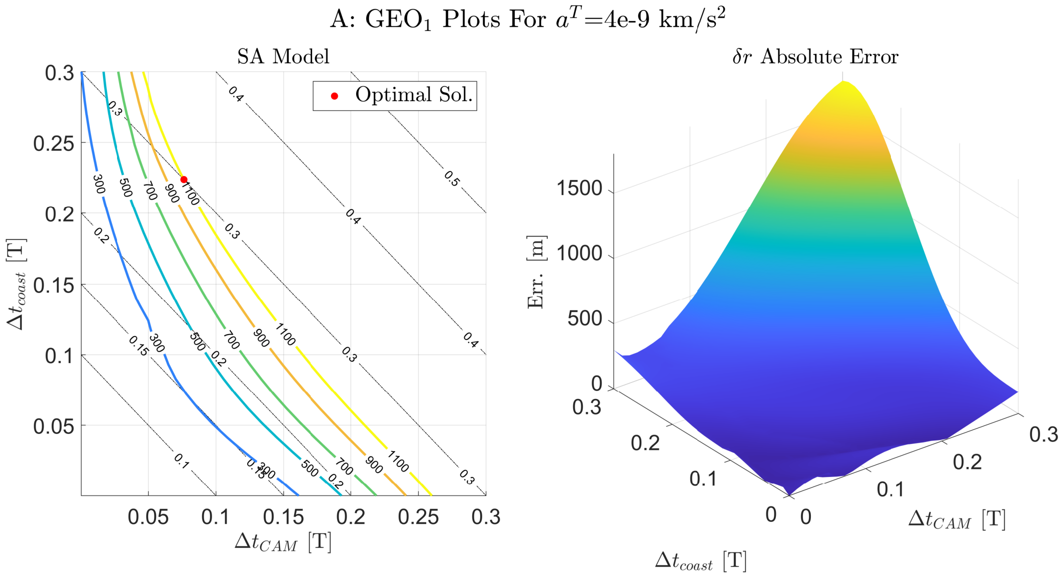
A: GEO_1 Plots For a^T=4e-9 km/s^2

Figure 5.10: CASE A: GEO_1 solution for a^T=4×10^{-9} km/s^2.

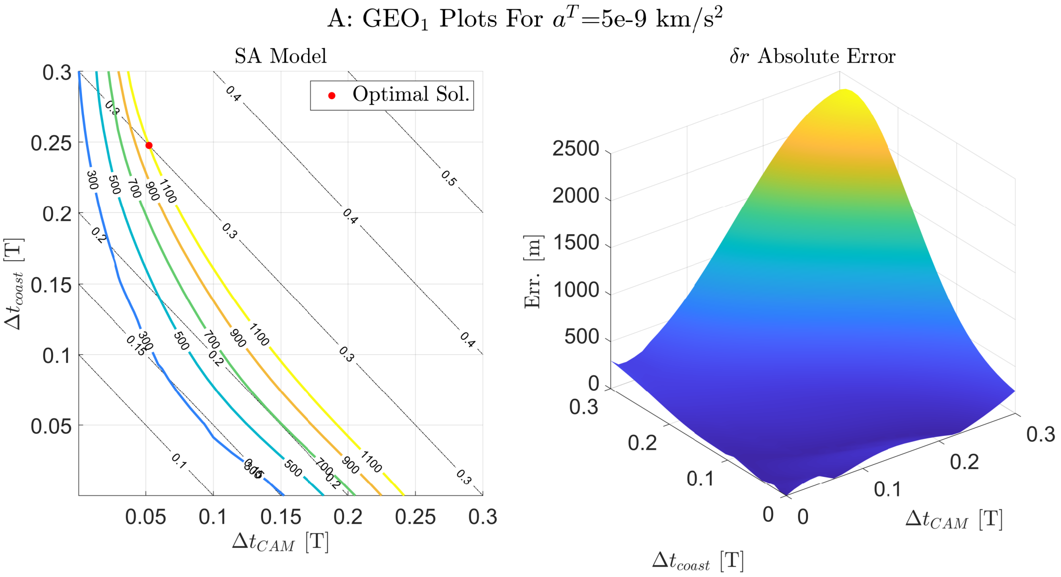

Figure 5.11: CASE A: GEO$_1$ solution for a^T=5×10^{-9} km/s^2.

Fig. 5.7 and 5.8 show no feasible solution with respect to the others, since the acceleration levels are not enough to grant a miss distance of 1100 meters before 0.3 T; instead the optimal solution in Fig. 5.9, 5.10 and 5.11 tends to move along the curve line of 0.3 T towards lower and lower manoeuvring times as the acceleration level increases.

Solution Analysis

Table 5.5 reports the various information in terms of cost and coordinates of the sub-optimal solution for each acceleration; the global optimal solution which gives the minimum cost Δv is the one obtained by using an acceleration of 5e-9 km/s^2.

a^T $[\frac{km}{s^2}]$	δr [m]	Δt_{CAM} [T]	Δt_{coast} [T]	Δt [T]	Δv $[\frac{cm}{s}]$	t_{CPU}^{an} [s]	t_{CPU}^{num} [s]
1e-9	-	-	-	-	-	53.23	92.21
2e-9	-	-	-	-	-	51.70	89.44
3e-9	$\approx$ 1100	0.1468	0.1532	0.3000	3.7948	51.33	89.30
4e-9	$\approx$ 1100	0.0763	0.2238	0.3000	2.6305	51.76	89.60
5e-9	$\approx$ 1100	0.0524	0.2476	0.3000	2.2590	50.71	90.72

Table 5.5: Case A: GEO$_1$ results for different a^T.

Once the final solution is carried out, the final solution can be summarized as follows:

- The CAM starts on **April 1st 2023** at **2:39 p.m.(GMT)**;
- An acceleration of **5e-9 km/s^2** tilted of **3 deg** from the tangential direction is adopted;
- The powered leg lasts approximately **1h 15 min** (4518 s);
- The coasting leg lasts **5 h 56 min** (21360 s);
- The total time of the manoeuvre (powered+coasting) is about **7 h 11 min**;
- The cost of the manoeuvre is **2.2589 cm/s**;
- The final miss distance, reached through the manoeuvre, is about **1100 m**;
- To solve the 50x50x5 grid and compute the solution the **SA** propagator takes **258.73 s** whereas the **numerical** takes **451.27 s**;

In this GEO case, despite the SA approach is still the fastest one, the difference in computational time between the two models is not as relevant as in LEO also by adopting very stringent tolerances for the numerical integrator.

The accuracy of the model is also tested by confronting the optimal solutions obtained from the SA and numerical models, the values reported in Table 5.6 shows that the committed error reaches values of about **30 min** for both the CAM and coasting arcs whereas in terms of cost, an error of **0.994 cm/s** is committed, these errors are mainly associated to the analytical thrust model, as the thrust level increases the error increases too especially on GEO (see Section 4.6.1).

	δr **[m]**	Δt_{CAM} **[T]**	Δt_{coast} **[T]**	Δv **[$\frac{cm}{s}$]**	t_{CPU} **[s]**
SA	$\approx$ 1100	0.0524	0.2476	2.2590	50.71
NUM	$\approx$ 1100	0.0755	0.2245	3.2530	90.72

Table 5.6: Case A: GEO$_1$ results from numerical and SA models for a^T=5e-9 km/s^2.

5.4. Case B : Time Minimization for Given Miss Distance

The goal of this problem is to reach a determined miss distance $\overline{\delta r}$ in the less amount of time Δt, given by the sum of the powered and coasting times; to have a bounded solution, the problem is also subject to a constraint in Δv given by the LT propulsion capability.

This kind of problem can be implemented for the last moment detection of CA or to complete the overall manoeuvre in a short time.

5.4.1. Case B : Optimisation on LEO

Problem Statement

In test case B, a CA is detected on June 23^{rd} 2023 at 7:05 a.m. (GMT), with the states of both satellite and debris reported in Table 5.7; the goal is to reach a miss distance of 800 meters by minimizing the overall time Δt, moreover the cost of the manoeuvre Δv must be kept less than 5.00 cm/s.

	a **[km]**	e **[-]**	i **[deg]**	ω **[deg]**	Ω **[deg]**	θ **[deg]**	$\frac{A}{m}$ **[**$\frac{m^2}{kg}$**]**	C_D **[-]**
ISS	6800	.0013	52.00	0.00	20.00	60.00	0.001	2.0
DEB	6762	.0088	52.07	295.21	20.16	124.69	-	-

Table 5.7: Case B: Orbital parameters of ISS and debris at CA.

The optimisation problem is lastly summarized in the following mathematical notation:

$$\begin{cases} \min \Delta t = \min\left(\Delta t_{CAM} + \Delta t_{coast}\right) \\ \delta r \geq 800 \text{ m} \\ \Delta v \leq 5.00 \text{ cm/s} \end{cases} \tag{5.3}$$

Optimisation Analysis

In this case it was decided to adopted a value of five degrees for γ_t.
For Δt_{CAM} and Δt_{coast} the values that are adopted, go from 0 to five orbital periods in 50 equi-spaced steps, whereas the same acceleration levels as before are adopted.
The results of each parametric analysis are shown in Fig 5.12, 5.13, 5.14, 5.15 and 5.16.

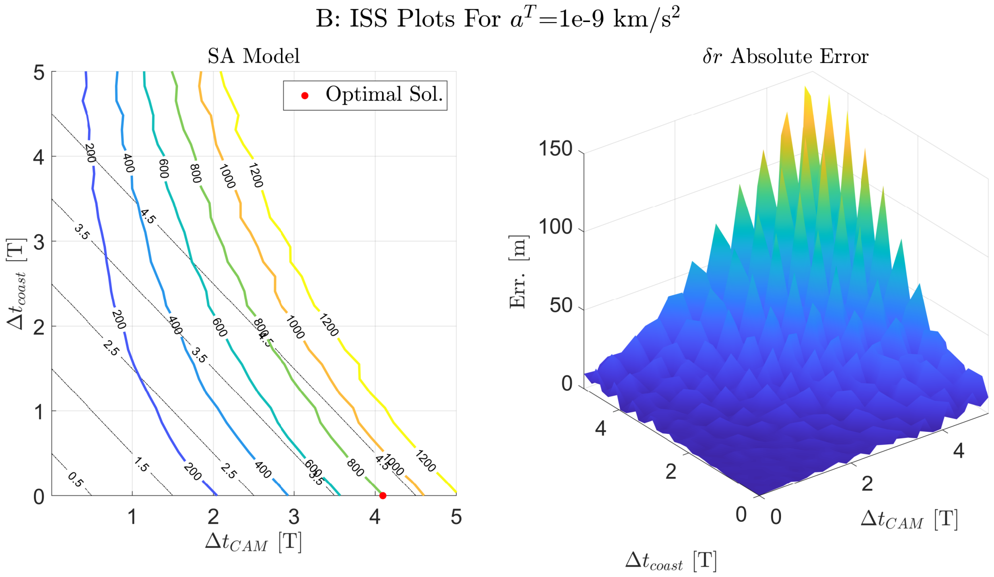

Figure 5.12: CASE B: ISS solution for a^T=1×10^{-9} km/s^2.

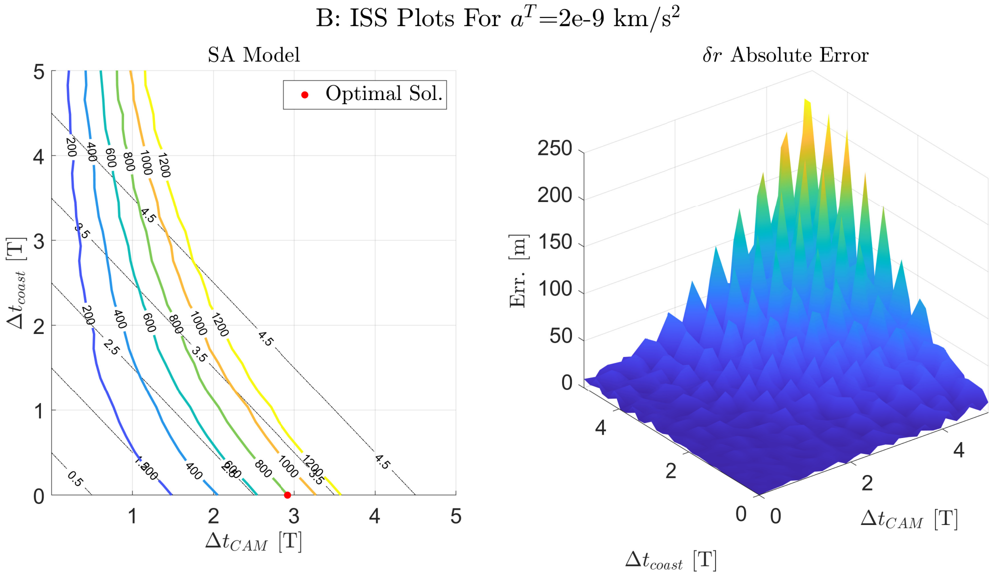

Figure 5.13: CASE B: ISS solution for a^T=2×10^{-9} km/s^2.

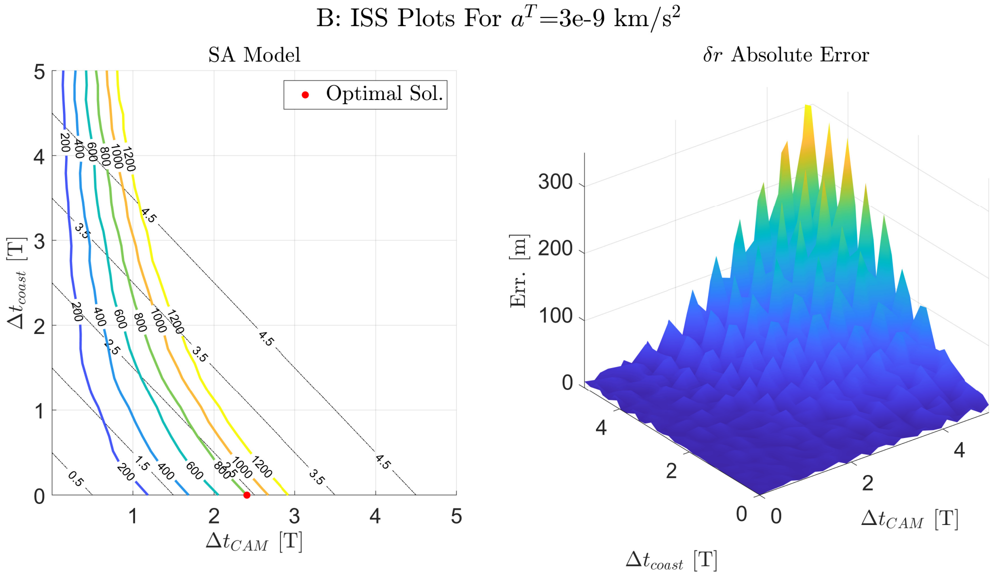

Figure 5.14: CASE B: ISS solution for a^T=3×10^{-9} km/s^2.

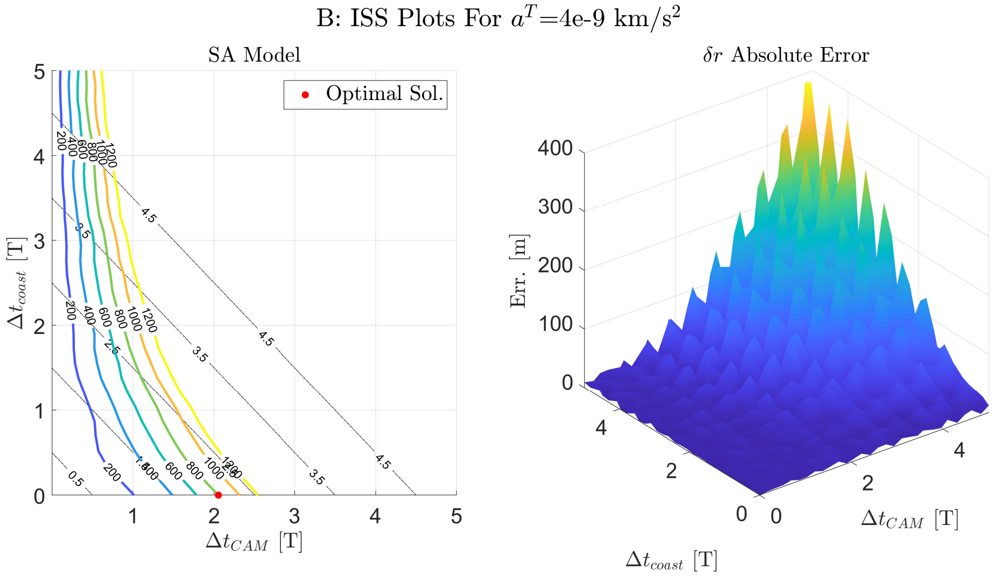

Figure 5.15: CASE B: ISS solution for a^T=4×10^{-9} km/s^2.

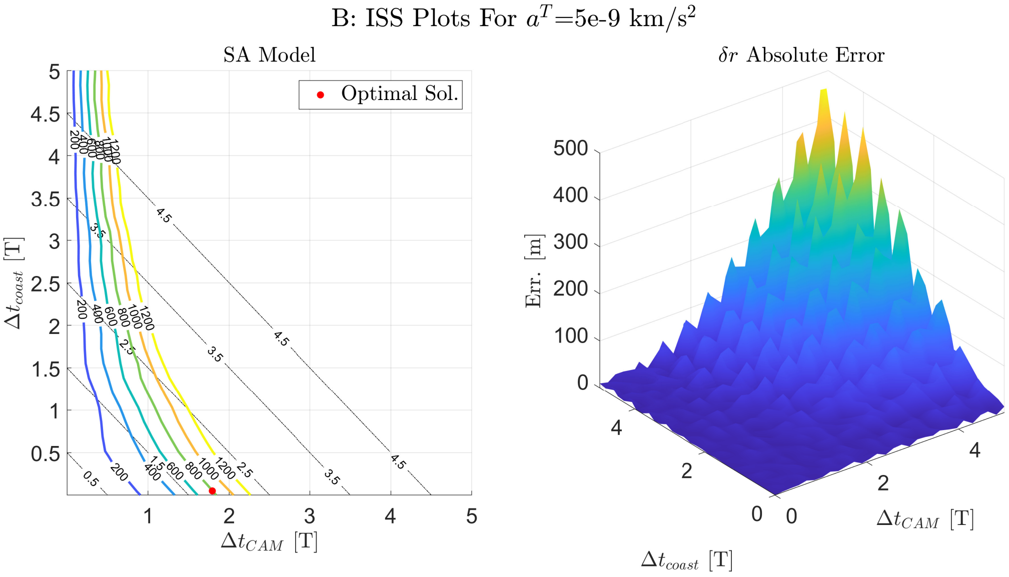

Figure 5.16: CASE B: ISS solution for a^T=5×10^{-9} km/s^2.

Solution Analysis

Each plot shows how the sub-optimal solution tends to move towards low CAM times as the acceleration level increases, minimizing the coasting time down to zero.

The coordinates of each sub-optimal solution are reported in Table 5.8 together with the total time Δt, the manoeuvre cost Δv and the computational time (both numerical and SA) to solve the 50x50 grid; the global optimal solution is reached for a thrust acceleration of 5e-9 km/s^2 which grants the minimum time to complete the overall CAM, in particular this solution uses all of the LT propulsion capability to perform the overall powered arc, followed then by a short coasting phase to reach the wanted miss distance.

For the other cases instead the acceleration a^T is too small to reach the maximum Δv: this one can be reached only by increasing the manoeuvring time Δt_{CAM} leading to higher miss distances.

However the sub-optimal solution will not reach this saturation condition for Δv since the following problem wants to minimise the overall time and it is not needed to have higher miss distances than 800 meters.

a^T $[\frac{km}{s^2}]$	δr **[m]**	Δt_{CAM} **[T]**	Δt_{coast} **[T]**	Δt **[T]**	Δv $[\frac{cm}{s}]$	t^{an}_{CPU} **[s]**	t^{num}_{CPU} **[s]**
1e-9	≈ 800	4.0940	≈ 0	4.0940	2.2847	40.78	3437.38
2e-9	≈ 800	2.9182	≈ 0	2.9182	3.2570	40.22	3348.64
3e-9	≈ 800	2.4048	≈ 0	2.4048	4.0260	40.37	3042.16
4e-9	≈ 800	2.0535	≈ 0	2.0535	4.5838	40.14	3121.51
5e-9	≈ 800	1.7920	0.0500	1.8420	5.0000	39.81	2944.12

Table 5.8: Case B: ISS results for different a^T.

The results are summarized as follows:

- The CAM starts on **June 23rd 2023** at **7:05 a.m.(GMT)**;
- An acceleration of **5e-9 km/s^2** tilted of **5 deg** from the tangential direction is adopted;
- The powered leg lasts approximately **2h 47 min** (10000 s);
- The coasting leg lasts **5 min** (280 s);
- The total time of the manoeuvre (powered+coasting) is about **2 h 51 min**;
- The cost of the manoeuvre is **5.0000 cm/s**;
- The final miss distance, reached through the manoeuvre, is about **800 m**;
- To solve the 50x50x5 grid and compute the solution the **SA** propagator takes **201.32 s** whereas the **numerical** takes **15893.81 s**;

In case B, the numerical integration takes more than four hours to solve a 50x50x5 grid, whereas the SA one takes less than four minutes, so in terms of computational cost the SA propagator outperforms the numerical one of almost two orders of magnitude; the SA model is also accurate as shown in Table 5.9 where an error of only **10 s** is committed in the overall time Δt (precisely during the coasting arc) with respect to the numerical one. The use of the SA propagator is particularly essential in this specific case where the time between the detection of CA and the CA itself is very short and so the design of the manoeuvre has to be carried out as soon as possible.

	δr **[m]**	Δt_{CAM} **[T]**	Δt_{coast} **[T]**	Δv **[$\frac{cm}{s}$]**	t_{CPU} **[s]**
SA	≈ 800	1.7920	0.0500	5.0000	39.81
NUM	≈ 800	1.7920	0.0519	5.0000	2944.12

Table 5.9: Case B: ISS results from numerical and SA models for a^T=5e-9 km/s^2.

5.4.2. Case B : Optimisation on GEO

Problem Statement

In this test case, a CA is detected on 6th February 2023 at 3:23 a.m. (GMT), the states of both the GEO and debris are reported in Table 5.10 and the goal is to reach a miss distance of about 1100 meters (or more), by minimizing the overall time.
Moreover the cost of the manoeuvre must be lower than 7.5 cm/s.

	a **[km]**	e **[-]**	i **[deg]**	ω **[deg]**	Ω **[deg]**	θ **[deg]**	$\frac{A}{m}$ **[$\frac{m^2}{kg}$]**	C_R **[-]**
GEO$_2$	42165	.0010	1.00	65.00	70.00	150.00	0.010	1.1
DEB	38963	.2500	145.80	236.45	284.15	122.53	-	-

Table 5.10: Case B: Orbital parameters of GEO$_2$ and debris at CA.

The mathematical formulation of the problem is instead reported below:

$$\begin{cases} \min \Delta t = \min \left(\Delta t_{CAM} + \Delta t_{coast}\right) \\ \delta r \geq 1100 \text{ m} \\ \Delta v \leq 7.5 \text{ cm/s} \end{cases} \tag{5.4}$$

Optimisation Analysis

As done until now, the free variables are reduced to three by assuming a constant value for γ_t which is fixed to 5 degrees.
Different values for Δt_{CAM} and Δt_{coast} are used in the analysis which go from 0 to 0.45 orbital periods in 50 equi-spaced steps, whereas five acceleration levels are considered which go from 1e-9 to 4e-9 km/s^2, so the final 50x50x5 grid is defined.
The results of each parametric analysis are then shown in the following figures (Fig 5.17, 5.18, 5.19, 5.20, 5.21):

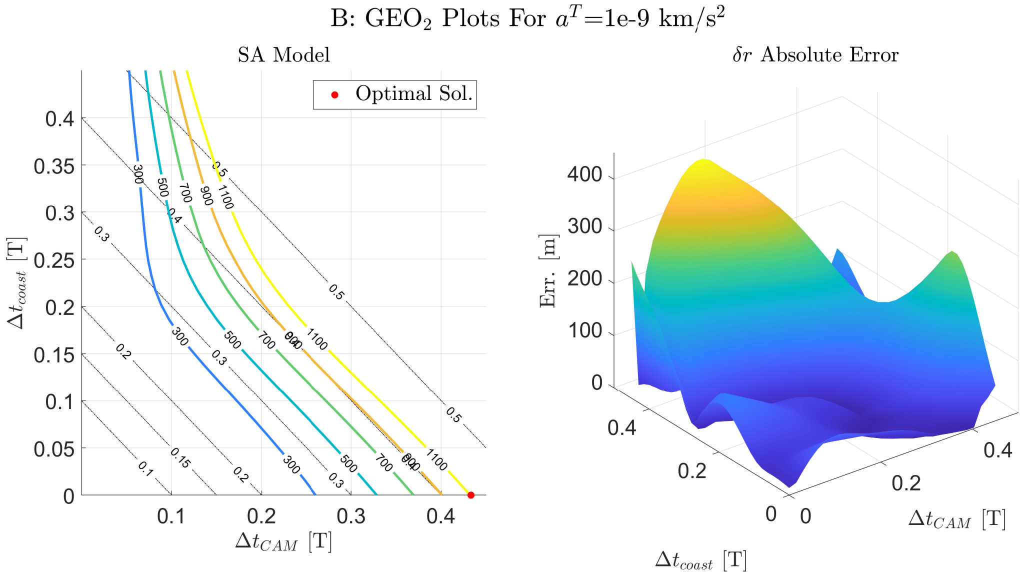

Figure 5.17: CASE B: GEO$_2$ solution for a^T=1×10^{-9} km/s^2.

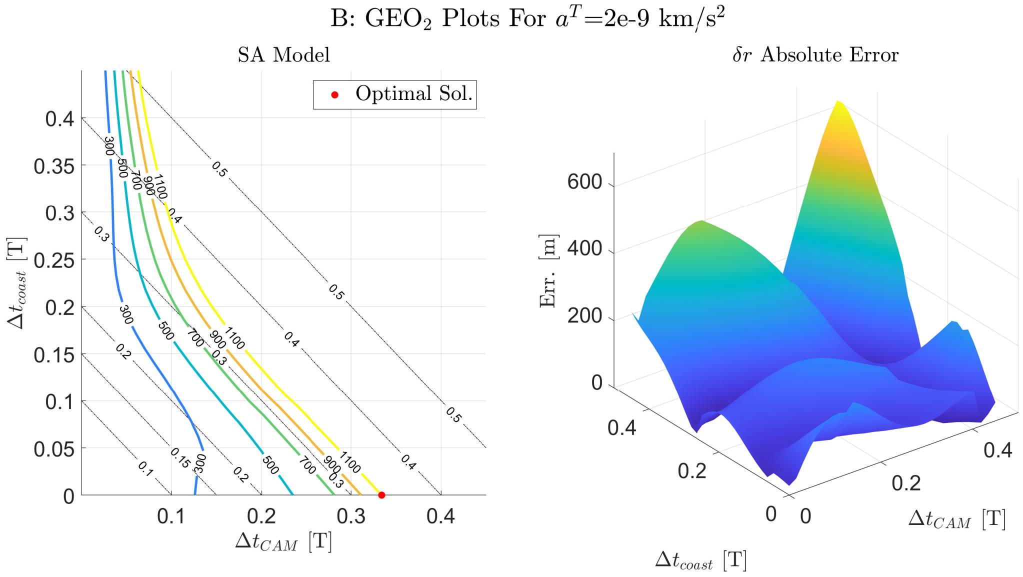

Figure 5.18: CASE B: GEO$_2$ solution for a^T=2×10^{-9} km/s^2.

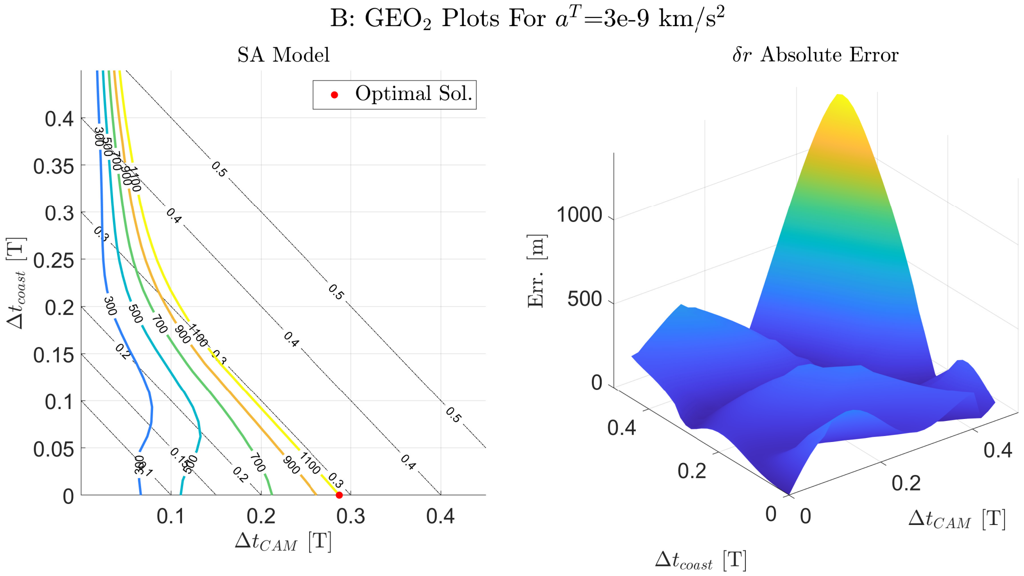

Figure 5.19: CASE B: GEO$_2$ solution for a^T=3×10^{-9} km/s^2.

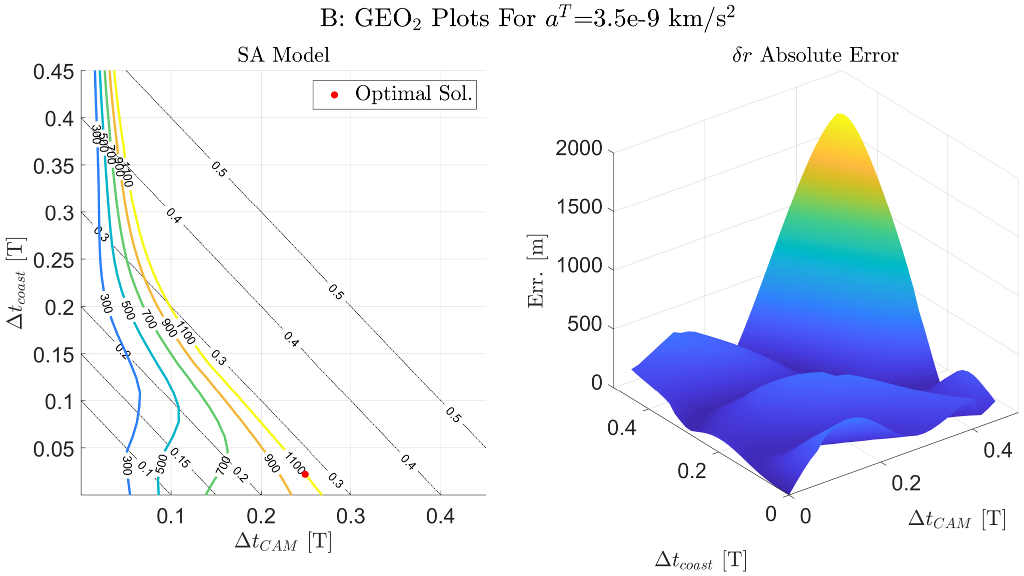

Figure 5.20: CASE B: GEO$_2$ solution for a^T=3.5×10^{-9} km/s^2.

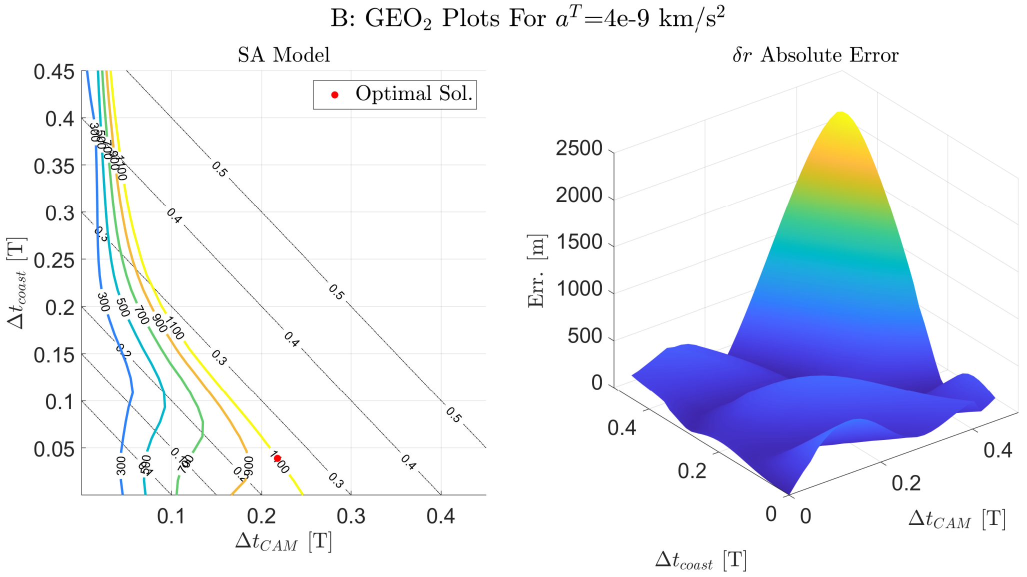

Figure 5.21: CASE B: GEO$_2$ solution for a^T=4×10^{-9} km/s^2.

Solution Analysis

As it happens for the LEO case, also in GEO the plots show how the sub-optimal solution move towards low CAM times as the acceleration level increases, minimizing the coasting time down to zero as long as the constraint on Δv is satisfied; the results of each sub-optimal solution are reported in Table 5.11.

The global optimal solution is reached for a thrust acceleration of 4e-9 km/s^2 which grants the minimum time to complete the overall CAM, and also here the solution uses all of the LT propulsion capability to perform the powered arc followed by a short coasting phase to reach the wanted miss distance.

It can be noticed that the last four figures show some folds in the contour plots, these are mainly due to the errors in the SA GEO model: as the thrust acceleration increases, the errors of GEO in analytical tangential and normal models become more relevant.

If the error is contained then only small δr curves will be affected by it, leading to a fold (Fig. 5.18 and 5.19), but as the error increases then also the curves of large miss distances will be affected and so the number of folds increases for higher a^T (Fig. 5.20 and 5.21); this explains why, to avoid big errors, for this test case the accelerations are considered only up to 4e-9 km/s^2.

a^T [$\frac{km}{s^2}$]	δ**r** [m]	Δt_{CAM} [T]	Δt_{coast} [T]	Δt [T]	Δv [$\frac{cm}{s}$]	t^{an}_{CPU} [s]	t^{num}_{CPU} [s]
1e-9	≈ 1100	0.4332	≈ 0	0.4332	3.7323	54.05	126.00
2e-9	≈ 1100	0.3340	≈ 0	0.3340	5.7559	53.73	128.30
3e-9	≈ 1100	0.2872	≈ 0	0.2872	7.4241	53.65	126.06
3.5e-9	≈ 1100	0.2487	0.0221	0.2708	7.5000	53.77	128.52
4e-9	≈ 1100	0.2176	0.0389	0.2565	7.5000	53.93	128.86

Table 5.11: Case B: GEO_2 results for different a^T.

Once the final solution is carried out, the results can be summarized as follows:

- The CAM starts on **February 5**th **2023** at **9:15 p.m.(GMT)**;
- An acceleration of **4e-9 km/s**^{2} tilted of **5 deg** from the tangential direction is adopted;
- The powered leg lasts approximately **5h 12 min** (18750 s);
- The coasting leg lasts **56 min** (3352 s);
- The total time of the manoeuvre (powered+coasting) is about **6 h 8 min**;
- The cost of the manoeuvre is **7.5000 cm/s**;
- The final miss distance, reached through the manoeuvre, is about **1100 m**;
- To solve the 50x50x5 grid and compute the solution the **SA** propagator takes **269.13 s** whereas the **numerical** takes **637.74 s**;

As in case A of GEO_1, also here for GEO_2, the difference in computational time between the SA and numerical methods is not that huge.
By testing the accuracy of the two models, Table 5.12 shows an error of **17 min** in the overall time, precisely in the coasting time that actually lasts about **1 h 12 min**, leading to a total time Δt of **6 h 25 min**, although the error in this case is smaller with respect to the first GEO case and the SA is still faster than the numerical model, the use of the SA propagator is not convenient since the saving in time is reduced to only **6 min**.

	δr **[m]**	Δt_{CAM} **[T]**	Δt_{coast} **[T]**	Δv **[$\frac{cm}{s}$]**	t_{CPU} **[s]**
SA	$\approx$ 1100	0.2176	0.0389	7.5000	53.93
NUM	$\approx$ 1100	0.2176	0.0505	7.5000	128.86

Table 5.12: Case B: GEO$_2$ results from numerical and SA models for a^T=4e-9 km/s^2.

5.5. Case C : Cost Minimization for Given PoC

This problem is similar to that proposed in case A, with the only exception that the goal is to reach a fixed *PoC* minimizing the cost Δv, the computation of PoC was already treated in Section 5.1.2 for which a combined radius s_a of 10 meters and a covariance matrix reported in Eq. (5.5), projected in ξ-ζ directions, were adopted for both LEO and GEO regions.

$$\boldsymbol{C}_{\xi\zeta} = \begin{bmatrix} 0.02\ km^2 & 0 \\ 0 & 0.8\ km^2 \end{bmatrix} \tag{5.5}$$

5.5.1. Case C : Optimisation on LEO

Problem Statement

Case C is characterized by a CA detected on 21st September 2023 at 1:13 p.m. (GMT), the states of satellite and debris are reported in Table 5.13 and the goal is to reach a PoC of 1×10^{-5} (or less) by minimizing the total cost Δv of the CAM.

Lastly the overall manoeuvre cannot last more than four periods of the nominal orbit.

	$\boldsymbol{a}$ **[km]**	$\boldsymbol{e}$ **[-]**	$\boldsymbol{i}$ **[deg]**	ω **[deg]**	Ω **[deg]**	θ **[deg]**	$\frac{A}{m}$ **[$\frac{m^2}{kg}$]**	C_D **[-]**
LEO$_2$	7100	.0100	30.00	10.00	10.00	80.00	0.010	2.0
DEB	7114	.0059	30.00	38.47	10.75	50.87	-	-

Table 5.13: Case C: Orbital parameters of LEO$_2$ and debris at CA.

Below it is reported the mathematical formulation of the problem:

$$\begin{cases} \min\ \Delta v = \min\ a^T \Delta t_{CAM} \\ \text{PoC} \leq 1e-5 \\ \Delta t \leq 4.0\ \text{T} \end{cases} \tag{5.6}$$

Optimisation Analysis

For this test case the thrust vector is tilted of ten degrees from the tangential direction and, as done until now, a 50x50x5 grid for Δt_{CAM}, Δt_{coast} (from 0 to four periods) and a^T (from 1e-9 to 5e-9 km/s^2) is adopted to perform the parametric analysis.
Next figures (Fig 5.22, 5.23, 5.24, 5.25 and 5.26) show the contour plots from the parametric analysis for each thrust acceleration, in this case each curve line represents a certain PoC and the absolute error is computed on it.

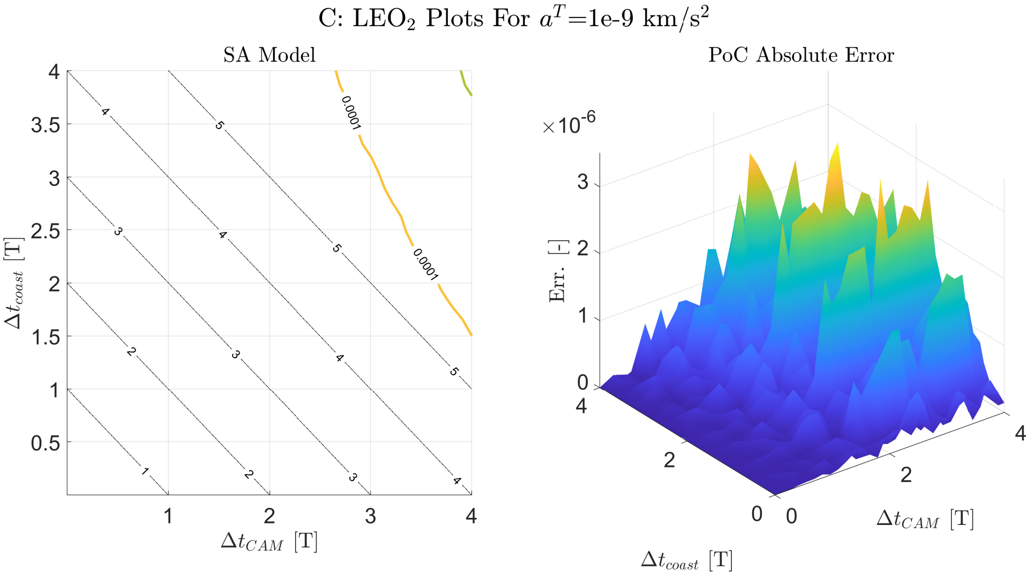

Figure 5.22: CASE C: LEO$_2$ solution for a^T=1×10^{-9} km/s^2.

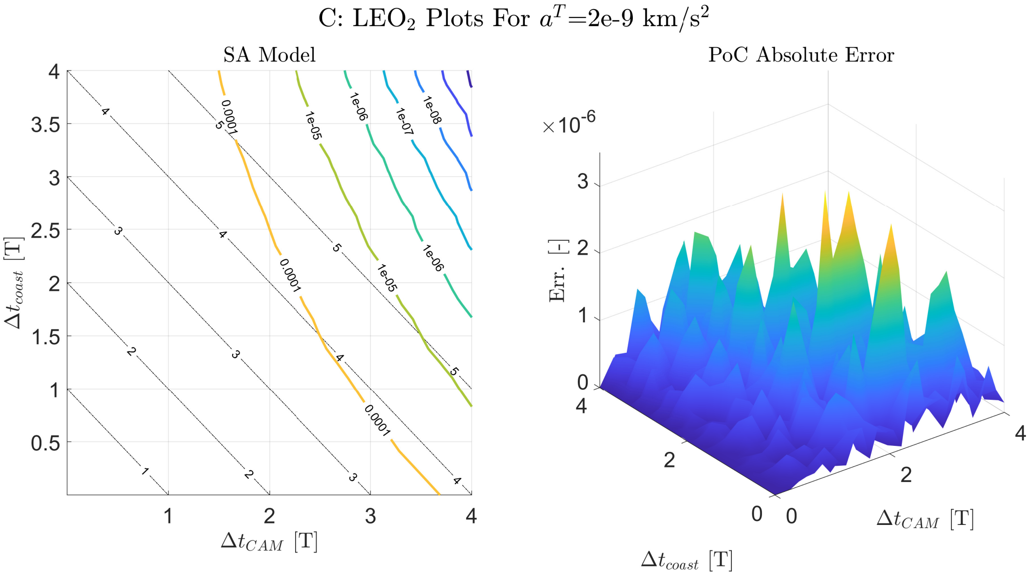

Figure 5.23: CASE C: LEO$_2$ solution for a^T=2×10^{-9} km/s^2.

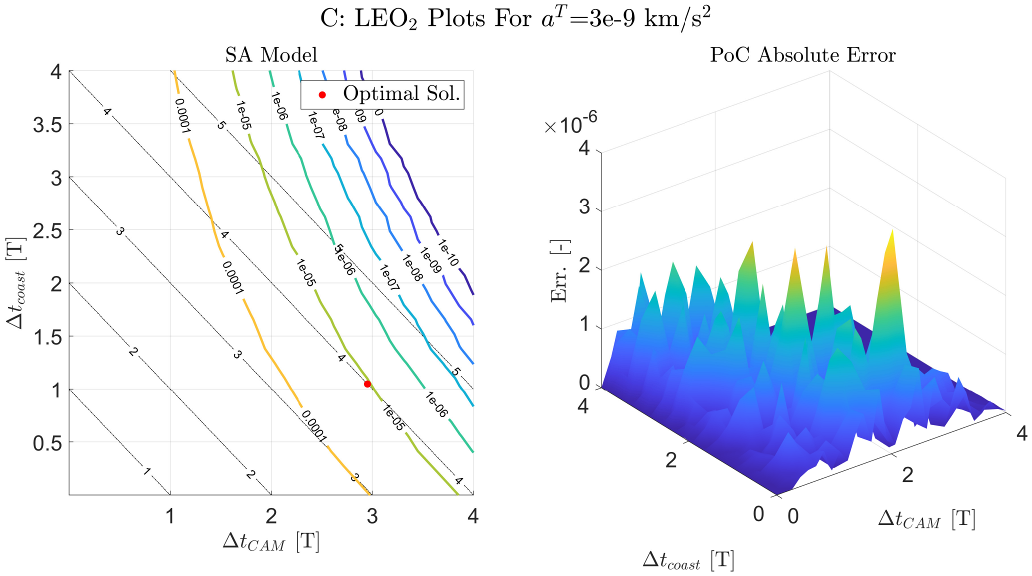

Figure 5.24: CASE C: LEO$_2$ solution for a^T=3×10^{-9} km/s^2.

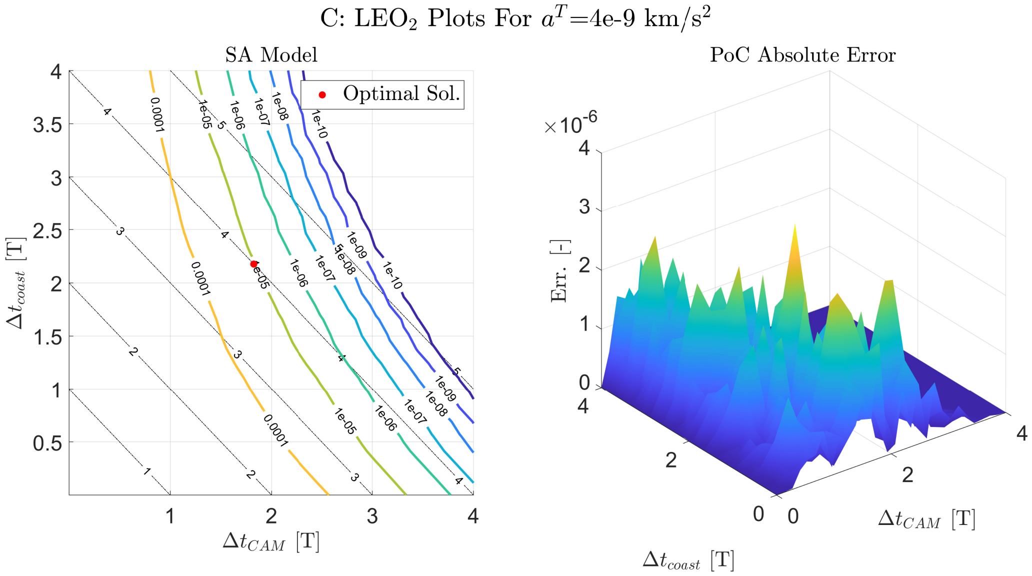

Figure 5.25: CASE C: LEO$_2$ solution for a^T=4×10^{-9} km/s^2.

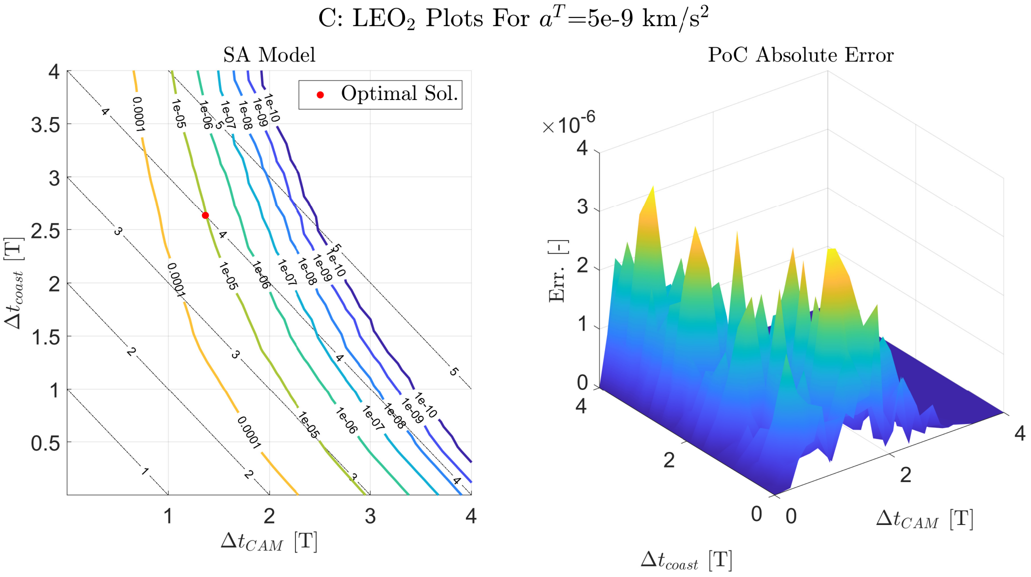

Figure 5.26: CASE C: LEO$_2$ solution for a^T=5×10^{-9} km/s^2.

Solution Analysis

Each plot shows how the sub-optimal solution tends to move towards low CAM times and high coasting times as the acceleration level increases; Table 5.14 summarizes the results obtained from the contour plot reporting the computational time.

In this case the global optimal solution is reached for a thrust acceleration of 5e-9 km/s^2 which grants the minimum cost to complete the overall CAM whereas for thrust accelerations of 1e-9 and 2e-9 km/^{2} no feasible solutions are detected considering the adopted constraints.

a^T [$\frac{km}{s^2}$]	PoC [-]	Δt_{CAM} [T]	Δt_{coast} [T]	Δt [T]	Δv [$\frac{cm}{s}$]	t^{an}_{CPU} [s]	t^{num}_{CPU} [s]
1e-9	-	-	-	-	-	39.32	1038.00
2e-9	-	-	-	-	-	38.69	1059.58
3e-9	$\approx$ 1e-5	2.9516	1.0484	4.0000	5.2720	38.71	1007.31
4e-9	$\approx$ 1e-5	1.8240	2.1760	4.0000	4.3439	39.72	996.51
5e-9	$\approx$ 1e-5	1.3664	2.6335	3.9999	4.0677	39.53	1054.46

Table 5.14: Case C: LEO$_2$ results for different a^T.

The final result can be summarized as follows:

- The CAM starts on **September 21st 2023** at **6:36 a.m.(GMT)**;

- An acceleration of **5e-9 km/s^2** tilted of **10 deg** from the tangential direction is adopted;
- The powered leg lasts approximately **2 h 15 min** (8135 s);
- The coasting leg lasts **4 h 21 min** (280 s);
- The total time of the manoeuvre (powered+coasting) is about **6 h 37 min**;
- The cost of the manoeuvre is **4.0677 cm/s**;
- The final PoC, reached through the manoeuvre, is about **1e-5**;
- To solve the 50x50x5 grid and compute the solution the **SA** propagator takes **195.97 s** whereas the **numerical** takes **5155.86 s**;

Also in this case the SA propagator is more efficient with respect to the numerical one, leading to the solution of the whole grid in just three minutes, the accuracy of the optimal solution is instead reported in Table 5.15 where an error of only **35 s** is committed in both the coasting and CAM times, whereas the error in Δv is of **0.0174 cm/s**.

	PoC [-]	Δt_{CAM} **[T]**	Δt_{coast} **[T]**	Δv **[$\frac{cm}{s}$]**	t_{CPU} **[s]**
SA	≈ 1e-5	1.3664	2.6335	4.0677	39.53
NUM	≈ 1e-5	1.3722	2.6277	4.0851	1054.46

Table 5.15: Case C: LEO$_2$ results from numerical and SA models for a^T=5e-9 km/s^2.

5.5.2. Case C : Optimisation on GEO

Problem Statement

Test case C is now tested on a GEO: a CA is detected on 9th November 2023 at 9:49 p.m. (GMT) with the states of s/c and debris defined in Table 5.16; the goal is to obtain a PoC of 1e-5 (or less) in less than 0.3 orbital periods, by minimising the total cost Δv.

	a **[km]**	e **[-]**	i **[deg]**	ω **[deg]**	Ω **[deg]**	θ **[deg]**	$\frac{A}{m}$ **[$\frac{m^2}{kg}$]**	C_D **[-]**
GEO$_3$	42165	.0010	1.00	30.00	30.00	40.00	0.010	1.2
DEB	38845	.3128	35.16	124.17	98.66	237.46	-	-

Table 5.16: Case C: Orbital parameters of GEO$_3$ and debris at CA.

The mathematical formulation of the problem is reported here:

$$\begin{cases} \min \Delta v = \min a^T \Delta t_{CAM} \\ \text{PoC} \leq 1e-5 \\ \Delta t \leq 0.3 \text{ T} \end{cases} \tag{5.7}$$

Optimisation Analysis

For this test case the thrust vector is aligned with the tangential direction and a 50x50x5 grid for Δt_{CAM}, Δt_{coast} (from 0 to 0.3 periods) and a^T (from 1e-9 to 5e-9 km/s^2) is adopted to perform the parametric analysis.
Fig 5.27, 5.28, 5.29, 5.30 and 5.31 show the contour plots of the SA parametric analysis for each thrust acceleration, with their absolute errors.

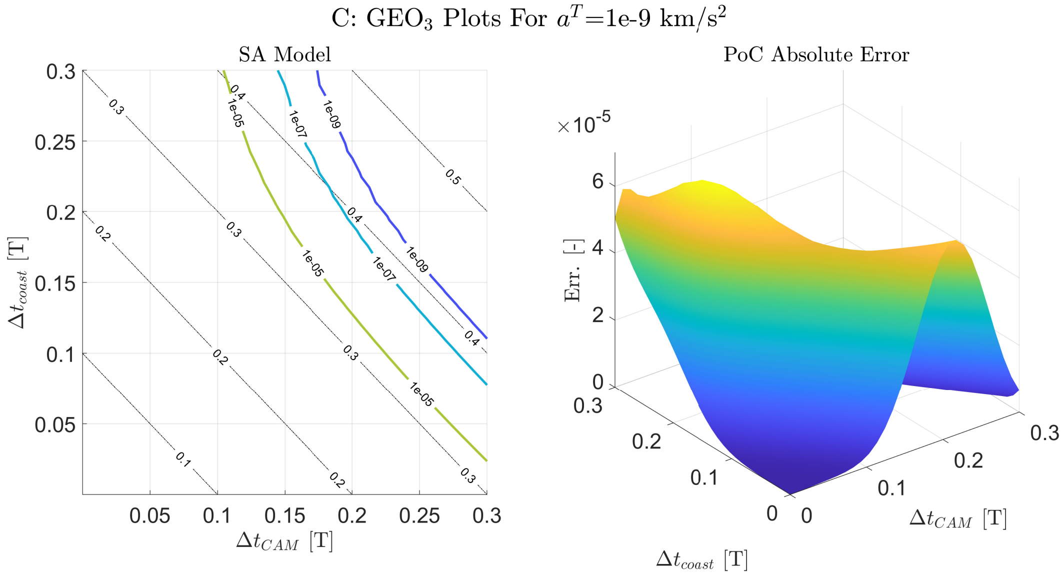

Figure 5.27: CASE C: GEO$_3$ solution for a^T=1$\times$10^{-9} km/s^2.

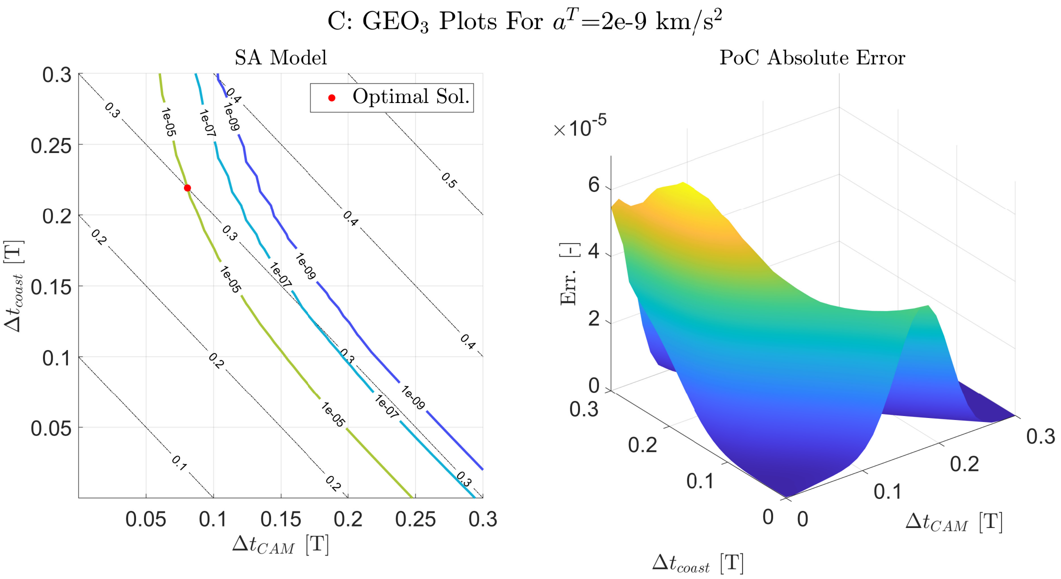

Figure 5.28: CASE C: GEO$_3$ solution for a^T=2×10^{-9} km/s^2.

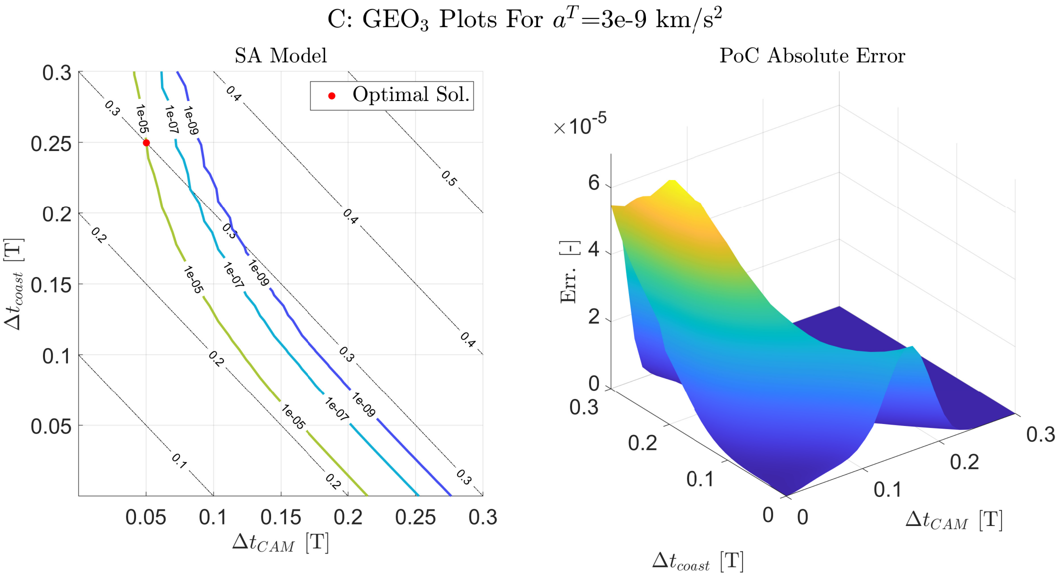

Figure 5.29: CASE C: GEO$_3$ solution for a^T=3×10^{-9} km/s^2.

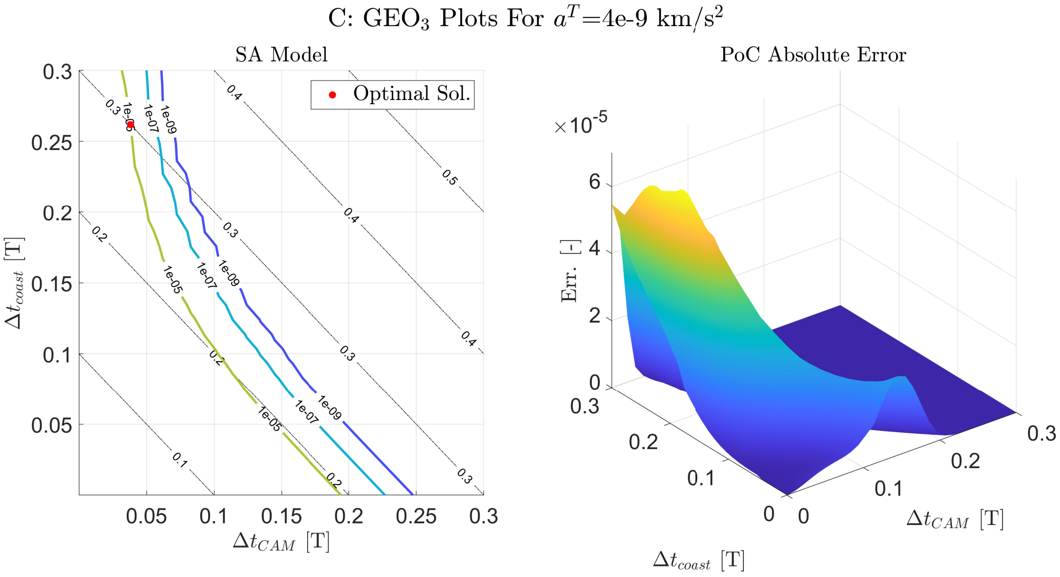

Figure 5.30: CASE C: GEO$_3$ solution for a^T=4×10^{-9} km/s^2.

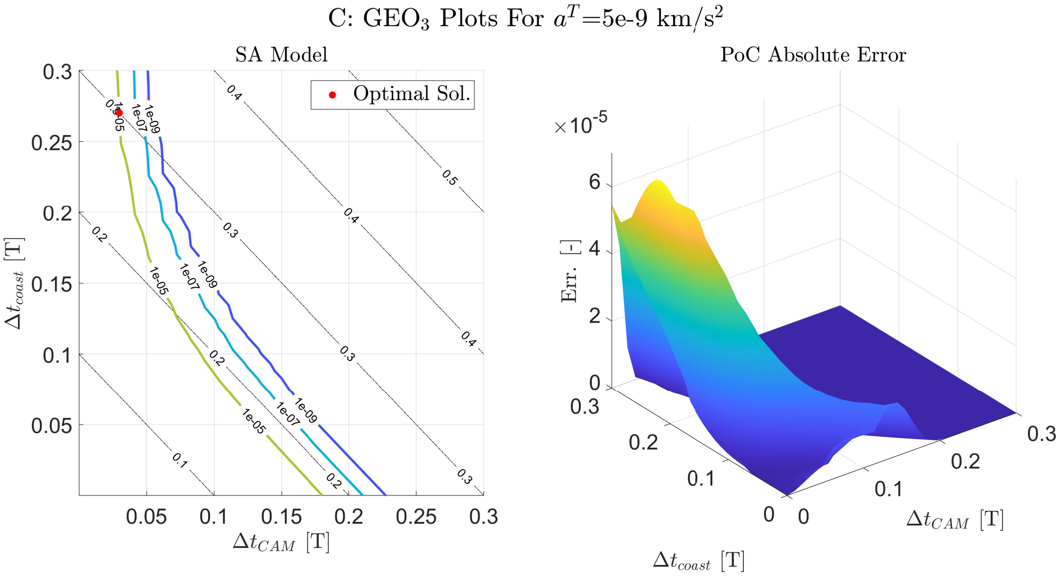

Figure 5.31: CASE C: GEO$_3$ solution for a^T=5×10^{-9} km/s^2.

Solution Analysis

The results of each sub-optimal solution are reported in Table 5.17; the global optimal solution is reached for a thrust acceleration of 5e-9 km/s^2 which grants the minimum cost to complete the manoeuvre and reach the desired PoC.

a^T [$\frac{km}{s^2}$]	**PoC [-]**	Δt_{CAM} **[T]**	Δt_{coast} **[T]**	Δt **[T]**	Δv [$\frac{cm}{s}$]	t_{CPU}^{an} **[s]**	t_{CPU}^{num} **[s]**
1e-9	-	-	-	-	-	50.50	81.69
2e-9	≈ 1e-5	0.0807	0.2193	0.3000	1.3907	49.92	86.75
3e-9	≈ 1e-5	0.0503	0.2497	0.3000	1.2995	51.74	84.20
4e-9	≈ 1e-5	0.0382	0.2618	0.3000	1.3149	52.63	86.71
5e-9	≈ 1e-5	0.0299	0.2701	0.3000	1.2870	53.31	85.81

Table 5.17: Case C: GEO_3 results for different a^T.

The results are lastly summarized as follows:

- The CAM starts on **November 9th 2023** at **2:38 p.m.(GMT)**;
- An acceleration of **5e-9 km/s^2** aligned with the tangential direction is adopted;
- The powered leg lasts approximately **43 min** (2574 s);
- The coasting leg lasts **6 h 28 min** (23276 s);
- The total time of the manoeuvre (powered+coasting) is about **7 h 11 min**;
- The cost of the manoeuvre is **1.2870 cm/s**;
- The final PoC, reached through the manoeuvre, is about **1e-5**;
- To solve the 50x50x5 grid and compute the solution the **SA** propagator takes **258.10 s** whereas the **numerical** takes **425.16 s**;

Also here for GEO_3, the difference in computational time between the SA and numerical methods is minimum.
By testing the accuracy of the two models, Table 5.18 shows an error of **1 min** in both the CAM and coasting times and of **0.0400 cm/s** in Δv, the error in this case is much smaller with respect to the other two GEO cases with the SA still faster than the numerical model but not as convenient.

	PoC [-]	Δt_{CAM} **[T]**	Δt_{coast} **[T]**	Δv [$\frac{cm}{s}$]	t_{CPU} **[s]**
SA	≈ 1e-5	0.0299	0.2701	1.2870	53.31
NUM	≈ 1e-5	0.0308	0.2692	1.3300	85.81

Table 5.18: Case C: GEO_3 results from numerical and SA models for a^T=5e-9 km/s^2.

5.6. Case D : PoC Minimisation in a Given Time

The final optimisation problem that is analyzed is based on the minimisation of PoC within a given time Δt; this problem is very useful for the cases where CAs are detected at the last moment, making it similar to **Case B** with the only difference that there is not a defined target; moreover for the computation of PoC, Chan's algorithm will be used together with the same covariance matrix adopted in Eq. (5.5) and a combined radius s_a of ten meters.

5.6.1. Case D : Optimisation on LEO

Problem Statement

In Case D the CA is detected on 27th July 2023 at 4:45 p.m. (GMT), the states of satellite and debris are reported in Table 5.19 and the goal is to minimize the PoC between satellite and debris within two orbital periods of the nominal orbit; the problem has also a constraint on the overall propulsion capability Δv which cannot exceed 6.0 cm/s.

	a [km]	e [-]	i [deg]	ω [deg]	Ω [deg]	θ [deg]	$\frac{A}{m}$ [$\frac{m^2}{kg}$]	C_D [-]
LEO$_3$	7050	.0034	22.00	5.00	50.00	120.00	0.005	2.0
DEB	6945	.0445	20.11	2.28	58.77	114.53	-	-

Table 5.19: Case D: Orbital parameters of LEO$_3$ and debris at CA.

Below it is reported the mathematical formulation of the problem:

$$\begin{cases} \text{min PoC} \\ \Delta v \leq 6.0 \text{ cm/s} \\ \Delta t \leq 2.0 \text{ T} \end{cases} \tag{5.8}$$

Optimisation Analysis

For this test case the thrust vector is tilted of seven degrees and a 50x50x5 grid for Δt_{CAM}, Δt_{coast} (from 0 to two periods) and a^T (from 1e-9 to 5e-9 km/s^2) is adopted to perform the parametric analysis whose contour plots are reported in the figures below (Fig. 5.32, 5.33, 5.34, 5.35, 5.36) together with the optimal solution and the error in PoC.

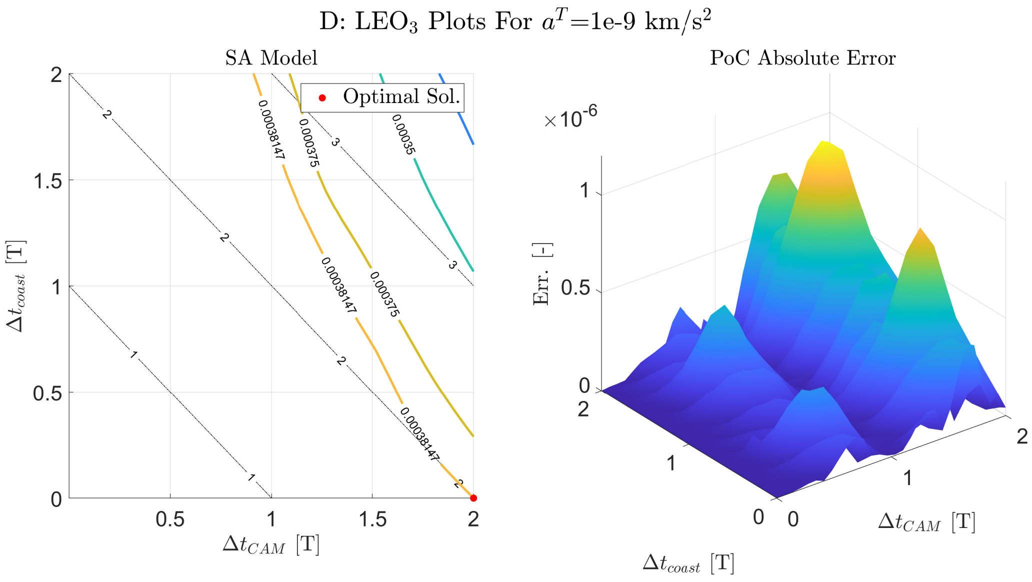

Figure 5.32: CASE D: LEO$_3$ solution for a^T=1$\times$10^{-9} km/s^2.

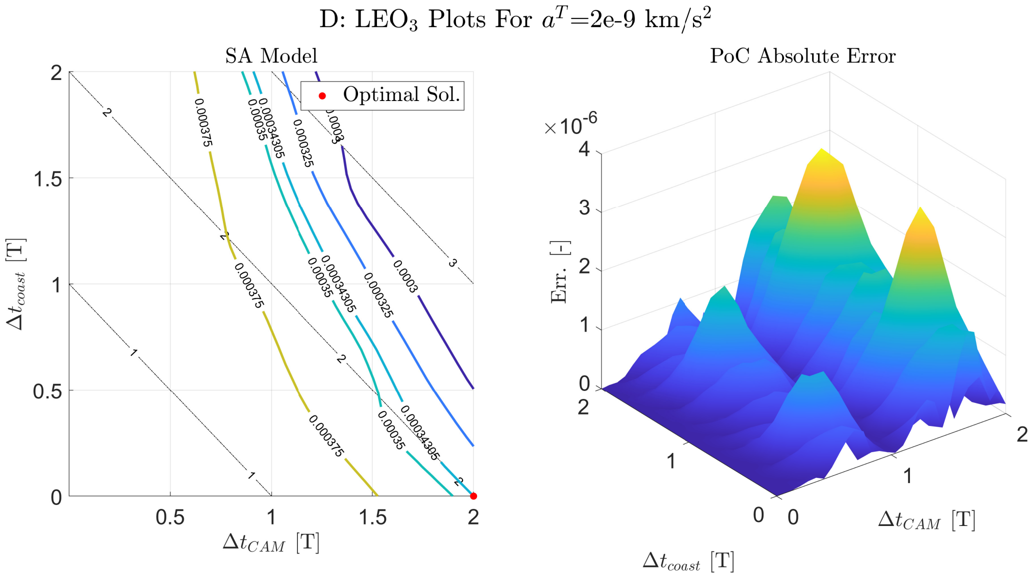

Figure 5.33: CASE D: LEO$_3$ solution for a^T=2$\times$10^{-9} km/s^2.

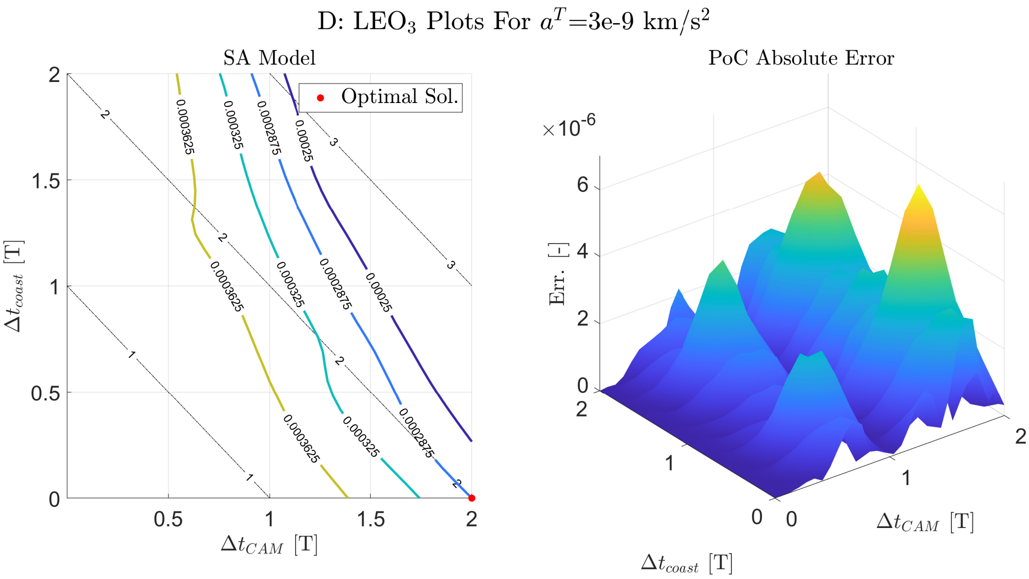

Figure 5.34: CASE D: LEO$_3$ solution for a^T=3×10^{-9} km/s^2.

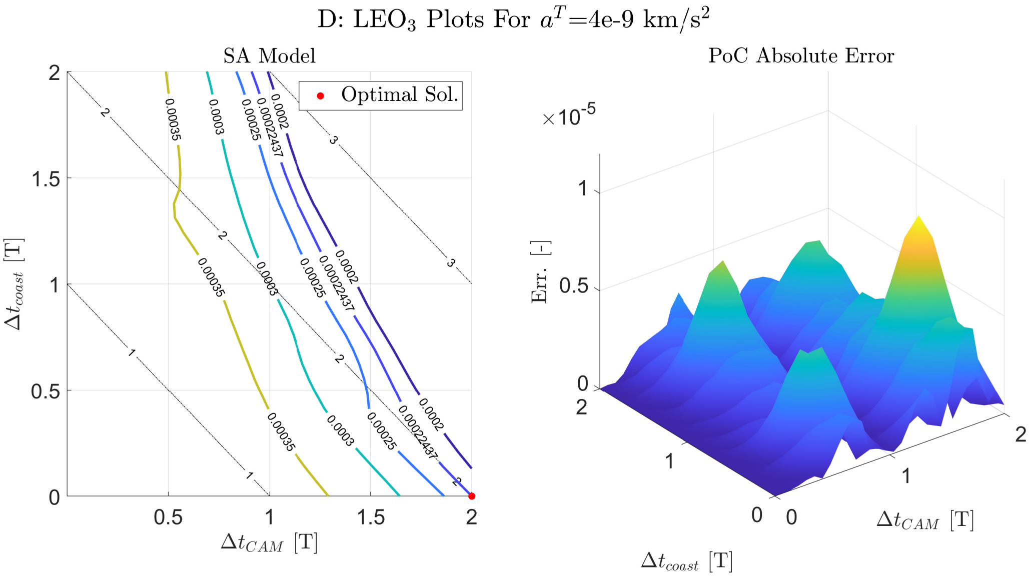

Figure 5.35: CASE D: LEO$_3$ solution for a^T=4×10^{-9} km/s^2.

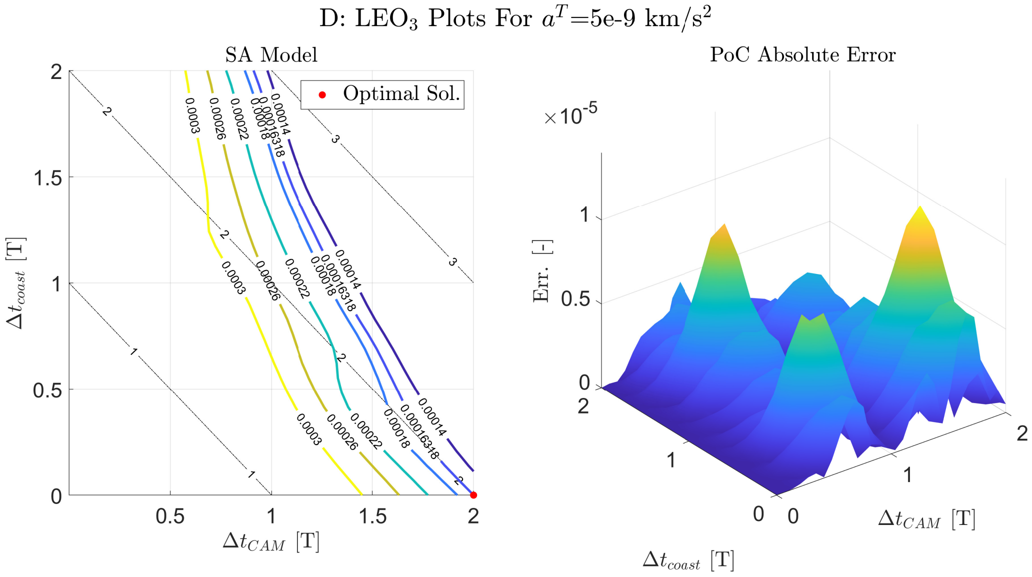

Figure 5.36: CASE D: LEO$_3$ solution for a^T=5×10^{-9} km/s^2.

Solution Analysis

Each plot shows how the sub-optimal solution is reached by maximising the powered arc which leads to a null coasting phase, this is intuitive since during an emergency case like this one where time is precious, the propulsion system must work for the duration of the overall manoeuvre; lastly the results of each plot are reported in Table 5.20:

a^T $[\frac{km}{s^2}]$	**PoC [-]**	Δt_{CAM} **[T]**	Δt_{coast} **[T]**	Δt **[T]**	Δv $[\frac{cm}{s}]$	t_{CPU}^{an} **[s]**	t_{CPU}^{num} **[s]**
1e-9	3.81e-4	2.0000	0.0000	2.0000	1.1782	41.01	505.21
2e-9	3.43e-4	2.0000	0.0000	2.0000	2.3564	40.99	507.78
3e-9	2.87e-4	2.0000	0.0000	2.0000	3.5346	40.80	505.68
4e-9	2.24e-4	2.0000	0.0000	2.0000	4.7129	42.22	505.26
5e-9	1.63e-4	2.0000	0.0000	2.0000	5.8911	39.87	514.08

Table 5.20: Case D: LEO$_3$ results for different a^T.

The final result can be summarized as follows:

- The CAM starts on **July 27th 2023** at **1:29 p.m.(GMT)**;
- An acceleration of **5e-9 km/s^2** tilted of **7 deg** from the tangential direction is adopted;
- The powered leg lasts approximately **3 h 16 min** (11782 s);

- There is no coasting leg;
- The total time of the manoeuvre (powered+coasting) is about **3 h 16 min**;
- The cost of the manoeuvre is **5.8911 cm/s**;
- The final PoC, reached through the manoeuvre, is about **1.63e-4**;
- To solve the 50x50x5 grid and compute the solution the **SA** propagator takes **204.89 s** whereas the **numerical** takes **2538.01 s**;

Also in this time constrained case, the SA propagator is more efficient with respect to the numerical one, leading to the solution of the whole grid in about three minute and saving about forty minutes; the accuracy of the optimal solution is reported in Table 5.21 showing a very small error in the final PoC.

	PoC [-]	Δt_{CAM} **[T]**	Δt_{coast} **[T]**	Δv **[$\frac{cm}{s}$]**	t_{CPU} **[s]**
SA	1.63e-4	2.0000	0.0000	2.0000	39.87
NUM	1.64e-4	2.0000	0.0000	2.0000	514.08

Table 5.21: Case D: LEO_3 results from numerical and SA models for a^T=5e-9 km/s^2.

5.6.2. Case D : Optimisation on GEO

Problem Statement

Test case D is lastly tested on a GEO: the date of CA and the states of s/c and debris are the same adopted in **Case C**, however the goal is to obtain the minimum PoC in less than 0.2 orbital periods, with a maximum Δv of 9.0 cm/s.
The mathematical formulation of the problem is reported below:

$$\begin{cases} \text{min PoC} \\ \Delta v \leq 9.0 \text{ cm/s} \\ \Delta t \leq 0.2 \text{ T} \end{cases} \tag{5.9}$$

Optimisation Analysis

For this test case the already mentioned 50x50x5 grid for Δt_{CAM}, Δt_{coast} (from 0 to 0.2 periods) and a^T (from 1e-9 to 5e-9 km/s^2) is adopted to perform the parametric analysis. Figures 5.37, 5.38, 5.39, 5.40 and 5.41 show the contour plots of the SA parametric analysis for each thrust acceleration, with their absolute errors.

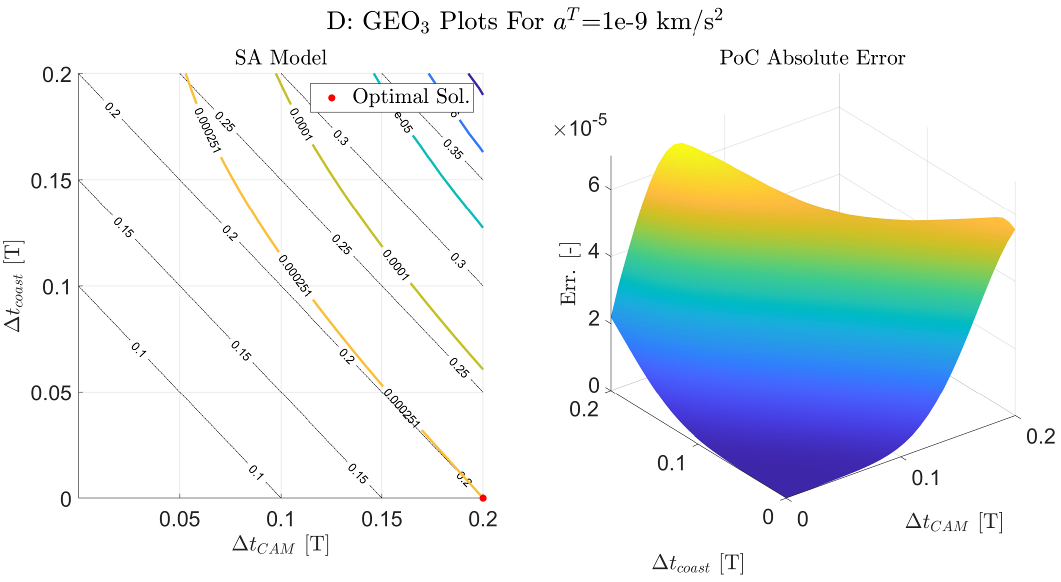

Figure 5.37: CASE D: GEO$_3$ solution for a^T=1×10^{-9} km/s^2.

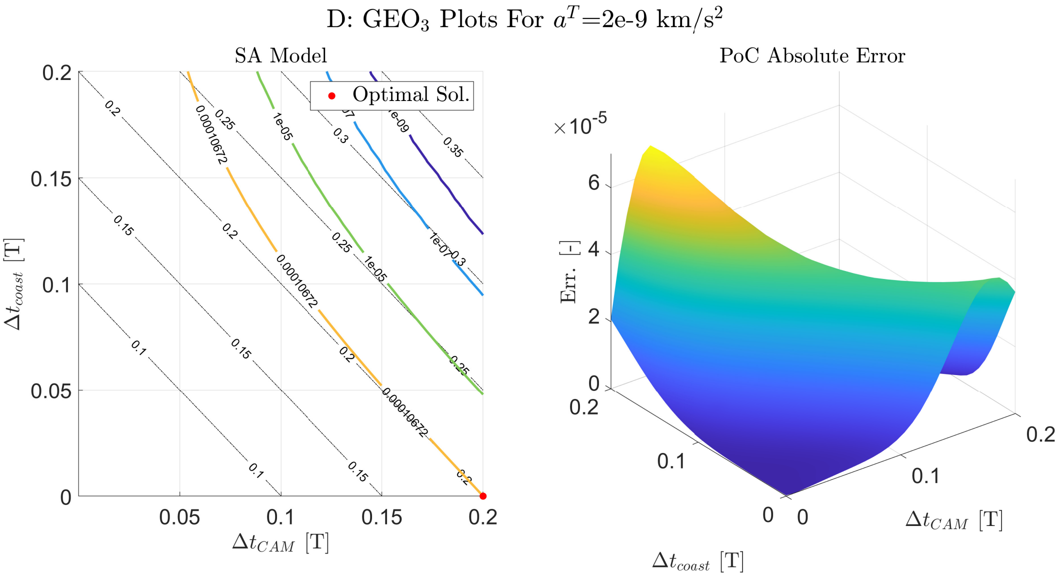

Figure 5.38: CASE D: GEO$_3$ solution for a^T=2×10^{-9} km/s^2.

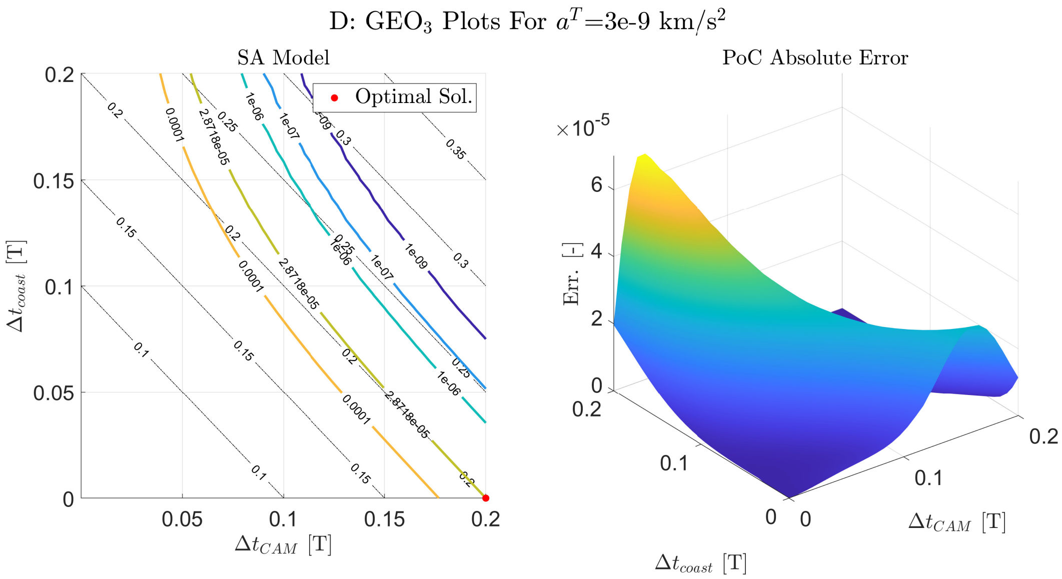

Figure 5.39: CASE D: GEO$_3$ solution for a^T=3×10^{-9} km/s^2.

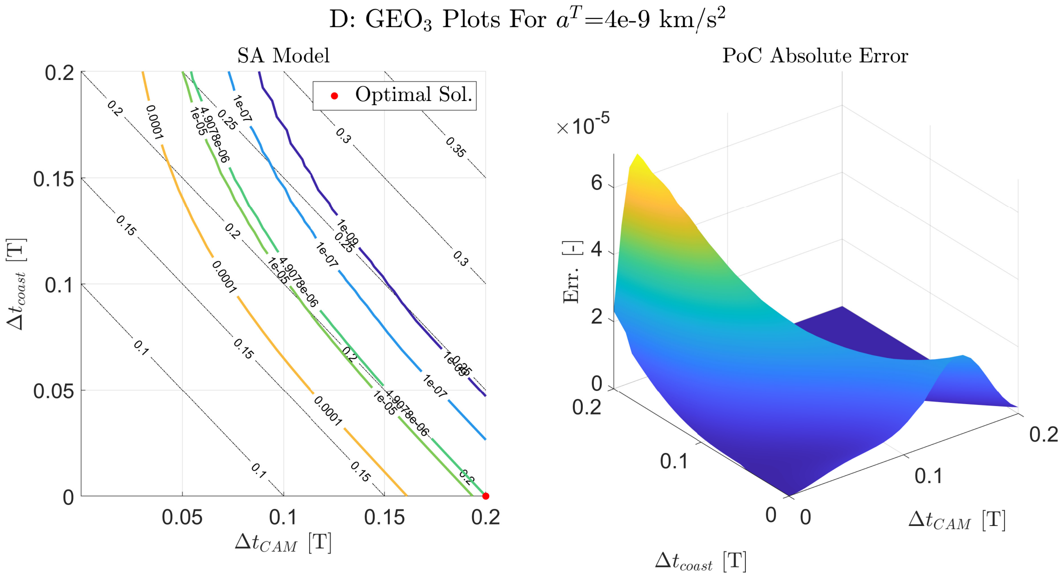

Figure 5.40: CASE D: GEO$_3$ solution for a^T=4×10^{-9} km/s^2.

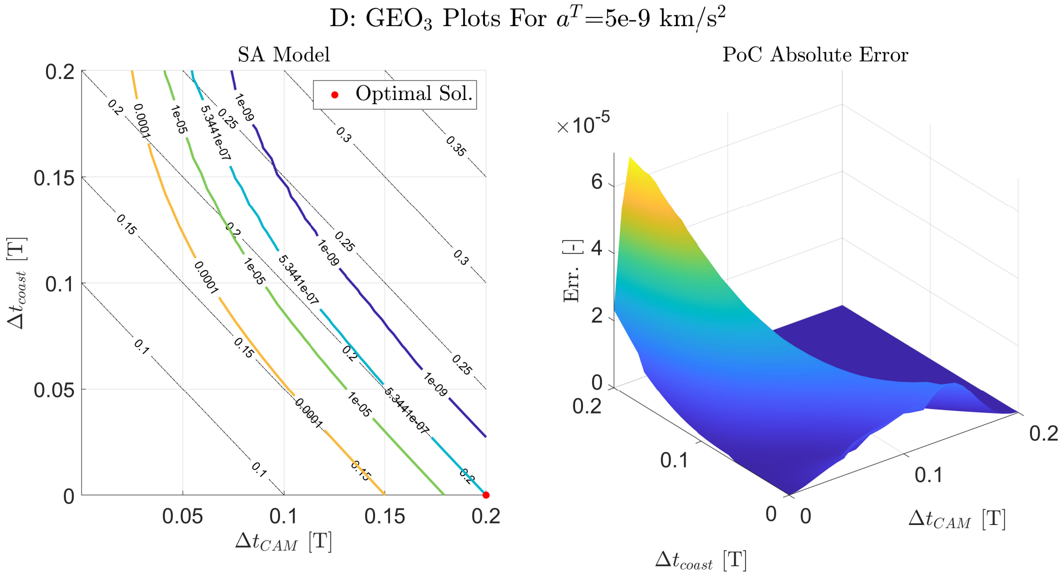

Figure 5.41: CASE D: GEO$_3$ solution for a^T=5×10^{-9} km/s^2.

Solution Analysis

The final results are reported in Table 5.22; the global optimal solution is reached for a thrust acceleration of 5e-9 km/s^2 and as for the LEO case, also in GEO the sub-optimal solution is reached by maximising the powered arc.

a^T [$\frac{km}{s^2}$]	PoC [-]	Δt_{CAM} [T]	Δt_{coast} [T]	Δt [T]	Δv [$\frac{cm}{s}$]	t^{an}_{CPU} [s]	t^{num}_{CPU} [s]
1e-9	2.51e-4	0.2000	0.0000	0.2000	1.7233	49.26	61.31
2e-9	1.07e-4	0.2000	0.0000	0.2000	3.4467	49.58	61.54
3e-9	2.87e-5	0.2000	0.0000	0.2000	5.1700	49.33	61.83
4e-9	4.91e-6	0.2000	0.0000	0.2000	6.8933	50.56	64.23
5e-9	5.34e-7	0.2000	0.0000	0.2000	8.6167	49.99	61.14

Table 5.22: Case D: GEO$_3$ results for different a^T.

The results are lastly summarized as follows:

- The CAM starts on **November 9th 2023** at **5:03 p.m.(GMT)**;
- An acceleration of **5e-9 km/s^2** aligned with the tangential direction is adopted;
- The powered leg lasts approximately **4 h 47 min** (17220 s);
- There is no coasting leg;

- The total time of the manoeuvre (powered+coasting) is about **4 h 47 min**;
- The cost of the manoeuvre is **8.6167 cm/s**;
- The final PoC, reached through the manoeuvre, is about **5.34e-7**;
- To solve the 50x50x5 grid and compute the solution the **SA** propagator takes **248.72 s** whereas the **numerical** takes **310.05 s**;

Here for GEO_3, the difference in computational time between the SA and numerical methods is the lowest and the saving is reduced to only one minute; this is mainly due to the low propagation times adopted for Δt_{CAM} and Δt_{coast} which reduce the cost of the numerical model.
Lastly, by testing the accuracy, Table 5.23 shows an error of **1.54e-7** on the final PoC, which is a good error but considering the very low saving in time with respect to the numerical model, the SA model is not as convenient.

	PoC [-]	Δt_{CAM} **[T]**	Δt_{coast} **[T]**	Δv **[$\frac{cm}{s}$]**	t_{CPU} **[s]**
SA	5.34e-7	0.2000	0.0000	0.2000	49.99
NUM	6.89e-7	0.2000	0.0000	0.2000	61.14

Table 5.23: Case D: GEO_3 results from numerical and SA models for a^T=5e-9 km/s^2.

5.7. Cost Breakdown Analysis

From the previous sections, different test cases were analyzed for both LEO and GEO, Table 5.24 summarizes the different computational times to solve the 50x50x5 grid using the SA or the numerical models.

Case	t_{CPU}^{LEO} **[s]**		t_{CPU}^{GEO} **[s]**	
	SA	**NUM**	**SA**	**NUM**
A	192.92	4953.66	258.73	451.27
B	201.32	15893.81	269.13	637.74
C	195.97	5155.86	258.10	425.16
D	204.89	2538.01	248.72	310.05

Table 5.24: Comparison of CPU times.

As already observed, the difference in computational time between SA and numerical is

very large in LEO, whereas on GEO the difference is not that relevant; the reason behind this is to research in the temporal evolution of the perturbed Keplerian elements.
LEOs are very close to Earth and so orbital perturbations, such as J_2 and drag, are very strong reaching magnitude from 1e-7 to 1e-5 km/s^2, considering also that the typical duration of a LEO low thrust CAM is larger than a period, then the short periodic oscillations in the evolution of KE increase either in magnitude and frequency.
The frequency of oscillations due to J_2 effect is calculated as 1/T (where T is the orbital period); since in LEO the orbital period is small, the frequency is much higher than in other regions; considering also that the manoeuvring times Δt_{CAM} in LEO are much larger than an orbital period then the number of oscillations increases.
As the number of oscillations gets higher and higher, also the numerical integration time increases especially when very stringent tolerances are used to retrieve the solution (remind that in the cases analyzed until now the numerical solution was retrieved through *ode45* of *MATLAB* using a *reltol* and an *abstol* of 1e-12 for both); this explains why the CPU times to get the numerical solution on LEO are so large and different from those obtained through the SA model; to better understand this phenomenon, Fig. 5.42 shows the evolution of KE on ISS orbit when this one is subject to atmospheric drag and J_2 effects.
The propagation time has been set to five periods (typical duration for a LT-CAM) and it can be noticed how the frequency and amplitude of the oscillations are very high on all of the elements: the former is due to the fact that the manoeuvring time Δt_{CAM} is much larger than the characteristic orbital period T whereas the latter is due to the magnitude of the perturbations.
For what concerns GEOs, these orbits are very far from Earth and the main orbital perturbations, such as J_2, SRP and luni-solar, reach magnitudes that go from 1e-10 to 1e-8 km/s^2 which are very weak compared to the magnitudes on LEO, in this way the amplitude of oscillations is very small
The frequency of oscillations for J_2 on GEO is much lower than in LEO ($T_{LEO}<T_{GEO}$), moreover the manoeuvring time Δt_{CAM} on GEO are smaller than one orbital period and so the number of oscillations is much lower; so the numerical solution can be retrieved quickly also by using very low tolerances, that is why the difference in computational time between the SA and numerical models is not that relevant, although the SA one is still faster.
Fig. 5.43 shows the evolution of KE on GEO$_1$ when it is perturbed by luni-solar, J_2 and SRP effects, in this case the propagation time has been set to half of a period and it can be observed the small amount of oscillations in all elements, due to the shorter manoeuvring time with respect to the GEO orbital period.

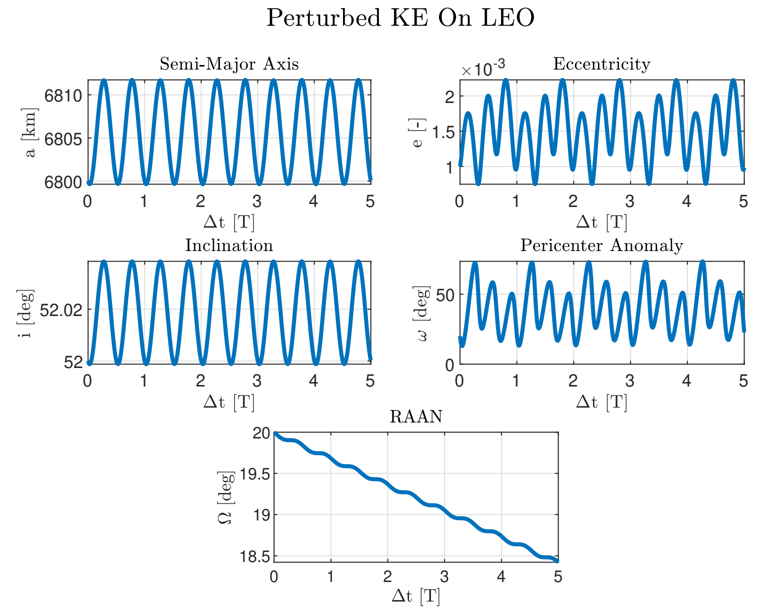

Figure 5.42: Evolution of KE on ISS.

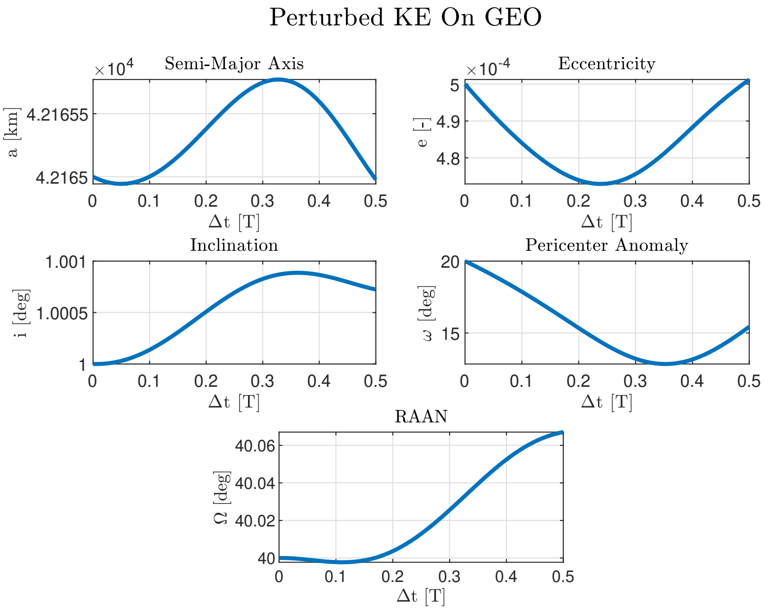

Figure 5.43: Evolution of KE on GEO_1.

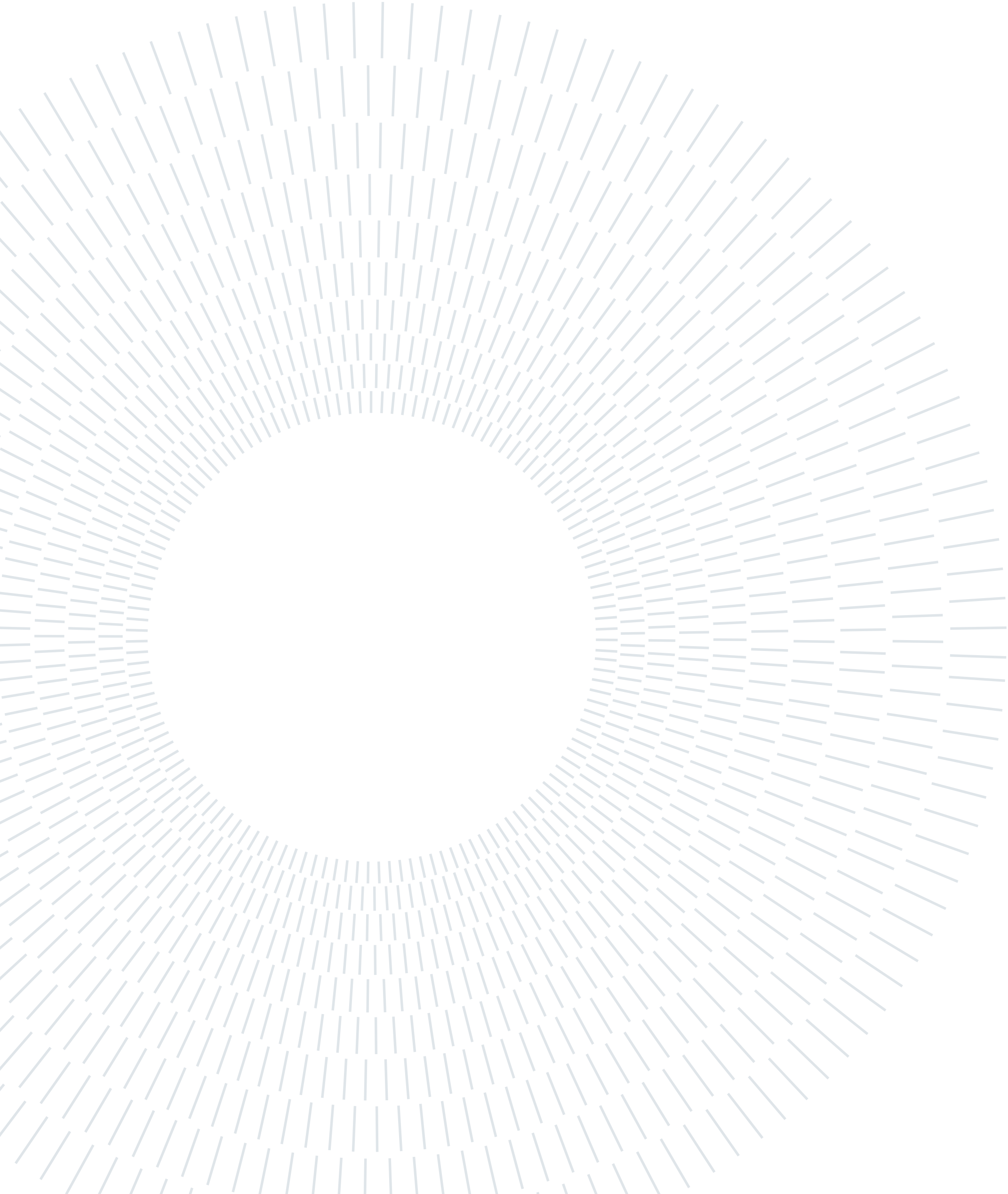

6 Conclusion

6.1. Conclusive Summary

Sometimes it may happen that CAs are detected at the last instant especially in this current scenario where space congestion is becoming a big issue; the design process must then be accomplished as soon as possible, so having lightweight and accurate algorithms for the modeling of perturbed LT-CAMs gets more and more relevant.

This thesis work was intended to provide lightweight and accurate algorithms for the design of low thrust CAMs under orbital perturbation effects.

During the project's development different perturbation models are analyzed and implemented, such as Aksnes' and King-Hele's models for the design of J_2 and atmospheric drag on LEO, and as Kozai's and Lyddane's models for the design of SRP, Sun perturbation and J_2 effect on GEO.

All of the orbital perturbation algorithms were tested for different ranges of semi-major axes, eccentricities and inclinations in order to assess their accuracy against an exact-numerical model, then all of the models were merged together in order to obtain an overall perturbed SA propagator.

Lastly, to simulate the LT action, an analytical model for the tangential and normal thrusts developed by Gonzalo et al. was integrated to complete the propagator.

To understand its advantages, the SA propagator was then tested against a numerical one for the design of perturbed LT-CAMs: different optimisation problems are analyzed and solved in order to find out the optimal solution; the optimisation process is not carried out in an analytical way but through the analysis of contour plots which are the results of a parametric analysis.

Three free variables, the coasting time, the CAM time and the thrust acceleration, are chosen to define a 3D grid of variables, each element of the grid is then used as input to the SA propagator to get the optimal solution, the same is done also with the numerical propagator in order to have a reference solution as a comparison to the accuracy and CPU cost.

The results coming out from the design process, show how fast is the SA propagator with respect to the numerical one; in LEO the computational time of the SA model to solve the grid of the parametric analysis is one or two orders of magnitude lower than the numerical one, showing also a very accurate behaviour; in GEO instead the accuracy of the SA model is still discrete and the algorithm is still faster than the numerical one but the difference is not huge.

The numerical integration in GEO takes much less time than in LEO because of the small amount of fast short-periodic oscillations in the evolution of the Keplerian elements due to the smaller ratio between manoeuvre duration and orbital period.

Summarizing, the new SA propagator is very convenient in terms of cost and accuracy on LEO whereas on GEO the game is not worth the candle especially when solving very small grids.

6.2. Future Works

This final chapter is dedicated to future works that can be done to improve the models already presented here, in particular the researches will be focused on the following points:

- **Development of a SA or analytical lunar model**: Moon perturbation in this work was modelled by integrating numerically the Gaussian equation, this is the only numerical model present within the GEO's SA propagator since all of the other perturbations are modelled in a fully analytical way; next works will be focused on the modeling of a SA or AN model in order to further decrease the computational time of the GEO propagator and get a difference in CPU time between the SA and numerical models of at least one order of magnitude;

- **Inclusion of HEO and MEO**: the models developed until now are valid only for LEO and GEO, next works will focus on expanding the perturbation models to also include Medium Earth Orbits (MEO) and High Eccentric Orbits (HEO); for MEO the perturbations that can be taken into account are the same of GEO, however all of the models must be revised since the magnitude of the perturbations is much different; for HEO instead a completely new method must be adopted since the models developed until now are not valid for high eccentricities;

- **Development of a optimisation algorithm**: in the design process the optimal solution is retrieved through a grid search by analyzing different contour plots.
  The goal is to obtain an algorithm, maybe based on genetic and gradient-based algorithms or particle swarm optimisation, to directly search for the optimal solution when the grid search is not required.

Bibliography

[1] M. Akella and K. Alfriend. Probability of collision between space objects. *Journal of Guidance, Control and Dynamics*, 23(5):769–772, 2000.

[2] K. Aksnes. A second-order artificial satellite theory based on an intermediate orbit. *JPL technical report*, 1970.

[3] K. Aksnes. Short-period and long-period perturbations of a spherical satellite due to direct solar radiation. *Celestial Mechanics*, 13:89–104, 1975.

[4] S. Alfano. A numerical implementation of spherical object collision probability. *The journal of Astronautical Sciences*, 53(1):103–109, 2005.

[5] J. H. Ayuso. Collision avoidance maneuvre optimization, a fast and accurate semi-analytical approach. Master's thesis, Universidad Politécnica de Madrid, 2014.

[6] C. Bombardelli. Analytical formulation of impulsive collision avoidance dynamics. *Celestial Mechanics and Dynamical Astronomy*, 118(2):99–114, 2013.

[7] C. Bombardelli and J. H. Ayuso. Optimal impulsive collision avoidance in LEO. *Journal Of Guidance, Control and Dynamics*, 2015.

[8] C. Bombardelli, J. Hernando-Ayuso, and R. Garcia-Pelayo. Collision avoidance maneuvre optimization. *Advances in Astronautical Sciences*, 2014.

[9] V. Braun, T. Flohrer, S. Lemmens, H. Krag, B. Bastida-Virgili, K. Merz, and Q. Funke. Operational support to collision avoidance activities by esa's space debris office. *CEAS Space J*, pages 177–189, 2016.

[10] D. Brouwer. Solution of the problem of artificial satellite theory without drag. *The Astronomical Journal*, 64(1274):378–396, 1959.

[11] F. Chan Kenneth. *Spacecraft Collision Probability.* Aerospace Corp, 2008.

[12] C. Colombo. Long-term evolution of highly ellptical orbits:luni-solar perturbation effects for stability and re-entry. *Frontiers in Astronomy and Space Sciences*, 2019. doi: 10.3389/fspas.2019.00034.

[13] C. Colombo, M. Vasile, and G. Radice. Semi-analytical solution for the optimal low-thrust deflection of NEO. *Journal of Guidance, Control and Dynamics*, 2009.

[14] H. D. Curtis. *Orbital mechanics for engineering students.* Elsevier, 2021.

[15] T. Flohrer, H. Klinkrad, H. Krag, B. Bastida-Virgili, and K. Merz. Operational collision avoidance for LEO satellites at ESA. *28th International Symposium on Space Technology and Science*, 2015.

[16] J. Foster and H. S. Estes. Parametric analysis of orbital debris collision probability and maneuver rate for space vehicles. *NASA JSC-25898*, 1992.

[17] S. Frey, C. Colombo, and S. Lemmens. Extension of King-Hele orbit contraction method for accurate,semi-analytical propagation of non-circular orbits. *Advances in Space Research*, 2019.

[18] R. Garcia-Pelayo and J. Hernando-Ayuso. Series for collision probability in short-encounter model. *Journal of Guidance, Control and Dynamics*, 39(8):1908–1916, 2016. doi: 10.2514/1-G001754.

[19] G. E. O. Giacaglia. Lunar perturbations of artificial satellites of the earth. *Smithsonian Astrophysical Observatory*, pages 239–268, 1973.

[20] J. L. Gonzalo, C. Colombo, and P. Di Lizia. A semi-analytical approach to low-thrust collision avoidance manouvre design. *70th International Astronautical Congress*, 2019.

[21] J. L. Gonzalo, C. Colombo, and P. Di Lizia. Introducing MISS, a new tool for collision avoidance analysis and design. *Journal of Space Safety Engineering*, 2020.

[22] J. L. Gonzalo, C. Colombo, and P. Di Lizia. Computationally efficient approaches for low-thrust collision avoidance activities. *72nd International Astronautical Congress*, 2021.

[23] J. L. Gonzalo, C. Colombo, and P. Di Lizia. Lightweight algorithms for collision avoidance application. *11th ESA GNC*, 2021.

[24] J. L. Gonzalo, C. Colombo, and P. Di Lizia. Analytical framework for space debris collision avoidance manouvre. *Journal Of Guidance, Control and Dynamics*, 2021.

[25] J. L. Gonzalo, C. Colombo, and P. Di Lizia. Single-averaged models for low-thrust collision avoidance under uncertainties. *73rd International Astronautical Congress*, 2022.

[26] D. Hele-King. *Theory of satellite orbits in an atmosphere.* Butterworths, 1964.

[27] J. Hernando-Ayuso. OCCAM: optimal computation of collision avoidance manouvres. 2016.

[28] IADC. IADC space debris mitigation guidelines. Vienna, 2003.

[29] B. Kaufman and D. R. Higher order theory for long-term behaviour of earth and lunar orbiters. *Naval Research Laboratory*, 1972.

[30] H. Kinoshita. Third-order solution of an artificial-satellite theory. *Dynamics of Planets and Satellites and Theories of Their Motion*, pages 241–257, 1977.

[31] Y. Kozai. Effects of solar-radiation-pressure on the motion of an artificial satellite. *NASA Astrophysics Data System*, 6:109–112, 1961.

[32] Y. Kozai. Second-order solution of artificial satellite theory without air drag. *The Astronomical Journal*, 67(7):446–462, 1962.

[33] Y. Kozai. A new method to compute lunisolar perturbations in satellite motions. *Smithsonian Astrophysical Observatory*, 1973.

[34] M. T. Lane. On analytical modeling of lunar perturbations of artificial satellites of the earth. *Celestial Mechanics and Dynamical Astronomy*, pages 287–305, 1989.

[35] R. H. Lyddane. Small eccentricities or inclinations in the Brouwer theory of the artificial satellite. *The Astronomical Journal*, 68(8):555–559, 1963.

[36] O. Montenbruck and G. Eberhard. *Satellite orbits: Models, Methods and Applications*. Springer, 2012.

[37] P. Musen, A. Bailie, and E. Upton. Development of the lunar and solar perturbations in the motion of an artificial satellite. *NASA Technical Report*, 1961.

[38] R. P. Patera. General method for calculating satellite collision probability. *Journal of Guidance, Control and Dynamics*, 24(4):716–722, 2001.

[39] J. M. Picone, A. E. Hedin, D. P. Drob, and A. C. Aikin. Nrlmsise-00 empirical model of the atmosphere: Statistical comparisons and scientific issues. *Journal of Geophysical Research: Space Physics*, 2002.

[40] A. Schiavo. A numerically efficient design of low-thrust collision avoidance manouvres. Master's thesis, Politecnico di Milano, 2020.

[41] R. Serra, D. Arzelier, M. Joldes, B. Lasserre, A. Rondepierre, and B. Salvy. Fast and accurate computation of orbital collision probability for short-term encounters. *Journal of Guidance, Control and Dynamics*, 2016. doi: 10.2514/1.G001353.

[42] D. A. Vallado. *Fundamental of astrodynamics and applications.* Springer, 2007.

[43] J. R. Wertz. *Spacecraft Attitude Determination and Control.* Kluwer Academic, 1978.

A | Appendix A

A.1. Gonzalo's Normal Thrust Time Law

The final eccentric anomaly E can be retrieved by solving the following non-linear equation:

$$\Delta t n_{ref} = E - e_{ref}\sin E + \epsilon_n \left[E K_E^n + \sum_{u=1} e_{ref}^{u-1} \sum_{v=1}^{u} \boldsymbol{N}_{uv}^E \sin vE \right] \Big|_{E_0}^{E} \tag{A.1}$$

where the expressions for the parameters K_E^n and $\boldsymbol{N}^E$ are computed as:

$$\begin{aligned} K_E^n = & \frac{2\gamma}{3\pi a_{ref} e_{ref}^2 n^2} \left((11 + 2e_{ref}^2)\mathrm{E}[e_{ref}^2] - (11 + e_{ref}^2)\mathrm{F}[e_{ref}^2] \right) + \\ & - \frac{e_{ref}}{2} - \frac{3e_{ref}^3}{16} - \frac{7e_{ref}^5}{128} - \frac{55e_{ref}^7}{2048} \end{aligned} \tag{A.2}$$

$$\boldsymbol{N}^E = \frac{\gamma}{a_{ref} e_{ref} n^2} \boldsymbol{N}_1 + \boldsymbol{N}_2 \tag{A.3}$$

F[...] and E[...] are the complete elliptic integral of first and second kind respectively, γ and the matrices N_1 and N_2 are instead computed as:

$$\gamma = \sqrt{1 - e_{ref}^2} \tag{A.4}$$

$$\boldsymbol{N_1} = \begin{bmatrix} \frac{7}{4} & 0 & 0 & 0 & 0 & 0 & 0 \\ 0 & -\frac{5}{6} & 0 & 0 & 0 & 0 & 0 \\ \frac{81}{32} & 0 & \frac{19}{96} & 0 & 0 & 0 & 0 \\ 0 & -\frac{29}{48} & 0 & -\frac{13}{192} & 0 & 0 & 0 \\ \frac{297}{256} & 0 & \frac{91}{512} & 0 & \frac{9}{512} & 0 & 0 \\ 0 & -\frac{145}{348} & 0 & -\frac{113}{1536} & 0 & -\frac{1}{128} & 0 \\ \frac{3205}{4096} & 0 & \frac{617}{4096} & 0 & \frac{569}{20480} & 0 & \frac{71}{28672} \\ 0 & -\frac{1757}{6144} & 0 & -\frac{217}{3072} & 0 & -\frac{27}{2048} & 0 \end{bmatrix} \tag{A.5}$$

$$\boldsymbol{N_2} = \begin{bmatrix} -2+\frac{3}{4}\pi & 0 & 0 & 0 & 0 & 0 & 0 \\ 0 & -\frac{1}{4} & 0 & 0 & 0 & 0 & 0 \\ \frac{3}{4} & 0 & \frac{1}{12} & 0 & 0 & 0 & 0 \\ 0 & -\frac{1}{8} & 0 & -\frac{1}{64} & 0 & 0 & 0 \\ \frac{5}{32} & 0 & \frac{5}{192} & 0 & \frac{1}{320} & 0 & 0 \\ 0 & -\frac{21}{512} & 0 & -\frac{21}{2560} & 0 & -\frac{7}{7680} & 0 \\ \frac{35}{512} & 0 & \frac{7}{512} & 0 & \frac{7}{2560} & 0 & \frac{1}{3584} \\ 0 & -\frac{11}{512} & 0 & -\frac{11}{2048} & 0 & -\frac{11}{10752} & 0 \end{bmatrix} \tag{A.6}$$

Once the non-linear equation is solved, the value of E is used to compute the final values for eccentricity and pericenter anomaly using the expressions presented in [25] and in Section 1.3.2.

B

Appendix B

In this appendix are reported the secular and short periodic components needed to for the modeling of J_2 according to Lyddane's model.
These expressions are the same presented in Brouwer's theory [10] (Lyddane use Brouwer's expressions but integrate them in a different way using Eq. (4.6)).

B.1. Brouwer's Secular Terms

J_2 perturbation has secular effects on pericenter anomaly, RAAN and mean anomaly; below are presented the expression of their secular rate of change developed up to the second order:

$$\begin{aligned}\dot{M}_{sec} =& n\Big\{1 + \frac{3}{2}\gamma_2\eta_2(-1+3\chi^2) + \frac{3}{32}\gamma_2^2\eta_2\Big[-15 + 16\eta_2 + 25\eta_2^2 + (30 + \\ &- 96\eta_2 - 90\eta_2^2)\chi^2 + (105 + 144\eta_2 + 25\eta_2^2)\chi^4\Big]\Big\}\end{aligned} \tag{B.1}$$

$$\begin{aligned}\dot{\omega}_{sec} =& n\Big\{\frac{3}{2}\gamma_2(-1+5\chi^2) + \frac{3}{32}\gamma_2^2\Big[-35 + 24\eta_2 + 25\eta_2^2 + (90 - 192\eta_2 + \\ &- 126\eta_2^2)\chi^2 + (385 + 360\eta_2 + 45\eta_2^2)\chi^4\Big]\Big\}\end{aligned} \tag{B.2}$$

$$\dot{\Omega}_{sec} = n\Big\{-3\gamma_2\chi + \frac{3}{8}\gamma_2^2\Big[(-5 + 12\eta_2 + 9\eta_2^2)\chi + (-35 - 36\eta_2 - 5\eta_2^2)\chi^3\Big]\Big\} \tag{B.3}$$

where the terms γ_2, χ, η and n are computed as:

$$\gamma_2 = \frac{J_2}{2}\left[\frac{R_e}{\bar{a}(1-\bar{e}^2)}\right]^2 \tag{B.4}$$

$$\chi = \cos\bar{i} \tag{B.5}$$

$$\eta_2 = \sqrt{1-\bar{e}^2} \tag{B.6}$$

$$n = \sqrt{\frac{\mu}{\bar{a}^3}} \tag{B.7}$$

B.2. Brouwer's Short-Periodic Terms

Short-periodic oscillations are present in all of the KE and their expressions are developed up to the first order as follows:

$$\delta a = \bar{a}\tilde{\gamma}_2\left[(-1+3\chi^2)\left(\frac{\bar{a}^3}{r^3}-\eta_2^{-3}\right)+3(1-\chi^2)\frac{\bar{a}^3}{r^3}\cos(2\overline{\varpi}+2\bar{\theta})\right] \tag{B.8}$$

$$\begin{aligned}\delta e =& \frac{\eta_2^2}{2\bar{e}}\left\{\tilde{\gamma}_2\left[(-1+3\chi^2)\left(\frac{\bar{a}^3}{r^3}-\eta_2^{-3}\right)+3(1-\chi^2)\left(\frac{\bar{a}^3}{r^3}-\eta_2^{-4}\right)\cos(2\overline{\varpi}+\right.\right.\\ &\left.\left.+2\bar{\theta})\right]-\gamma_2(1-\chi^2)[3\bar{e}\cos(2\overline{\varpi}+\bar{\theta})+\bar{e}\cos(2\overline{\varpi}+3\bar{\theta}]\right\}\end{aligned} \tag{B.9}$$

$$\delta i = \frac{1}{2}\gamma_2\chi\sqrt{1-\chi^2}[3\cos(2\overline{\varpi}+2\bar{\theta})+3\bar{e}\cos(2\overline{\varpi}+\bar{\theta})+\bar{e}\cos(2\overline{\varpi}+3\bar{\theta})] \tag{B.10}$$

$$\begin{aligned}\delta M =& -\frac{\eta_2^3}{4\bar{e}}\gamma_2\left\{2(-1+3\chi^2)\left(\frac{\bar{a}^2}{r^2}\eta_2^2+\frac{\bar{a}}{r}+1\right)\sin\bar{\theta}+3(1-\chi^2)\left[\left(-\frac{\bar{a}^2}{r^2}\eta_2^2+\right.\right.\right.\\ &\left.\left.\left.-\frac{\bar{a}}{r}+1\right)\sin(2\overline{\varpi}+\bar{\theta})+\left(\frac{\bar{a}^2}{r^2}\eta_2^2+\frac{\bar{a}}{r}+\frac{1}{3}\right)\sin(2\overline{\varpi}+3\bar{\theta})\right]\right\}\end{aligned} \tag{B.11}$$

$$\begin{aligned}\delta\omega =& \frac{\eta_2^2}{4\bar{e}}\gamma_2\left\{2(-1+3\chi^2)\left(\frac{\bar{a}^2}{r^2}\eta_2^2+\frac{\bar{a}}{r}+1\right)\sin\bar{\theta}+3(1-\chi^2)\left[\left(-\frac{\bar{a}^2}{r^2}\eta_2^2+\right.\right.\right.\\ &\left.\left.\left.-\frac{\bar{a}}{r}+1\right)\sin(2\overline{\varpi}+\bar{\theta})+\left(\frac{\bar{a}^2}{r^2}\eta_2^2+\frac{\bar{a}}{r}+\frac{1}{3}\right)\sin(2\overline{\varpi}+3\bar{\theta})\right]\right\}+\\ &+\frac{1}{4}\gamma_2\{6(-1+5\chi^2)(\bar{\theta}-\overline{M}+\bar{e}\sin\bar{\theta})+(3-5\chi^2)[3\sin(2\overline{\varpi}+2\bar{\theta})+\\ &+3\bar{e}\sin(2\overline{\varpi}+\bar{\theta})+\bar{e}\sin(2\overline{\varpi}+3\bar{\theta})]\}\end{aligned} \tag{B.12}$$

$$\begin{aligned}\delta\Omega =& -\frac{1}{2}\gamma_2\chi[6(\bar{\theta}-\overline{M}+\bar{e}\sin\bar{\theta})-3\sin(2\overline{\varpi}+2\bar{\theta})-3\bar{e}\sin(2\overline{\varpi}+\bar{\theta})+\\ &-\bar{e}\sin(2\overline{\varpi}+3\bar{\theta})]\end{aligned} \tag{B.13}$$

in this case $\overline{\theta}$ is the 'mean' true anomaly computed using Kepler's law from the 'mean' mean anomaly $\overline{M}$, the expressions for r and $\tilde{\gamma}_2$ are instead reported below:

$$r = \frac{\overline{a}(1 - \overline{e}^2)}{1 + \overline{e}\cos\overline{\theta}} \tag{B.14}$$

$$\tilde{\gamma}_2 = \frac{J_2}{2}\left(\frac{R_e}{\overline{a}}\right)^2 \tag{B.15}$$

It is important to remind that the overlined quantities are referred to the mean elements.

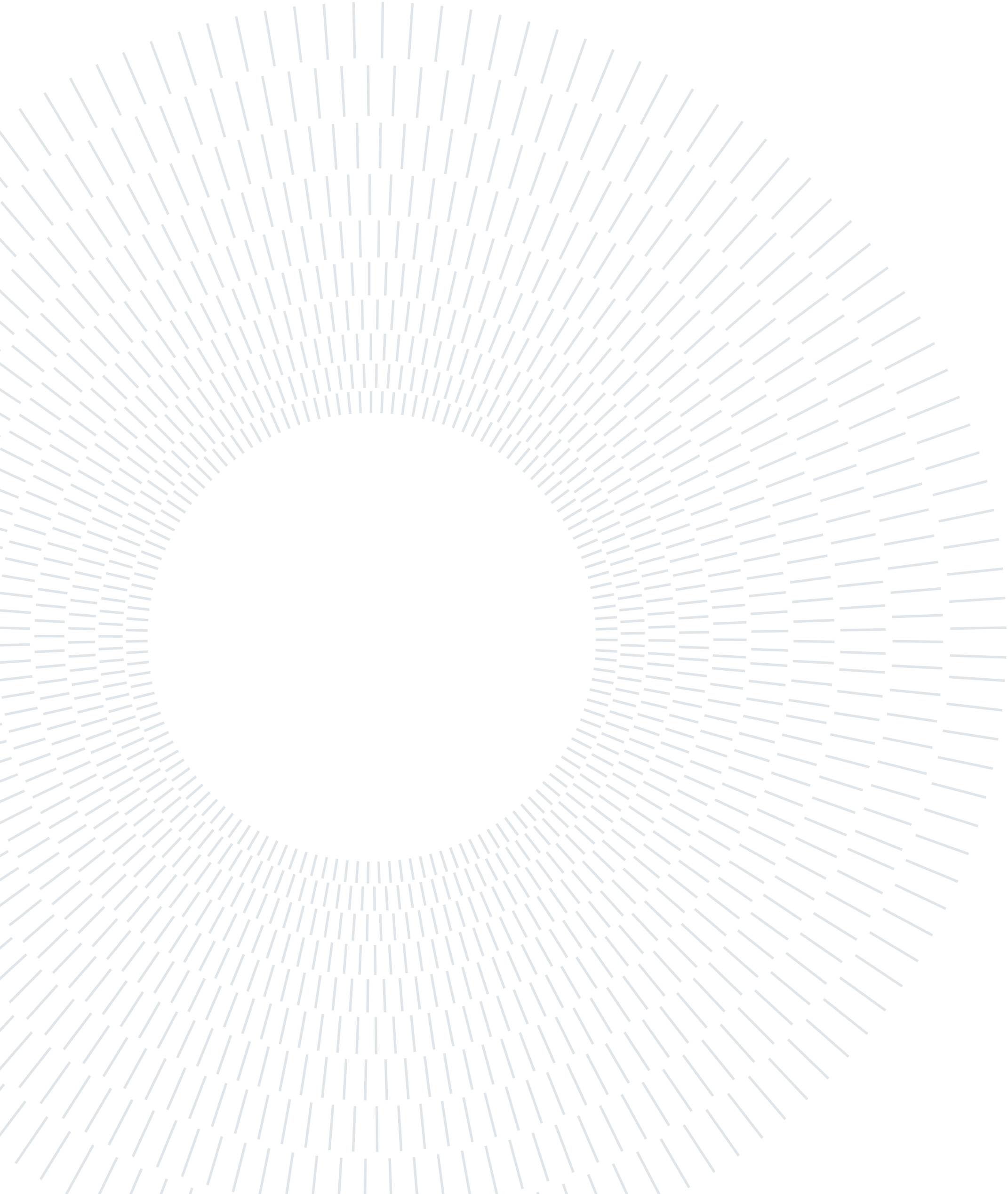

C | Appendix C

In this appendix are reported the full expressions of vector and matrices essential to model the King-Hele low and high eccentricity drag models; more information is also available in [26] and [17].

C.1. King-Hele Low Eccentricity Drag Model

To retrieve the final state of a s/c subject to the only atmospheric drag, the following ODE system must be solved through a numerical integrator:

$$\begin{cases} \frac{da}{dt} = -\frac{A}{m} C_D \sqrt{\mu a} \rho(h_p) \exp(-z) [\vec{e}^\top \boldsymbol{K}_{\boldsymbol{a}}^{\boldsymbol{l}} \vec{I}] \\ \frac{de}{dt} = -\frac{A}{m} C_D \sqrt{\frac{\mu}{a}} \rho(h_p) \exp(-z) [\vec{e}^\top \boldsymbol{K}_{\boldsymbol{e}}^{\boldsymbol{l}} \vec{I}] \\ \frac{dM}{dt} = \sqrt{\frac{\mu}{a^3}} \end{cases} \tag{C.1}$$

in this case the vectors $\vec{e}$ and $\vec{I}$ are defined as:

$$\vec{e}^\top = \begin{bmatrix} 1 & e & e^2 & e^3 & e^4 & e^5 \end{bmatrix} \tag{C.2}$$

$$\vec{I}^\top = \begin{bmatrix} I_0 & I_1 & I_2 & I_3 & I_4 & I_5 & I_6 \end{bmatrix} \tag{C.3}$$

where the generic $I_n(z)$ is the Bessel function of first kind defined as:

$$I_n(z) = \left(\frac{z}{2}\right)^n \sum_{j=0}^{\infty} \frac{(-1)^j (\frac{x}{2})^{2j}}{j! \Gamma(n + j + 1)} \tag{C.4}$$

the matrices $\mathbf{K}_a^l$ and $\mathbf{K}_e^l$ are instead defined as:

$$\boldsymbol{K_a^l} = \begin{bmatrix} 1 & 0 & 0 & 0 & 0 & 0 & 0 \\ 0 & 2 & 0 & 0 & 0 & 0 & 0 \\ \frac{3}{4} & 0 & \frac{3}{4} & 0 & 0 & 0 & 0 \\ 0 & \frac{3}{4} & 0 & \frac{1}{4} & 0 & 0 & 0 \\ \frac{21}{64} & 0 & \frac{28}{64} & 0 & \frac{7}{64} & 0 & 0 \\ 0 & \frac{30}{64} & 0 & \frac{15}{64} & 0 & \frac{3}{64} & 0 \end{bmatrix} \tag{C.5}$$

$$\boldsymbol{K_e^l} = \begin{bmatrix} 0 & 1 & 0 & 0 & 0 & 0 & 0 \\ \frac{1}{2} & 0 & \frac{1}{2} & 0 & 0 & 0 & 0 \\ 0 & -\frac{5}{8} & 0 & \frac{1}{8} & 0 & 0 & 0 \\ -\frac{5}{16} & 0 & -\frac{4}{16} & 0 & \frac{1}{16} & 0 & 0 \\ 0 & -\frac{18}{128} & 0 & -\frac{1}{128} & 0 & \frac{3}{128} & 0 \\ -\frac{18}{256} & 0 & -\frac{19}{256} & 0 & \frac{2}{256} & 0 & \frac{3}{256} \end{bmatrix} \tag{C.6}$$

C.2. King-Hele High Eccentricity Drag Model

Similarly to the previous section, to retrieve the final state of a s/c subject to the only atmospheric drag, the following ODE system must be solved through a numerical integrator:

$$\begin{cases} \frac{da}{dt} = -\frac{A}{m} C_D \sqrt{\mu a} \rho(h_p) \sqrt{\frac{2(1+e)}{\pi z(1-e)}} (1+e) [\vec{e}^\top \boldsymbol{K_a^h} \vec{r}] \\ \frac{de}{dt} = -\frac{A}{m} C_D \sqrt{\frac{\mu}{a}} \rho(h_p) \sqrt{\frac{2(1+e)}{\pi z(1-e)}} (1-e^2) [\vec{e}^\top \boldsymbol{K_e^h} \vec{r}] \\ \frac{dM}{dt} = \sqrt{\frac{\mu}{a^3}} \end{cases} \tag{C.7}$$

the vectors $\vec{e}$ and $\vec{r}$ are defined as:

$$\vec{e}^\top = \begin{bmatrix} 1 & e & e^2 & e^3 & e^4 & e^5 & e^6 & e^7 & e^8 & e^9 \end{bmatrix} \tag{C.8}$$

$$\vec{r}^\top = \begin{bmatrix} 1 & \lambda & \lambda^2 & \lambda^3 & \lambda^4 & \lambda^5 \end{bmatrix} \tag{C.9}$$

where λ is computed as:

$$\lambda = \frac{1}{z(1-e^2)} \tag{C.10}$$

the matrices $\mathbf{K}_a^h$ and $\mathbf{K}_e^h$ are instead defined as:

$$\boldsymbol{K_a^h} = \begin{bmatrix} \frac{1}{2} & \frac{1}{16} & \frac{9}{256} & \frac{75}{2048} & \frac{3675}{65536} & \frac{59535}{524288} \\ 0 & -\frac{1}{2} & -\frac{3}{16} & -\frac{45}{256} & -\frac{525}{2048} & -\frac{33075}{65536} \\ 0 & \frac{3}{16} & \frac{75}{128} & \frac{675}{2048} & \frac{5985}{16384} & \frac{288225}{524288} \\ 0 & 0 & \frac{3}{16} & -\frac{75}{128} & -\frac{105}{2048} & \frac{10395}{16384} \\ 0 & 0 & -\frac{15}{256} & -\frac{3735}{2048} & \frac{21945}{32768} & -\frac{344925}{262144} \\ 0 & 0 & 0 & -\frac{45}{256} & \frac{13545}{2048} & -\frac{129465}{32768} \\ 0 & 0 & 0 & \frac{105}{2048} & \frac{110985}{16384} & -\frac{7687575}{262144} \\ 0 & 0 & 0 & 0 & \frac{525}{2048} & -\frac{836325}{16384} \\ 0 & 0 & 0 & 0 & -\frac{4725}{65536} & -\frac{16288965}{524288} \\ 0 & 0 & 0 & 0 & 0 & -\frac{33075}{65536} \end{bmatrix} \tag{C.11}$$

$$\boldsymbol{K_e^h} = \begin{bmatrix} \frac{1}{2} & -\frac{3}{16} & -\frac{15}{256} & -\frac{105}{2048} & -\frac{4725}{65536} & -\frac{72765}{524288} \\ 0 & -\frac{1}{4} & \frac{9}{32} & \frac{75}{512} & \frac{735}{4096} & \frac{42525}{131072} \\ 0 & \frac{3}{16} & \frac{39}{128} & -\frac{405}{2048} & \frac{525}{16384} & \frac{152145}{524288} \\ 0 & 0 & \frac{3}{32} & -\frac{375}{256} & \frac{735}{4096} & -\frac{31185}{32768} \\ 0 & 0 & -\frac{15}{256} & -\frac{1515}{2048} & \frac{123585}{32768} & -\frac{530145}{262144} \\ 0 & 0 & 0 & -\frac{45}{512} & \frac{31605}{4096} & -\frac{1165185}{65536} \\ 0 & 0 & 0 & \frac{105}{2048} & \frac{40845}{16384} & -\frac{10235295}{262144} \\ 0 & 0 & 0 & 0 & \frac{525}{4096} & -\frac{1505385}{32768} \\ 0 & 0 & 0 & 0 & -\frac{4725}{65536} & -\frac{5716305}{524288} \\ 0 & 0 & 0 & 0 & 0 & -\frac{33075}{131072} \end{bmatrix} \tag{C.12}$$

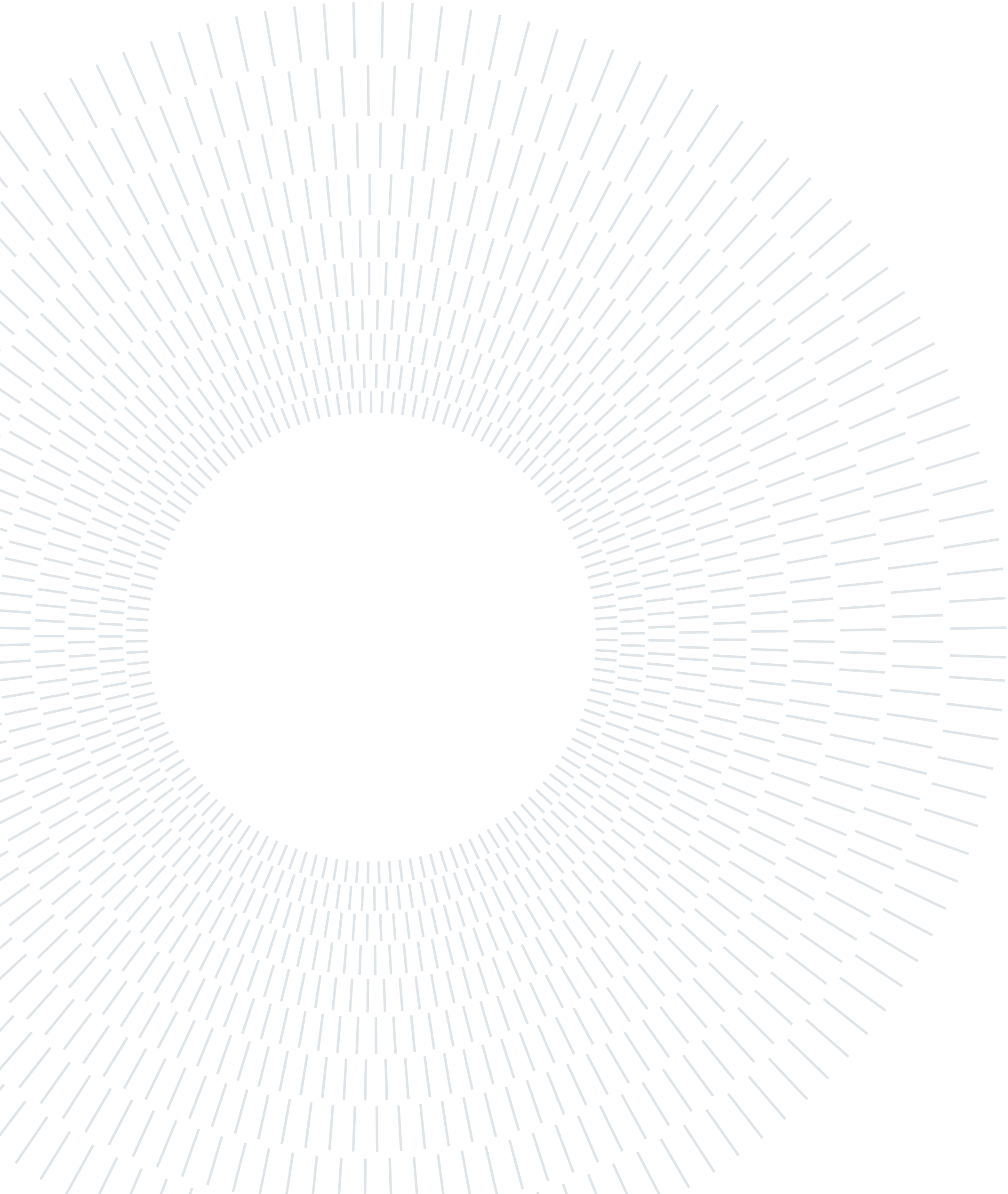

D | Appendix D

D.1. Kozai's SRP Model

In this appendix are reported the expressions of the short-periodic variations $\delta\alpha$ on Keplerian elements subject to SRP perturbation, these expressions show some corrections with respect to those exposed in [31].

$$\delta a = 2a^3 \frac{P_{SR}}{\mu} \Big| R\cos E + S\sqrt{1-e^2}\sin E \Big|_{E_0}^{E_f} \tag{D.1}$$

$$\delta e = a^2 \frac{P_{SR}}{\mu}\sqrt{1-e^2}\Big| \frac{1}{4}R\sqrt{1-e^2}\cos 2E + S\left(\frac{3}{2}E - 2e\sin E + \frac{1}{4}\sin 2E\right)\Big|_{E_0}^{E_f} \tag{D.2}$$

$$\begin{aligned}\delta i =& a^2\frac{P_{SR}}{\mu}W\frac{1}{\sqrt{1-e^2}}\Big|\left[-\frac{3}{2}eE + (1+e^2)\sin E - \frac{e}{4}\sin 2E\right]\cos\omega + \\ &+ \sqrt{1-e^2}\left(\cos E - \frac{e}{4}\cos 2E\right)\sin\omega\Big|_{E_0}^{E_f}\end{aligned} \tag{D.3}$$

$$\begin{aligned}\sin i\delta\Omega =& a^2\frac{P_{SR}}{\mu}W\frac{1}{\sqrt{1-e^2}}\Big|\left[-\frac{3}{2}eE + (1+e^2)\sin E - \frac{e}{4}\sin 2E\right]\sin\omega + \\ &- \sqrt{1-e^2}\left(\cos E - \frac{e}{4}\cos 2E\right)\cos\omega\Big|_{E_0}^{E_f}\end{aligned} \tag{D.4}$$

$$\begin{aligned}\delta\omega + \cos i\delta\Omega =& \frac{a^2P_{SR}\sqrt{1-e^2}}{\mu e}\Big|R\left(-\frac{3}{2}E + e\sin E + \frac{1}{4}\sin 2E\right) + \\ &+ S\frac{1}{\sqrt{1-e^2}}\left(e\cos E - \frac{1}{4}\cos 2E\right)\Big|_{E_0}^{E_f}\end{aligned} \tag{D.5}$$

$$
\begin{aligned}
\delta M = &- \sqrt{1-e^2}\,(\delta\omega + \cos i\delta\Omega) + \\
&- 3a^2\frac{P_{SR}}{\mu}\Bigg| R\left[-\frac{3}{2}eE + \left(\frac{5}{3}+\frac{2}{3}e^2\right)\sin E - \frac{5}{12}e\sin 2E\right] + \\
&- S\sqrt{1-e^2}\left(\frac{5}{3}\cos E - \frac{5}{12}e\cos 2E\right) + \\
&- \left[R\cos E_0 + S\sqrt{1-e^2}\sin E_0\right](E - e\sin E)\Bigg|_{E_0}^{E_f}
\end{aligned}
\tag{D.6}
$$

where R, S and W represents the direction cosines of the Earth-Sun position vector in the RSW frame evaluated at θ=0, whereas E_0 and E_f are the eccentric anomaly at the initial and final epochs.

List of Figures

1.1 Operations on collision avoidance process at ESOC (from [15]). 3
1.2 Operations on collision avoidance process at ESOC using CSM (from [15]). 4
1.3 Risk assessment for TLE-based (top) and CSM-based (bottom) data [9]. . 5
1.4 Objects encountered by ES into an ellipsoid of 10x25x10 km [15]. 6

2.1 Magnitude of orbital perturbations [36]. 20

3.1 Encounter plane between two objects [40]. 26

4.1 Error in position of Aksnes' model. 36
4.2 Error in position of Lyddane's model. 37
4.3 Error in position of KH low eccentricity model. 39
4.4 Error in position of KH high eccentricity model. 40
4.5 Error in position of SRP model. 42
4.6 Error in position of SRP model at epoch. 43
4.7 Error in position of Sun model. 45
4.8 Error in position of Sun model at epoch. 45
4.9 Error in position of LEO tangential model. 47
4.10 Error in position of GEO tangential model. 48
4.11 Position error VS displacement obtained from different ϵ_t. 48
4.12 Error in position of LEO normal model. 49
4.13 Error in position of GEO normal model. 50

5.1 Structure of the perturbed SA propagator. 54
5.2 CASE A: LEO$_1$ solution for a^T=1×10^{-9} km/s^2. 57
5.3 CASE A: LEO$_1$ solution for a^T=2×10^{-9} km/s^2. 57
5.4 CASE A: LEO$_1$ solution for a^T=3×10^{-9} km/s^2. 58
5.5 CASE A: LEO$_1$ solution for a^T=4×10^{-9} km/s^2. 58
5.6 CASE A: LEO solution for a^T=5×10^{-9} km/s^2. 59
5.7 CASE A: GEO$_1$ solution for a^T=1×10^{-9} km/s^2. 62
5.8 CASE A: GEO$_1$ solution for a^T=2×10^{-9} km/s^2. 62

5.9 CASE A: GEO_1 solution for a^T=3×10^{-9} km/s^2. 63
5.10 CASE A: GEO_1 solution for a^T=4×10^{-9} km/s^2. 63
5.11 CASE A: GEO_1 solution for a^T=5×10^{-9} km/s^2. 64
5.12 CASE B: ISS solution for a^T=1×10^{-9} km/s^2. 67
5.13 CASE B: ISS solution for a^T=2×10^{-9} km/s^2. 67
5.14 CASE B: ISS solution for a^T=3×10^{-9} km/s^2. 68
5.15 CASE B: ISS solution for a^T=4×10^{-9} km/s^2. 68
5.16 CASE B: ISS solution for a^T=5×10^{-9} km/s^2. 69
5.17 CASE B: GEO_2 solution for a^T=1×10^{-9} km/s^2. 72
5.18 CASE B: GEO_2 solution for a^T=2×10^{-9} km/s^2. 72
5.19 CASE B: GEO_2 solution for a^T=3×10^{-9} km/s^2. 73
5.20 CASE B: GEO_2 solution for a^T=3.5×10^{-9} km/s^2. 73
5.21 CASE B: GEO_2 solution for a^T=4×10^{-9} km/s^2. 74
5.22 CASE C: LEO_2 solution for a^T=1×10^{-9} km/s^2. 77
5.23 CASE C: LEO_2 solution for a^T=2×10^{-9} km/s^2. 77
5.24 CASE C: LEO_2 solution for a^T=3×10^{-9} km/s^2. 78
5.25 CASE C: LEO_2 solution for a^T=4×10^{-9} km/s^2. 78
5.26 CASE C: LEO_2 solution for a^T=5×10^{-9} km/s^2. 79
5.27 CASE C: GEO_3 solution for a^T=1×10^{-9} km/s^2. 81
5.28 CASE C: GEO_3 solution for a^T=2×10^{-9} km/s^2. 82
5.29 CASE C: GEO_3 solution for a^T=3×10^{-9} km/s^2. 82
5.30 CASE C: GEO_3 solution for a^T=4×10^{-9} km/s^2. 83
5.31 CASE C: GEO_3 solution for a^T=5×10^{-9} km/s^2. 83
5.32 CASE D: LEO_3 solution for a^T=1×10^{-9} km/s^2. 86
5.33 CASE D: LEO_3 solution for a^T=2×10^{-9} km/s^2. 86
5.34 CASE D: LEO_3 solution for a^T=3×10^{-9} km/s^2. 87
5.35 CASE D: LEO_3 solution for a^T=4×10^{-9} km/s^2. 87
5.36 CASE D: LEO_3 solution for a^T=5×10^{-9} km/s^2. 88
5.37 CASE D: GEO_3 solution for a^T=1×10^{-9} km/s^2. 90
5.38 CASE D: GEO_3 solution for a^T=2×10^{-9} km/s^2. 90
5.39 CASE D: GEO_3 solution for a^T=3×10^{-9} km/s^2. 91
5.40 CASE D: GEO_3 solution for a^T=4×10^{-9} km/s^2. 91
5.41 CASE D: GEO_3 solution for a^T=5×10^{-9} km/s^2. 92
5.42 Evolution of KE on ISS. 95
5.43 Evolution of KE on GEO_1. 95

List of Tables

4.1 Summary of perturbation models. 51

5.1 Case A: Orbital parameters of LEO_1 and debris at CA. 56
5.2 Case A: LEO_1 results for different a^T. 59
5.3 Case A: LEO_1 results from numerical and SA models for a^T=5e-9 km/s^2. . 60
5.4 Case A: Orbital parameters of GEO_1 and debris at CA. 61
5.5 Case A: GEO_1 results for different a^T. 64
5.6 Case A: GEO_1 results from numerical and SA models for a^T=5e-9 km/s^2. . 65
5.7 Case B: Orbital parameters of ISS and debris at CA. 66
5.8 Case B: ISS results for different a^T. 70
5.9 Case B: ISS results from numerical and SA models for a^T=5e-9 km/s^2. . . 71
5.10 Case B: Orbital parameters of GEO_2 and debris at CA. 71
5.11 Case B: GEO_2 results for different a^T. 75
5.12 Case B: GEO_2 results from numerical and SA models for a^T=4e-9 km/s^2. . 76
5.13 Case C: Orbital parameters of LEO_2 and debris at CA. 76
5.14 Case C: LEO_2 results for different a^T. 79
5.15 Case C: LEO_2 results from numerical and SA models for a^T=5e-9 km/s^2. . 80
5.16 Case C: Orbital parameters of GEO_3 and debris at CA. 80
5.17 Case C: GEO_3 results for different a^T. 84
5.18 Case C: GEO_3 results from numerical and SA models for a^T=5e-9 km/s^2. . 84
5.19 Case D: Orbital parameters of LEO_3 and debris at CA. 85
5.20 Case D: LEO_3 results for different a^T. 88
5.21 Case D: LEO_3 results from numerical and SA models for a^T=5e-9 km/s^2. . 89
5.22 Case D: GEO_3 results for different a^T. 92
5.23 Case D: GEO_3 results from numerical and SA models for a^T=5e-9 km/s^2. . 93
5.24 Comparison of CPU times. 93

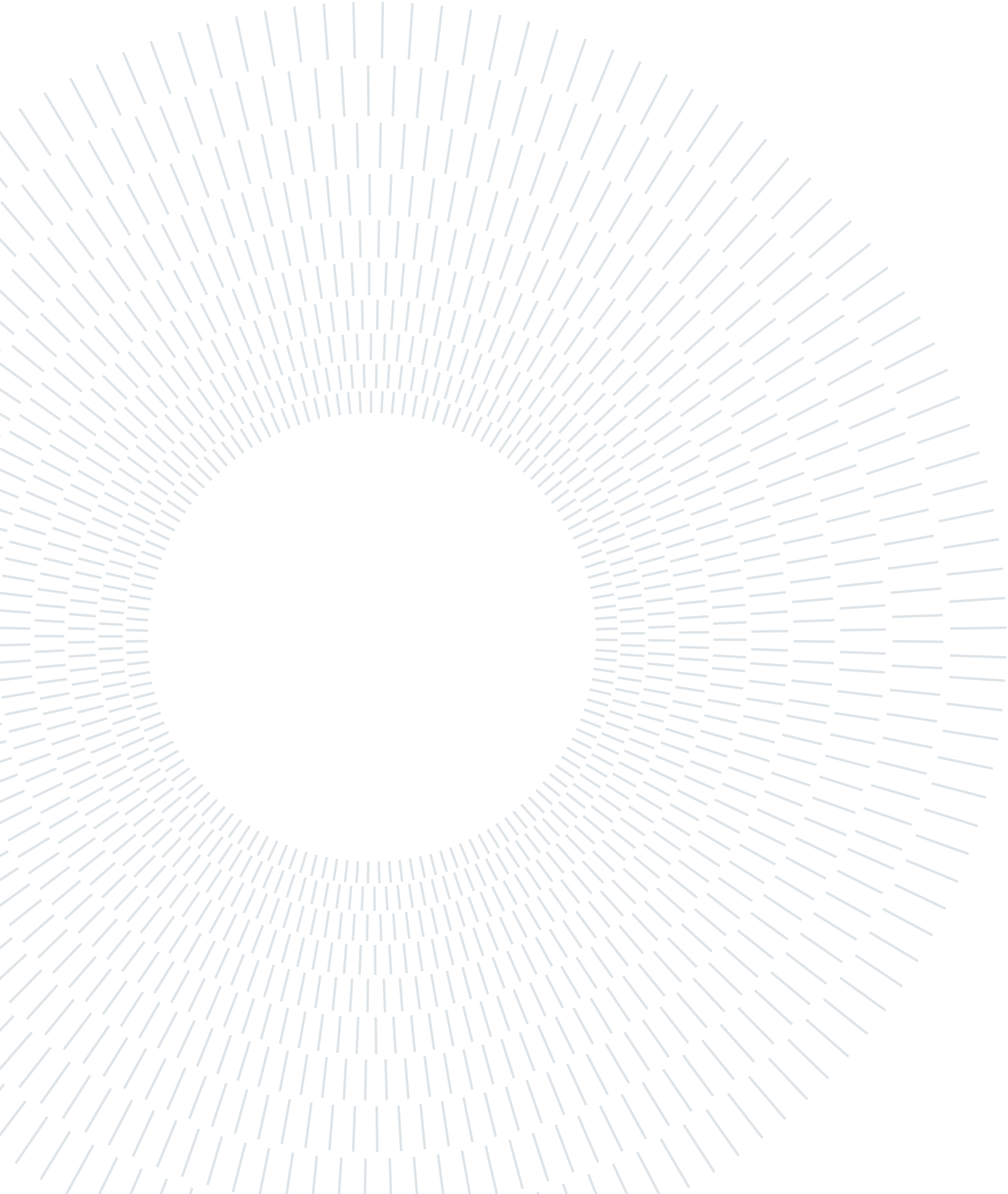

List of Acronyms

Acronym	Description
AN	ANalytical
CA	Closest Approach
CAM	Collision Avoidance Manoeuvre
CAMOS	Collision Avoidance Manoeuvre Optimisation Software
CDM	Conjuction Data Message
CORCOS	COllision Risk COmputation Software
CPU	Central Processing Unit
CRASS	Collision Risk ASsessment Software
CSM	Conjuction Summary Message
CSPOC	Combined SPace Operation Centre
DEB	DEBris
DISCOS	Database Information System Characterising Objects in Space
ES	Envisat
ESA	European Space Agency
ESOC	European Space Operation Centre
GEO	Geostationary Earth Orbit
GMT	Greenwich Mean Time
HEO	High Eccentric Orbit
HRCE	High Risk Conjuction Event
IADC	Inter-Agency space Debris coordination Committee
ISS	International Space Station
KE	Keplerian Element
KH	King-Hele
LEO	Low Earth Orbit
LT	Low Thrust

MEO	Medium Earth Orbit
MISS	Manoeuvre Intelligence for Space Safety
MJD	Modified Julian Day
NASA	National Aeronautics and Space Administration
NUM	NUMerical
OCCAM	Optimal Computation of Collision Avoidance Manoeuvre
ODE	Ordinary Differential Equation
ODIN	Orbit Determination by Improved Normal equations
PDF	Probability Density Function
PoC	Probability Of Collision
RAAN	Right Ascension of the Ascending Node
RF	Reference Frame
RTH	Radial Transversal Out-of-plane frame
SA	Semi-Analytical
S/C	SpaceCraft
SDO	Space Debris Office
SRP	Solar Radiation Pressure
SSO	Sun-Synchronous Orbit
STM	State Transition Matrix
TLE	Two Line Elements
TNH	Tangential Normal Out-of-plane frame
USSTRATCOM	United States STRATegic COMmand

List of Symbols

Variable	Description	SI unit
$P_{n,m}$	Associated Legendre function	-
ρ	Atmospheric density	kg/m^3
Δt_{CAM}	CAM time	s
Δt_{coast}	Coasting time	s
s_a	Combined radius	m
t_{CPU}	Computational time	s
ρ_{xx}	Correlation component	-
Δv	Cost of manoeuvre	m/s
$\boldsymbol{C}$	Covariance matrix	-
A	Cross section	m^2
C_D	Drag coefficient	-
ω_e	Earth angular speed	rad/s
μ	Earth gravitational parameter	m^3/s^2
R_e	Earth radius	-
E	Eccentric anomaly	rad
e	Eccentricity	-
ϵ	Ecliptic angle	rad
F[...]	Elliptic integral of first kind	-
E[...]	Elliptic integral of second kind	-
t_c	Encounter duration	s
ϵ_c	Encounter ratio	-
x_f	Final value	-
S	Flux density	kg/s^3
$J(x)$	Generic cost function	-
α_H	Generic Hill element	-

α	Generic Keplerian element	-
α_P	Generic Poincarè element	-
$J_{n,m}$	Geodesy parameter	-
$\boldsymbol{I}$	Identity matrix	-
i	Inclination	rad
x_0	Initial value	-
P_n	Legendre polynomial	-
x_{lp}	Long periodic term	-
m	Mass	kg
$\boldsymbol{A}$	Matrix notation	-
M	Mean anomaly	rad
$\overline{\alpha}$	Mean element	-
n	Mean motion	rad/s
δr	Miss distance	m
μ_{Moon}	Moon gravitational parameter	$\mathrm{m}^3/\mathrm{s}^2$
a_n	Normal acceleration	m/s^2
ϵ_n	Normal thrust parameter	-
r	Orbital radius	m
v	Orbital speed	m/s
x_{osc}	Oscillatory component	-
ω	Pericenter anomaly	rad
h_p	Perigee height	m
$\vec{p}$	Perturbation vector	m/s^2
U	Potential	$\mathrm{m}^2\mathrm{kg}/\mathrm{s}^2$
PoC	Probability of collision	-
$\boldsymbol{A}^P$	Pseudo-inverse matrix	-
Ω	RAAN	rad
$\dot{x}$	Rate of change	[...]/s
x_{ref}	Reference value	-
C_R	Reflectivity coefficient	-
H	Scale height	m
x_{sec}	Secular term	-
p	Semi-latus rectum	m

a	Semi-major axis	m
b	Semi-minor axis	m
x_{sp}	Short periodic term	-
P_{SR}	Solar radiation pressure	$\mathrm{kg/s^2m}$
c	Speed of light	m/s
σ	Standard deviation	m
μ_{Sun}	Sun gravitational parameter	$\mathrm{m^3/s^2}$
a_t	Tangential acceleration	$\mathrm{m/s^2}$
ϵ_t	Tangential thrust parameter	-
t_{CA}	Time to closest approach	s
a^T	Thrust acceleration	$\mathrm{m/s^2}$
γ_t	Thrust angle	rad
$\boldsymbol{A}^\top$	Transverse matrix	-
θ	True anomaly	rad
$\vec{a}$	Vector notation	-

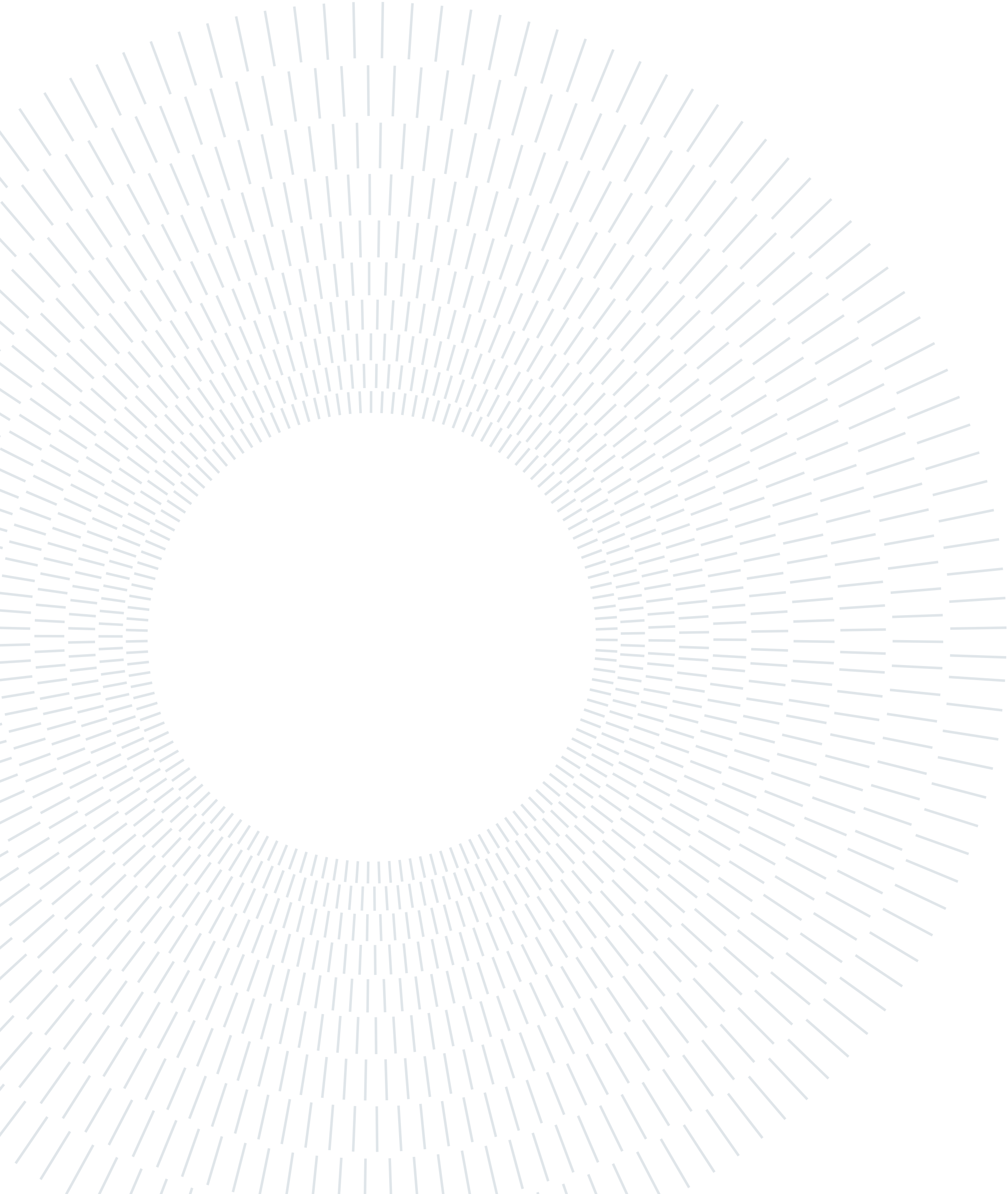

Acknowledgements

It is my duty to thank all of the people who assisted me to take on these challenging yet valuable studies and to those who have supported me until the end.

I would like to express my gratitude to my advisor Professor Juan Luis Gonzalo Gómez for always being available and keen to help me during my difficult and laborious times, thank you for sharing your knowledge with me and motivate me so that I was able to pursue this path with more pride and confidence.

In addition I wish to thank my family for constantly being there for me and especially providing me of everything I needed since the very beginning, I will be forever grateful to them for believing in my decisions and for blindly trusting me; they continuously encourage me and I know I can always count on them in the future.

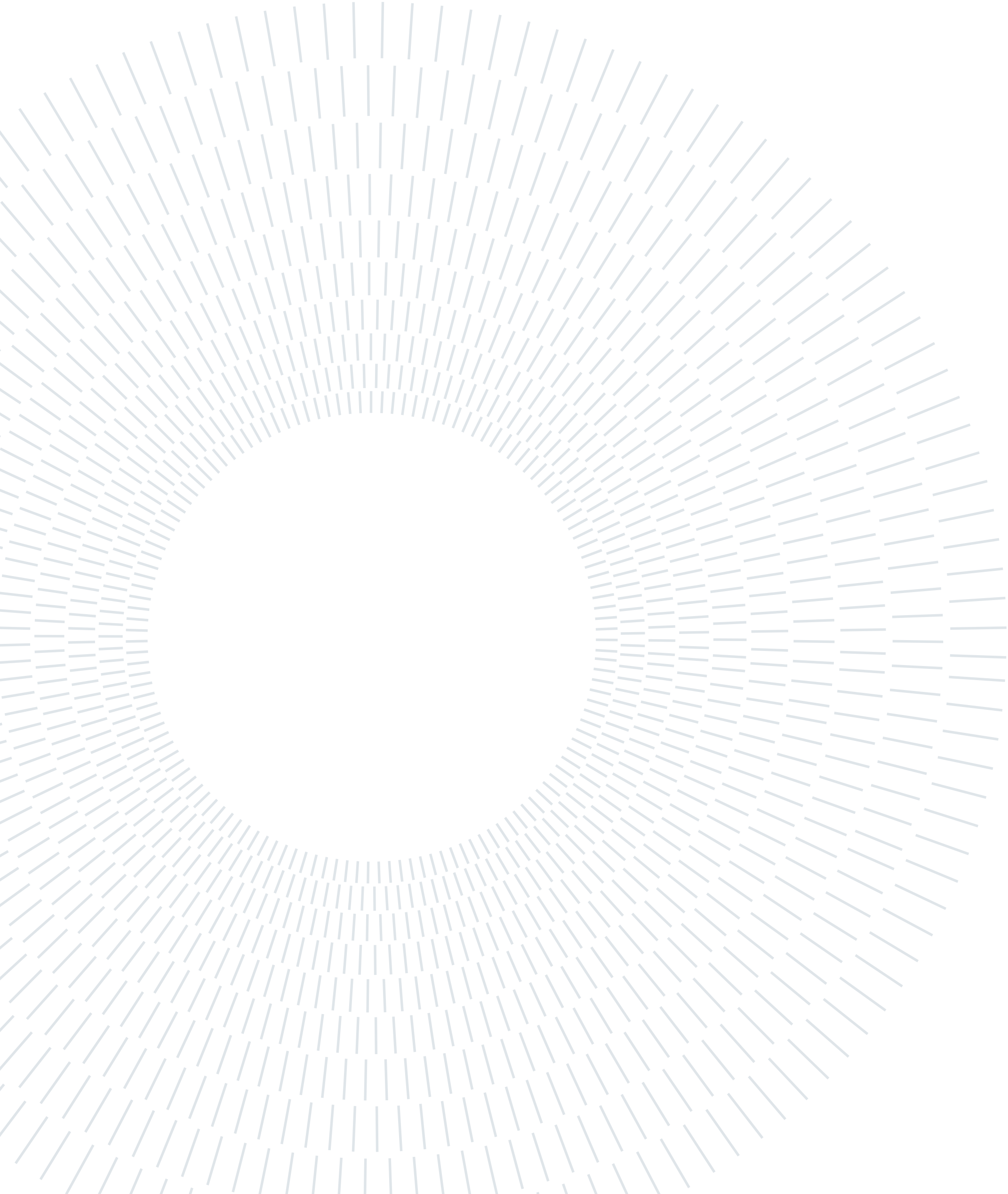This experience helped me grow in my academic path bringing out the best of me, therefore I wish to grow as a person too in the years to come.